TRANSIENT LIFT-OFF TEST RESULTS FOR AN EXPERIMENTAL HYBRID BEARING IN AIR

A Thesis

by

DAVID GREGG KLOOSTER

Submitted to the Office of Graduate Studies of
Texas A&M University
in partial fulfillment of the requirements for the degree of

MASTER OF SCIENCE

December 2009

Major Subject: Mechanical Engineering

TRANSIENT LIFT-OFF TEST

RESULTS FOR AN EXPERIMENTAL

HYBRID BEARING IN AIR

A Thesis

by

DAVID GREGG KLOOSTER

Submitted to the Office of Graduate Studies of
Texas A&M University
in partial fulfillment of the requirements for the degree of

MASTER OF SCIENCE

Approved by:

Chair of Committee,	Dara Childs
Committee Members,	W. Lynn Beason
	Alan Palazzolo
Head of Department,	Dennis O'Neal

December 2009

Major Subject: Mechanical Engineering

ABSTRACT

Transient Lift-off Test Results for an Experimental

Hybrid Bearing in Air. (December 2009)

David Gregg Klooster, B.S., Kettering University

Chair of Advisory Committee: Dr. Dara Childs

A hybrid bearing designed for use in a next generation turbo-pump is evaluated for the performance of initial lift-off, referred to as start-transient. The radial test rig features a high-speed spindle motor capable of 20,000 *rpm* that drives a 718 Inconel rotor attached via a high-speed coupling. The drive end is supported by ceramic ball bearings, while the hybrid bearing supports the opposite end. A magnetic bearing delivers the applied loading along the mid-span of the rotor. Many parameters, including ramp rate [*rpm/s*] (drive torque), supply pressure at 15,000 *rpm*, magnitude of the applied load, and load orientation, are varied to simulate different start-transient scenarios. The data are recorded in .dat files for future evaluation of transient predictions.

Analysis of the data includes an evaluation of hydrodynamic and hydrostatic lift-off, an assessment of rub from passing through a lightly damped critical speed, and observation of pneumatic hammer instability. Hydrodynamic lift-off occurs when the hydrodynamic pressure, resulting from the relative motion of two surfaces, overcomes the forces acting on the rotor; no indication of hydrodynamic lift-off is provided. Hydrostatic lift-off results from the external supply pressure (which for this test rig is speed dependent) overcoming the forces acting on the rotor as determined from rotor centerline plots. With 0.263 *bar* applied unit load in the vertical direction, hydrostatic lift-off occurs at 0 *rpm* and 2.08 *bar* supply pressure. With a much higher load of 1.53 *bar*, hydrostatic lift-off is at 12,337 *rpm* and 10.7 *bar* supply pressure.

The required supply pressure for hydrostatic lift-off is approximately a linear function of the applied unit load. In a turbopump, hydrostatic lift-off depends on the speed because the supply pressure is proportional to the speed squared. With the load in

the horizontal direction, hydrostatic lift-off occurs at lower speeds and pressures. The ramp rate did not affect the required supply pressure for hydrostatic lift-off. A lower supply pressure at 15,000 *rpm* lowered the required supply pressure for hydrostatic lift-off as well as the natural frequencies creating a rub. The hydrostatic lift-off speed should be minimized to avoid damage to the rotor/bearing surfaces due to contact.

DEDICATION

To my parents, Gregg and Kathy Klooster, who taught me how to work hard, and gave me all their support and encouragement. To my Lord and Savior, Jesus Christ, who has given me new life and hope.

ACKNOWLEDGEMENTS

I would like to thank all those who have helped me throughout this process. Thank you to my friends and family whose advice and encouragement meant so much when I needed someone to lean on. Thank you to my professors, both undergraduate and graduate, who took the time to help me learn. A special thanks to those at the Turbolmachinery Laboratory especially Paul Esser, Roston Elwell, David Mertz, Henry Borchard, Eddy Denk, Stephen Phillips and many others who gave of their time and energy to help me. Also, to my committee members Dr. Childs, Dr. Beason, and Dr. Palazzolo, thank you for your patience and wisdom throughout.

TABLE OF CONTENTS

Page

Page

LIST OF FIGURES

Page

Page

Page

Page

LIST OF TABLES

Page

NOMENCLATURE

C	Calibration factor, see Eq. (9) [F L^2 L^{-4}]
C_r	Bearing radial clearance [L]
C_{xx}, C_{xy}, C_{yx}, C_{yy}	Damping coefficients [F T L^{-1}]
C_{xxo}	Damping coefficient in the absence of fluid compressibility [F T L^{-1}]
D	Diameter [L]
e_x, e_y	Distance from bearing center [L]
F	Force [F]
f_{bx} , f_{by}	Force coefficients [F]
F_o	Tare [F]
g	Effective gap [L]
K_{xx}, K_{xy}, K_{yx}, K_{yy}	Stiffness coefficients [F L^{-1}]
L	Length [L]
M_{xx}, M_{xy}, M_{yx}, M_{yy}	Mass coefficients [M]
N	Number of recesses on the bearing [dim]
P_a	Ambient pressure [F L^{-2}]
P_r	Recess pressure [F L^{-1}]
P_s	Supply pressure [F L^{-1}]
P_{rc}	Pressure ratio [dim]
V_r	Total recess volume [L^3]
W	Load [F]
W_{unit}	Unit load [F L^{-2}]
x	Offset [L]
z	Restrictor control parameter [dim]
Δx , Δy	Relative rotor-stator displacement in x or y direction [L]
α_c	Reduced damping factor due to compressibility, see Eq. (3) [dim]
β	Fluid compressibility factor [L^2 F^{-1}]
γ	Circumferential flow factor [dim]
e	Bearing eccentricity, see Eq. (7) [L]

ε_0	Bearing eccentricity ratio, see Eq. (8) [dim]
Ω	Excitation or whirl frequency [T^{-1}]
LOL	Load on land
LOR	Load on recess

INTRODUCTION

Turbo-pump applications that use ball bearings in cryogenic fluids can experience rapid wear when the pump is at full power, limiting the life of the bearing. Hybrid bearings have been proposed for use in next-generation turbo-pumps because of their Diameter X Speed (DN) life, low friction factor, and application in low-viscosity fluids [1]. Hybrid bearings use an external pressure supplied through a flow restrictor (orifice) to create pressure that supports the rotor (shaft) without rotation. The pressure generated by the flow through an orifice gives the hybrid bearing a theoretical infinite DN life. The direct stiffness and load capacity of a hybrid bearing are independent of the fluid viscosity making a cryogenic application ideal [1].

The cryogenic applications proposed for the next-generation of turbo-pumps utilize the pump-discharge fluid as the external pressure supplied to the bearing. Therefore, during start-up the bearings are flooded but unpressurized, at which point wear can occur due to rubbing between the rotor and the bearing. The time, speed, and supply pressure when rubbing during start-up ceases is referred to as "lift-off". Currently, there is a lack of available data to validate the theoretical predictions for the initial start-up, referred to as start-transient, of hybrid bearings. This report will present the transient lift-off results of a radial hybrid bearing with air as the supply medium, including the effects of varying the ramp rate (drive torque), the supply pressure at 15,000 *rpm*, the applied unit load, and load orientation. Air is compressible as is liquid hydrogen.

This thesis follows the style and format of the ASME Journal of Tribology.

BACKGROUND

Steady-state operation and rotordynamic coefficients of hybrid bearings have been well documented with good comparisons between predictions and experimental results for eccentricities up to 0.5 [1]. While the steady-state performance of hybrid bearings is predictable, little data exists to verify predictions for start-transients of hybrid bearings.

Scharrer et al. [2] designed a test apparatus to simulate a bearing for the Space Shuttle Main Engine (SSME) High Pressure Oxidizer Turbo-pump (HPOTP) and performed start-transients of hydrostatic bearings in liquid nitrogen. An analog servo controller matched speed, load, and pressure characteristics to data taken from an SSME HPOTP.

The main objective of the start-transients performed by Scharrer et al. [3] was to determine the influence of the load magnitude and speed profile on lift-off speed. Also investigated were the influence of different bearing and journal material characteristics on the transient behavior. Table 1 shows the two different bearing geometries that were tested; the carbon P5N bearing had a different geometry than the nickel-chromium alloy and silver plated nickel-copper alloy bearings. Five different test conditions were performed; the first with no load applied. The remaining four had two different peak loads and varied the load profile linearly with speed and a speed squared relationship. For each material combination, all five-test conditions were run four times. The silver plated NiCu bearing was tested using the higher peak load and the linear load profile an additional 60 times.

Table 1 Bearing geometry from Scharrer et al. [3]

	Carbon P5N bearing	NiCr alloy bearing, and Ag-plated NiCu alloy
Bearing length	31.75 mm (1.25 in)	31.75 mm (1.25 in)
Bearing diameter	76.2 mm (3.0 in)	76.2 mm (3.0 in)
Number of Recesses	6	8
Recess area ratio	0.12	0.2
Recess axial length	11.1 mm (0.438 in)	13.8 mm (0.544 in)
Recess circ. Length	13.3 mm (0.524 in)	13.8 mm (0.544 in)
Recess depth	0.254 mm (0.01 in)	0.254 mm (0.01 in)
Operating radial clearance	0.084 mm (0.0033 in)	0.079 mm (0.0031 in)
Orifice diameter	1.3 mm (0.051 in)	1.27 mm (0.05 in)

Scharrer et al. [3] defined hydrodynamic lift-off as the change in motion of the journal from a clockwise rotation to counterclockwise as the rotor rotates counterclockwise. Hydrostatic lift-off is defined when the journal departs from the bearing and moves towards the center. Figure 1 shows a typical orbit plot of the x and y journal displacements and the two types of lift-off. Although orbit plots were used, the primary indicator of lift-off was the inflection of the turbine servovalve position.

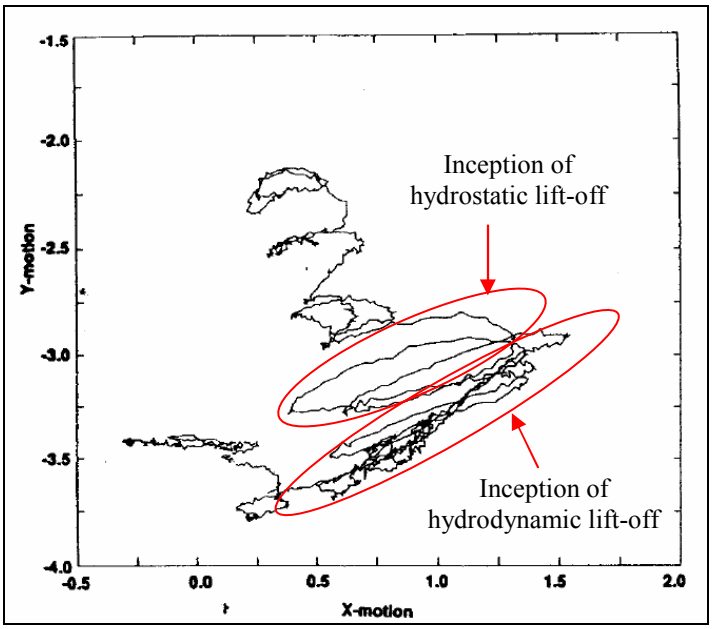

Fig. 1 Orbit plots showing hydrodynamic and hydrostatic lift-off from Scharrer et al. [3]

Scharrer et al. [3] concluded that the predictions for lift-off speed were conservative, low friction material combinations produced early lift-off, and hydrostatic bearings would work in turbo-pump operating conditions.

Scharrer et al. [4] extended the testing to a tapered, knurled annular hydrostatic bearing (Lomakin bearing) in liquid oxygen. The dimensions are shown in Table 2. The test plan applied the load as a linear function of speed, and an unbalance mass was added to simulate the build up of dynamic loads during start-up.

Table 2 Bearing geometry from Scharrer et al. [4]

Bearing length	31.75 mm (1.25 in)
Bearing diameter	76.2 mm (3.0 in)
Inlet operating radial clearance	0.28 mm (0.011 in)
Exit operating radial clearance	0.066 mm (0.0026 in)

Transient behavior was observed during 61 start-ups. Contrary to Scharrer et al. [3], Scharrer et al. [4] defined lift-off as a correlation between the orbit plots and inflections in the speed profile. The change in the definition of lift-off was due to the lag present in the turbine servovalve position relative to the event of lift-off. Figure 2 shows the hydrodynamic and hydrostatic lift-off speed for each of the start-transients.

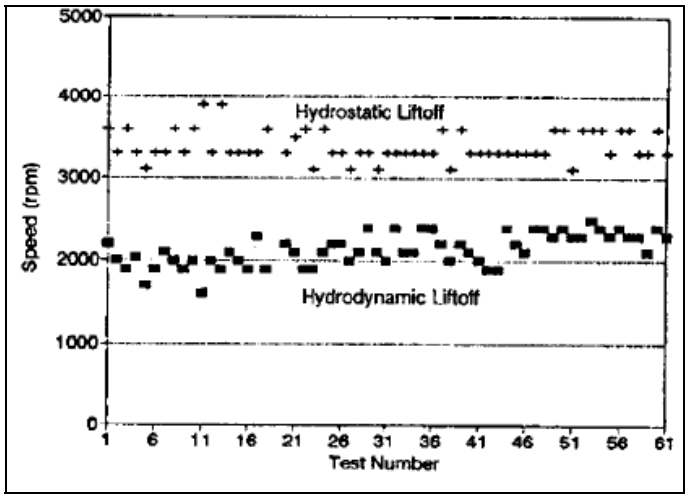

Fig. 2 Lift-off testing from Scharrer et al. [4]

Very little change in the orbit size and complete transient between the first and last test were observed, indicating the bearing stiffness and damping was unaffected. Post inspection of the bearing revealed wear in the direction of the load at approximately an 80° arc. Two different regions of wear were present; the first had burnishing and debris formation while the second as shown in Figure 3 was characterized by abrasion. Scharrer et al. [4] concluded that the bearing performance did not degrade during the 61 tests, and the bearing is a viable replacement to the ball bearings in use at the time.

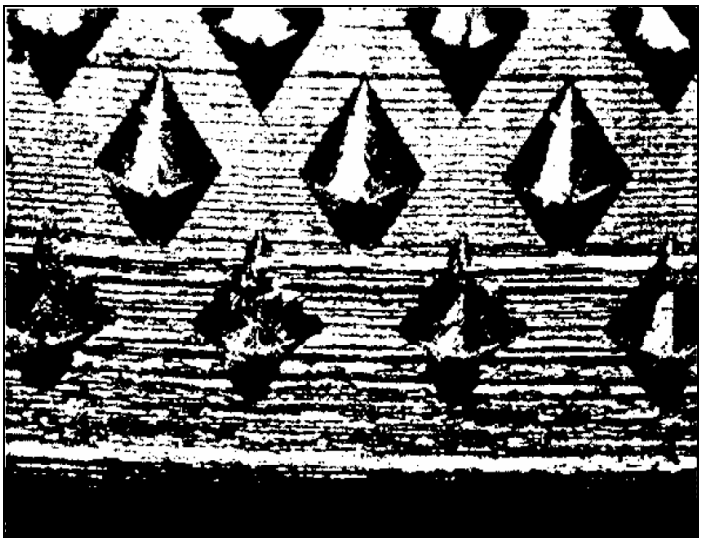

Fig. 3 Abrasion without burnishing from Scharrer et al. [4]

While Scharrer et al. [2,3,4] looked at the transient behavior of hydrostatic bearings in liquid nitrogen, and an annular hydrostatic bearing in liquid oxygen the focus was material selection. Not enough data are available from the study to calibrate start-transient predictions.

Borchard [5] performed many start-transients of a hybrid (hydrostatic and hydrodynamic) bearing in water. The hybrid bearing was designed by Pavelek [6] using XLHydroJet® [7]; the design features and geometry are detailed later. Table 3 shows several parameters including; the ramp rate (drive torque), supply pressure, applied load, and load orientation that were varied to simulate different start-transient scenarios. Data from each test was recorded in a .dat file to calibrate start-transient predictions. For each case tested, Borchard [5] simulated the speed, pressure, and load profile to data from a next-generation turbo-pump through a custom LabVIEW program, called Transient.VI.

Table 3 Start-transient cases performed by Borchard [5]

Texas A&M Test Matrix (NGST Radial Test Rig)					
	Ramp Rate (rpm/s)	Pressure @ 15,000 rpm	Type of Loading	Load Cases (Multiples of Rotor Weight)	Load Orientation
Case 1	8824	18.25 bar (264.7 psia)	Static	1X, 2X, 3X, 4X, 5X, 6X, 7X, 8X	Load on Pad (Vertical)
Case 2	4412	18.25 bar (264.7 psia)	Static	1X, 2X, 3X, 4X, 5X, 6X, 7X, 8X	Load on Pad (Vertical)
Case 3	4412	9.63 bar (139.7 psia)	Static	1X, 2X, 3X, 4X, 5X, 6X, 7X, 8X	Load on Pad (Vertical)
Case 4	2206	9.63 bar (139.7 psia)	Static	1X, 2X, 3X, 4X, 5X, 6X, 7X, 8X	Load on Pad (Vertical)
Case 5	2206	5.32 bar (77.2 psia)	Static	1X, 2X, 3X, 4X, 5X, 6X, 7X, 8X	Load on Pad (Vertical)
Case 6	8824	18.25 bar (264.7 psia)	Static	1X, 2X, 3X, 4X, 5X, 6X, 7X, 8X	Load on Land (Horizontal)
Case 7	4412	18.25 bar (264.7 psia)	Static	1X, 2X, 3X, 4X, 5X, 6X, 7X, 8X	Load on Land (Horizontal)
Case 8	4412	9.63 bar (139.7 psia)	Static	1X, 2X, 3X, 4X, 5X, 6X, 7X, 8X	Load on Land (Horizontal)
Case 9	2206	9.63 bar (139.7 psia)	Static	1X, 2X, 3X, 4X, 5X, 6X, 7X, 8X	Load on Land (Horizontal)
Case 10	2206	5.32 bar (77.2 psia)	Static	1X, 2X, 3X, 4X, 5X, 6X, 7X, 8X	Load on Land (Horizontal)

Like Scharrer et al. [3,4], Borchard [5] defined hydrostatic lift-off as the point of departure towards the center of the bearing. Hydrodynamic lift-off could not be determined from the data. Upon removal of the bearing after an excess of 100 start-transients, Borchard [5] observed that burnishing was present on the rotor surface, and the bearing surface showed signs of burnishing and pitting.

Borchard's [5] main objective was to gather data to validate predictions of a start-transient for a hybrid bearing in water. In addition to the successful completion of the main objective, Borchard [5] was able to make the following conclusions. Hydrodynamic lift-off could not be accurately predicted by the orbit plots. Hydrostatic lift-off is predictable, highly pressure dependent, and increases to a higher speed with increasing load and ramp rate. Hybrid bearings are susceptible to damage during start-transients in which the supply medium is a process fluid.

The data that Borchard [5] gathered gives a good indication of the start-transient performance of a hybrid bearing in a non-compressible supply medium. Liquid hydrogen is a compressible fluid commonly used in cryogenic applications; therefore, data using a similar fluid is necessary to validate the start-transient predictions for a hybrid bearing in a compressible supply medium.

TEST RIG AND HARDWARE

An experimental test rig was designed and built by Pavelek [6] and Dyck [8] to validate predictions for dry friction whip and whirl, pneumatic-hammer instability, and the start-transient of hybrid bearings. Figure 4 shows the configuration designed in Solidworks by Pavelek [6] for start-transient testing of hybrid bearings. The electric motor designed to drive the rotor is a high speed integral motorized spindle unit manufactured by SKF Precision Technologies and driven by a Spindle Master Drive (model 50270-0). A high speed KHS-200 bellows coupling manufactured by GAM transfers the torque from the motor to the rotor which is made of 718 Inconel. Barden 207HC angular contact ball bearings with a nominal bore of 35 *mm* are support bearings on the drive end of the rotor. SKF Magnetic Bearings, Inc. designed and manufactured a magnetic bearing exciter system capable of applying up to 1223 *N* (275 *lbs*) which can be applied to the rotor through a laminate sleeve. Angular-contact ball bearings called catcher bearings are installed to prevent contact between the laminate sleeve and the poles of the magnetic bearing exciter in case of a failure. The air buffer seal and collection chamber shown in Figure 4 are not used for start-transients of hybrid bearings because the supply medium is air. More details of the magnetic bearing are in the Appendix, while the hybrid bearing, fluid supply loop, and DAQ/instrumentation are detailed in the following sections.

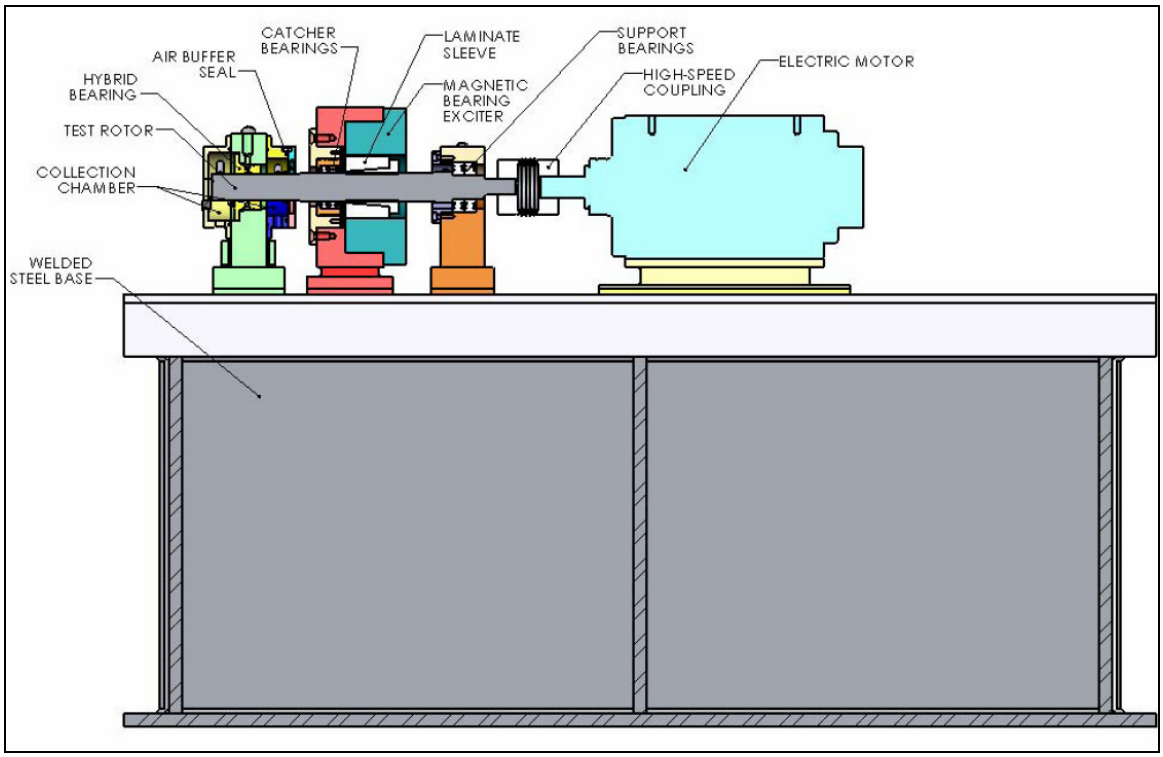

Fig. 4 Start-transient test configuration designed in Solidworks by Pavelek [6]

Hybrid Bearing

The hybrid bearing was designed by Pavelek [6] to be consistent with a proposed next-generation turbo-pump in terms of clearance, diameter, number of recesses, etc. The bearing geometry as designed by Pavelek [6] is shown in Figure 5. The hybrid bearing features a supply annulus where the supply medium will flow into. Two o-ring grooves are machined on either side of the annulus to prevent leakage. There are six bearing recesses (pockets) with an orifice in the center of the recess which supply fluid to the bearing. Two recess pressure-measurement ports for dynamic and static pressure-measurements are in the bottom pocket. A bolt flange secures the bearing to the housing while a taper machined on the outer surface aids in alignment.

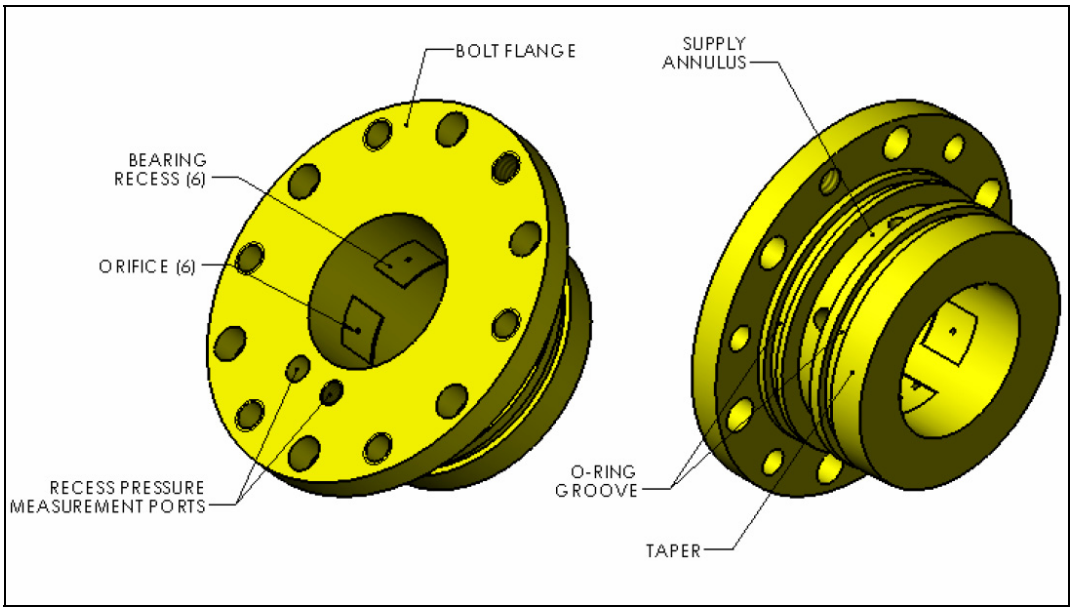

Fig. 5 Hybrid bearing geometry by Pavelek [6]

The major feature to be considered in the design was the orifice diameter. Mosher and Childs [9] found the optimum pressure ratio for hybrid bearings is between 0.45-0.50. The pressure ratio (P_{rc}) is the recess pressure divided by the supply pressure as shown in Eq. (1).

$$P_{rc} = \frac{P_r - P_a}{P_s - P_a} \tag{1}$$

Pavelek [6] used the data from Table 4 in XLHydroJet®, varying the orifice diameter to find the optimum pressure ratio of 0.5. An orifice diameter of 1.19 *mm* (0.047 *in*) was selected because the predicted pressure ratio with the bearing in the centered position at 15,000 *rpm* and a nominal supply pressure of 18.25 *bar* (265.4 *psia*) is approximately 0.50 as seen in Figure 6. With air as the fluid medium the predicted pressure ratio is 0.71, the actual pressure ratio is 0.67.

Table 4 Parameters used for the design of the hybrid bearing by Pavelek [6]

Bearing Geometeric Parameters		
Parameter	Value	Unit
Diameter	3.81E-02	[m]
Axial Length	3.81E-02	[m]
Inlet Radial Clearance	6.35E-05	[m]
Exit Radial Clearance	6.35E-05	[m]
# Pockets	6	[-]
Pocket Axial Length	1.20E-02	[m]
Pocket 1 - Leading Edge	24	[deg]
Pocket 1 - Arc Length	36	[deg]
Pocket Depth	5.08E-04	[m]
Orifice Diameter	1.19E-03	[m]
Orifice Discharege Coefficient	0.85	[-]
Orifice Angle Injection	0	[-]
Orifice Location Relative to Pocket	0.5	[-]
Pocket Area Ratio	0.1875	[-]

Supply Fluid Properties (Water)		
Parameter	Value	Units
Supply Temperature	54	[C]
Cavitation Pressure	0.006893	[bar]
Viscosity at TS, PS	5.01E-04	[Ns/m^2]
Density at TS, PS	984.33	[kg/m^3]
Viscosity at TS, PA	5.01E-04	[Ns/m^2]
Density at TS, PA	983.5	[kg/m^3]
Compressibility	4.64E-10	[m^2/N]

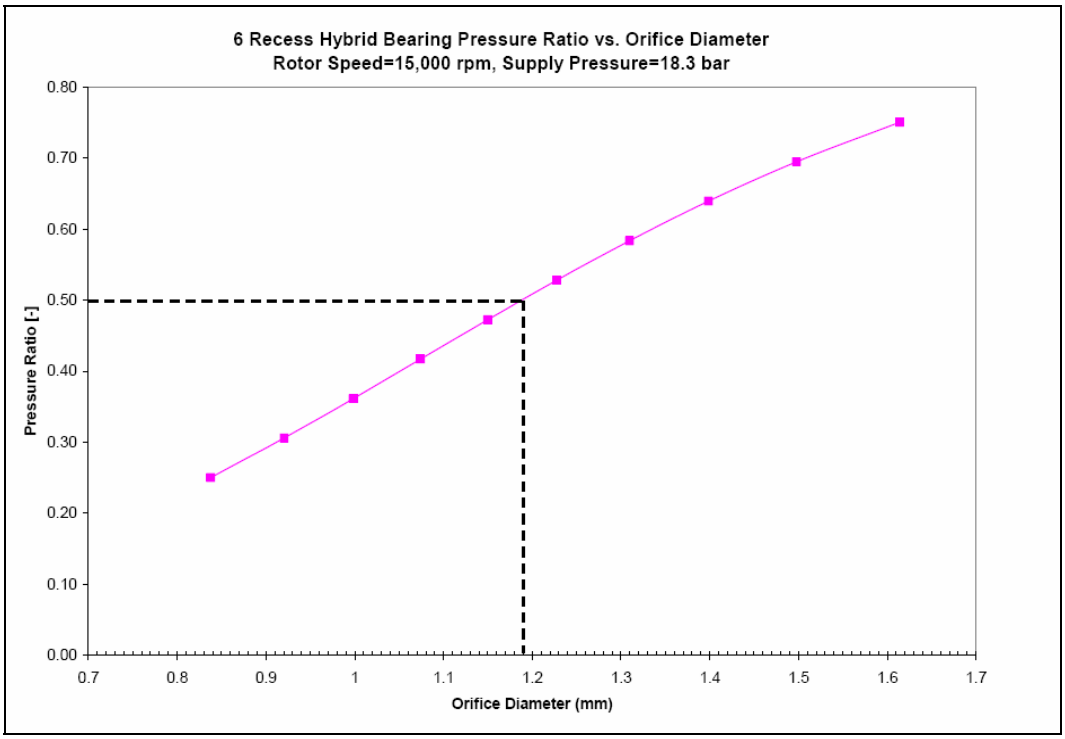

Fig. 6 Hybrid bearing pressure ratio vs. orifice diameter by Pavelek [6]

Although the bearing was designed with a taper on the outer surface to assist in the alignment of the bearing, the angle was not within specifications. Borchard [5] adjusted the alignment manually until the clearance was within 0.0127 *mm* (0.0005 *in*) of the designed bearing clearance. The clearance was determined by applying a load with the magnetic bearing at eight equally spaced points around the circumference of the

bearing. Any small misalignment of the bearing results in an increased pressure ratio and premature contact between the rotor and bearing [5]. For the present testing, the bearing will be manually aligned, and the clearance will be verified by a bump test. The alignment and bump test procedure is detailed in the experimental procedure section.

Hybrid bearings with compressible fluid media are subject to pneumatic-hammer instabilities. Pneumatic-hammer occurs at low frequencies and has negative values of the direct damping coefficients. San Andrés [10] discusses the cause of pneumatic hammer instability and the important design features of a hybrid bearing to avoid pneumatic hammer. San Andrés [10] defines the value of direct damping in Eq. (2). Where α_c is the reduced damping factor due to compressibility at zero frequency and given by Eq. (3).

$$C_{xx} = C_{xxo}\left(1-\alpha_c\right) \tag{2}$$

$$\alpha_c = \frac{3NV_r\left(P_r - P_a\right)\beta}{\pi LDC_b\left[z+1+2\gamma\sin^2\left(\pi/N\right)\right]} \tag{3}$$

The direct damping will be positive if $\alpha_c << 1$, which implies that the recess volume (V_r) to film land volume (πLDc) ratio remains small, and the compressibility factor (β) is small.

Next generation turbo-pumps operate with the fluid-discharge as the supply medium for the hybrid bearing, commonly a cryogenic fluid such as liquid hydrogen is utilized. Liquid hydrogen is susceptible to pneumatic hammer instability and low break frequencies due to its low viscosity and compressibility factor (β = 8.88x10^{-8} [m^2 N^{-1}]) [10]. The break frequency is the frequency at which there is a brisk increase in direct stiffness accompanied by a rapid decrease in damping. The susceptibility to pneumatic hammer instability and a low break frequency with liquid hydrogen as the supply medium limits the application of hybrid bearings in turbo-pump applications. Application of a hybrid bearing in a cryogenic application such as liquid hydrogen requires careful attention to the possibility of pneumatic-hammer instability as well as the value of the break frequency.

Borchard [11] performed two tests to verify the predictions of pneumatic-hammer for the hybrid bearing. Each test measured the damping at varying pressures for a static (non-rotating) rap test. In the first test the recess pressure-measurement ports as shown in Figure 5 were filled with wax. No pneumatic-hammer instability was predicted, and none was observed. The wax was removed, and a screw was inserted in the recess pressure-measurement ports and backed out to add volume to the recess. With the added volume pneumatic-hammer instability was predicted and observed. To prevent pneumatic-hammer instability Borchard [11] recommends that the ratio of recess pocket area to land area should be 20-25%, the pocket depth should be minimized, and the orifices should not have a pressure recovery zone.

The hybrid bearing is held in place by the bolt flange to the test bearing housing, but is also connected to the ground by o-rings. Prior to start-transient testing pneumatic-hammer instability was observed in the hybrid bearing at the same recess volume Borchard [11] predicted the absence of pneumatic-hammer instability. Inspection of the o-rings revealed worn areas with noticeable hardening in some areas. The o-rings were replaced and, for the same recess volume and supply pressure, no pneumatic-hammer instability was observed. As o-rings wear, localized hardening can occur; the observation that changing o-rings eliminated the pneumatic-hammer instability verifies that the o-rings add damping to the system.

Fluid Supply Loop

A compressor supplies compressed air at 20.32 *bar* (294.7 *psia*) to the test rig to serve as the fluid medium for start-transients of the hybrid bearing. A FT-10NEE1-GEAH4 flow meter from Flow Technology is installed in the piping to the test rig, with pressure and temperature sensors upstream and downstream, to record the mass flow rate. The pressure transducers are manufactured by Omega Engineering, Inc., model PX209-300G10V. The temperature sensors and signal conditioners are manufactured by Omega Engineering, Inc. model RTD-NPT-72-E-DUAL-1/4-MPT and DRF-RTD-24VDC-0/200C-0/10.

Downstream of the flow meter and upstream of the radial test rig, a Baumann 3/4" 32-24588SVF valve is used to control the supply pressure to the test rig. The air will exit the bearing at atmospheric pressure.

DAQ/Instrumentation

Design and assembly of the test rig was completed by Pavelek [6], Dyck [8] and Borchard [5], with modifications to the fluid supply loop and static recess pressure measurement made by the author for start-transient testing with air. Figure 7 shows the assembly of the test rig with instrumentation. For each start-transient, a custom virtual instrument (VI) was created in LabVIEW to record the data as listed in Table 5. The data are recorded at 5000 *Hz* to decrease data saturation. The data output are recorded to a .dat file during testing for later use. The instrumentation specification for all sensors in recorded order is in the appendix.

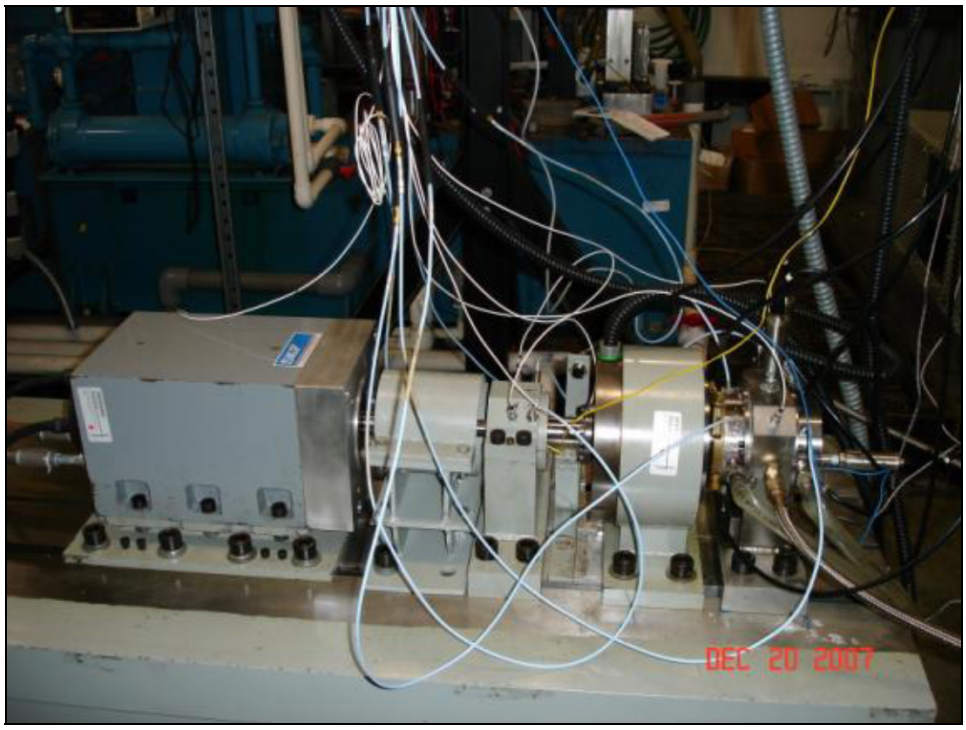

Fig. 7 Assembly of the test rig with instrumentation from Borchard [5]

Table 5 Instrumentation recorded in custom VI in LabVIEW

Number	Location	Number	Location
	Speed		**Pressure Transducers**
1	Mounted Tachometer	1	Exhaust Pressure
1	Encoder Speed		(Mounted after test bearing)
	(Via motor controller software)	1	Supply Pressure
1	Scaled Tachometer		(Mounted before test bearing)
	(Via motor controller software)	1	Recess Pressure
	Proximity Probes		(Mounted in recess of test bearing)
2	Test Bearing Housing (Outboard)	1	Flow Meter Pressure (Inlet)
	(2 probes mounted at 90 degrees)		(Mounted before flow meter)
2	Test Bearing Housing (Inboard)	1	Flow Meter Pressure (Outlet)
	(2 probes mounted at 90 degrees)		(Mounted after flow meter)
2	Support Bearing Housing		**Temperature Sensors**
	(2 probes mounted at 90 degrees)	1	Supply Temperature
	Accelerometers		(Mounted before test bearing)
2	Support Bearing Housing	1	Flow Meter Temperature (Inlet)
	(2 probes mounted at 90 degrees)		(Mounted before flow meter)
2	Test Bearing Housing	1	Flow Meter Temperature (Outlet)
	(2 probes mounted at 90 degrees)		(Mounted after flow meter)
2	Drive Motor Casing		**Voltage**
	(1 probe mounted by support bearing)	1	Force Voltage
	Flow Meter		(W 24 vertical displacement)
1	Flow Meter	1	Force Voltage
	(Mounted before test bearing)		(V 24 horizontal displacement)
	Torque	1	Valve Voltage
1	Load		(Voltage applied to valve, converted to 4-20 mA signal)
	(Via motor controller software)		

PROPOSED TEST CASES

This section explains the rationale behind the design of start-transient tests. First, variation in ramp rate and supply pressure of the provided data is outlined. Second, the maximum applied load for each case is given, and finally, the start-transient predictions including rotordynamic analysis is detailed.

Ramp Rate and Supply Pressure

Northrop Grumman Space Technology (NGST) provided ROCETS predictions of a next generation turbo-pump to be replicated on the radial test rig that is shown in Figure 8. The pump-discharge fluid is used to pressurize the bearing; therefore, the supply pressure is proportional to the speed (ω) squared. The target supply pressure for the start-transients is 18.25 *bar* (265.4 *psia*), which is 1.7 *seconds* after the turbo-pump starts. The SKF motor will accelerate to 15,000 *rpm* over the 1.7 *seconds* as it closely follows the speed profile provide in the ROCETS predictions. Figure 9 shows a comparison of a start-transient compared to the ROCETS predictions.

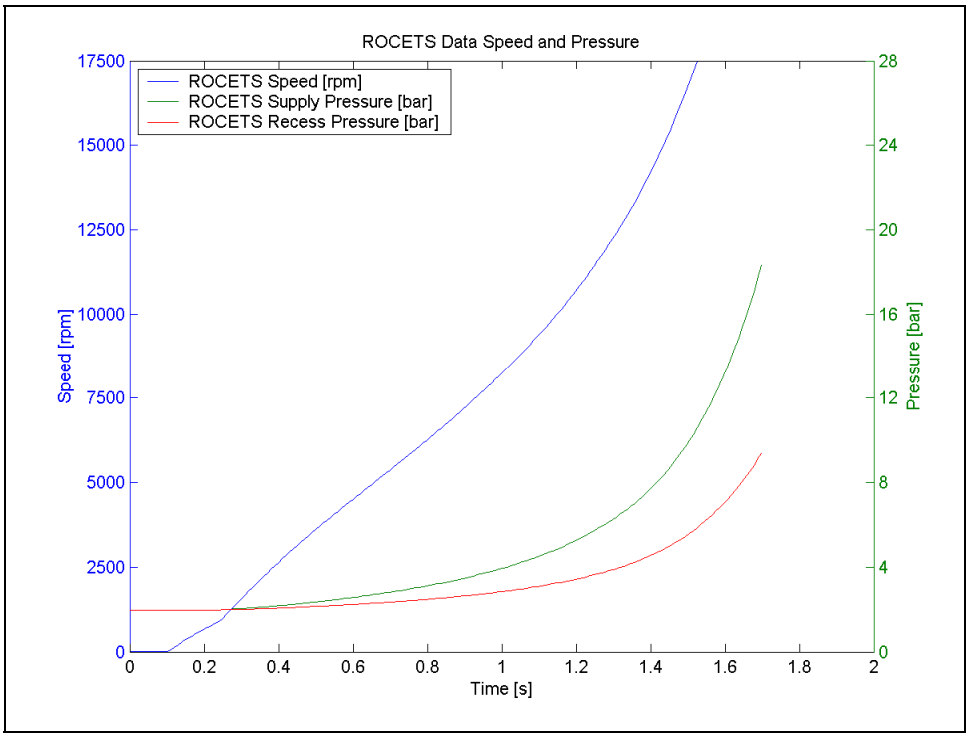

Fig. 8 NGST ROCETS data of a next generation turbo-pump provided for replication

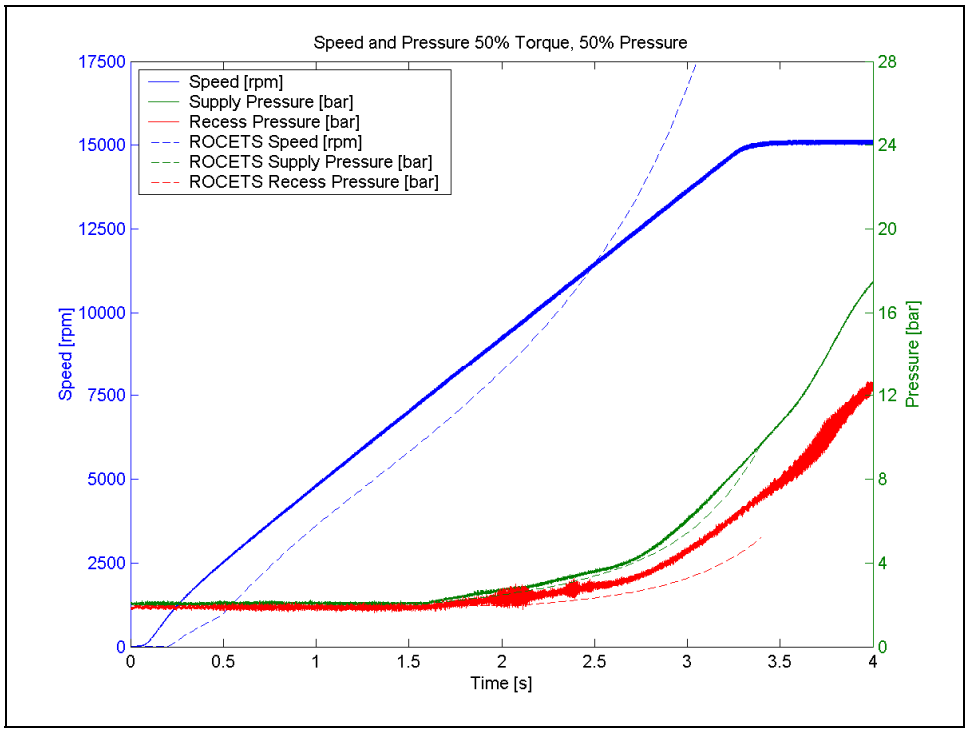

Fig. 9 Comparison between ROCETS data and start-transient test

The ramp rate (drive torque) and the supply pressure at 15,000 *rpm* are two variables for different start-transient cases. The ROCETS predictions that we are trying to replicate has an acceleration of the rotor from zero to 15,000 *rpm* over 1.7 *seconds* with a 18.3 *bar* (265.4 *psia*) supply pressure, referred to as 100% torque-100% pressure. If the ramp rate is twice as long, the torque is 50% and four times as long the torque is 25%. If the supply pressure at 15,000 *rpm* is half of target supply pressure, 9.63 *bar* (139.7 *psia*), the pressure is 50% and one fourth, 5.32 *bar* (77.2 *psia*), the pressure is 25%.

Five start-transient test cases are used to simulate various ramp rates and supply pressures. Figure 9 displays the 50% torque-50% pressure case. The four other cases are 100% torque-100% pressure, 50% torque-100% pressure, 25% torque-50% pressure, and 25% torque-25% pressure. The speed and supply pressure are matched to the ROCETS predictions and shown in the appendix. For the 100% torque-100% pressure and 50% torque-100% pressure cases, the supply pressure does not match the ROCETS predictions perfectly as the rate the supply pressure can increase is limited; therefore, the supply

pressure started to increase before the ROCETS predictions to supply 18.25 *bar* (265.4 *psia*) at 1.7 *seconds*.

Applied Load

Other variables for different start-transient test cases are the magnitude and direction of the load. Simulations were run in XLHydroJet®, with the hybrid bearing geometry and air as the fluid medium, to predict the maximum unit load the hybrid bearing could support. The unit load defines the load capacity of the bearing and is shown in Eq. (4). Table 6 shows the input parameters used in XLHydroJet®.

$$W_{unit} = \frac{W}{LD} \tag{4}$$

Table 6 Input parameters used for the simulation of the hybrid bearing with air

Bearing Geometeric Parameters		
Parameter	Value	Unit
Diameter	3.81E-02	[m]
Axial Length	3.81E-02	[m]
Inlet Radial Clearance	6.35E-05	[m]
Exit Radial Clearance	6.35E-05	[m]
# Pockets	6	[-]
Pocket Axial Length	1.20E-02	[m]
Pocket 1 - Leading Edge	24	[deg]
Pocket 1 - Arc Length	36	[deg]
Pocket Depth	5.08E-04	[m]
Orifice Diameter	1.19E-03	[m]
Orifice Discharege Coefficient	0.815	[-]
Orifice Angle Injection	0	[-]
Orifice Location Relative to Pocket	0.5	[-]
Pocket Area Ratio	0.1875	[-]

Supply Fluid Properties (Air)		
Parameter	Value	Units
Supply Temperature	21.1	[C]
Cavitation Pressure	0	[bar]
Viscosity at TS, PS	2.89E-02	[Ns/m^2]
Viscosity at TS, PA	1.84E-02	[Ns/m^2]
Gas Constant	2.87E+02	J/kg-C
Compressibility Z supply	1.02	--
Compressibility Z exit	9.80E-01	--

The predicted maximum unit loads that the bearing could support with a supply pressure of either 264.7, 139.7, or 77.2 *psia*, exhaust pressure atmospheric, and the rotor at 15,000 *rpm* are shown in Table 7. The maximum unit load was predicted with: (1) An eccentricity ratio greater than 0.75, and (2) An eccentricity ratio greater than the clearance minus twice the surface roughness of the bearing.

Table 7 Max unit load hybrid bearing supports in air at 15,000 *rpm*

	Max Unit Load [bar (psi)]	
Supply Pressure [bar (psia)]	0.75 eccentricity	2x Surface roughness
18.25 (264.7)	3.85 (55.8)	4.45 (64.5)
9.63 (139.7)	2.18 (31.6)	2.52 (36.6)
5.32 (77.2)	1.25 (18.1)	1.51 (21.9)

To calculate the hydrodynamic effect, the maximum unit load the bearing can support with a constant pressure, while reducing the speed, and with an eccentricity less than twice the surface roughness is shown in Table 8. As the speed decreases the hydrodynamic effect is calculated to decrease noted by the reduction in maximum unit load. With no hydrodynamic effect or zero speed, the bearing will support a very high unit load indicating that lift-off is highly pressure dependent.

Table 8 Max unit load hybrid bearing supports in air for varying speed

Supply Pressure 5.32 [*bar*] (77.2 [*psia*])		Supply Pressure 9.63 [*bar*] (139.7 [*psia*])		Supply Pressure 18.25 [*bar*] (264.7 [*psia*])	
Lift-off Speed [rpm]	Max Unit Load [bar (psi)]	Lift-off Speed [rpm]	Max Unit Load [bar (psi)]	Lift-off Speed [rpm]	Max Unit Load [bar (psi)]
15000	1.51 (21.9)	15000	2.52 (36.6)	15000	4.45 (64.5)
12000	1.46 (21.2)	12000	2.49 (36.1)	12000	4.44 (64.4)
9000	1.42 (20.6)	9000	2.45 (35.6)	9000	4.42 (64.0)
6000	1.39 (20.1)	6000	2.42 (35.2)	6000	4.42 (64.1)
3000	1.36 (19.8)	3000	2.41 (35.0)	3000	4.42 (64.0)
100	1.35 (19.6)	100	2.41 (35.0)	100	4.43 (64.2)

For a turbopump start-transient, supply pressure is proportional to speed squared. Therefore, if the supply pressure at 15,000 *rpm* is 18.25 *bar* (264.7 *psia*), the supply pressure will remain below 9.63 *bar* (139.7 *psia*) or half until around 12,000 *rpm*. To limit the duration of rubbing, the maximum unit load applied will be roughly half the predicted maximum unit load the bearing will support for an eccentricity less than 0.75. Table 9 shows how much load will be applied for each test case.

Table 9 Proposed NGST radial test rig test matrix for air

Texas A&M Test Matrix (NGST Radial Test Rig)				
	Ramp Rate [*rpm/s*]	Pressure @ 15,000 rpm	Load Cases (Multiples of Rotor Weight)	Load Orientation
Case 1	8824	18.25 bar (264.7 psia)	1X, 2X, 3X, 4X, 5X, 6X, 7X, 8X	Load on Recess (Vertical)
Case 2	4412	18.25 bar (264.7 psia)	1X, 2X, 3X, 4X, 5X, 6X, 7X	Load on Recess (Vertical)
Case 3	4412	9.63 bar (139.7 psia)	1X, 2X, 3X, 4X, 5X	Load on Recess (Vertical)
Case 4	2206	9.63 bar (139.7 psia)	1X, 2X, 3X, 4X	Load on Recess (Vertical)
Case 5	2206	5.32 bar (77.2 psia)	1X, 2X, 3X	Load on Recess (Vertical)
Case 6	8824	18.25 bar (264.7 psia)	1X, 2X, 3X, 4X, 5X, 6X, 7X, 8X	Load on Land (Horizontal)
Case 7	4412	18.25 bar (264.7 psia)	1X, 2X, 3X, 4X, 5X, 6X, 7X	Load on Land (Horizontal)
Case 8	4412	9.63 bar (139.7 psia)	1X, 2X, 3X, 4X, 5X	Load on Land (Horizontal)
Case 9	2206	9.63 bar (139.7 psia)	1X, 2X, 3X, 4X	Load on Land (Horizontal)
Case 10	2206	5.32 bar (77.2 psia)	1X, 2X, 3X	Load on Land (Horizontal)

Definitions

Static - Load is calculated at the bearing and is applied before test remaining constant throughout test.
Linear - Load is time dependant starting from zero at beging of test and reaching max load at final speed (15,000 rpm).
Ramp Rate - Time in seconds taken to reach 15,000 rpm during start-up.
Vertical - Load is being applied downward in the vertical direction.
Horizontal - Load is side load in the horizontal direction.
Rotor Weight - This is 31 *N* (7 *lbs*.) at the test bearing.

Figure 10 shows the intended direction of load for the load on recess (LOR) and load on land (LOL) start-transient cases as well as the *x*-*y* axis for orientation of the load from the magnetic bearing. The load from the magnetic bearing in the LOR case is applied directly on a recess while, in the LOL case, the load is applied on the land of the bearing.

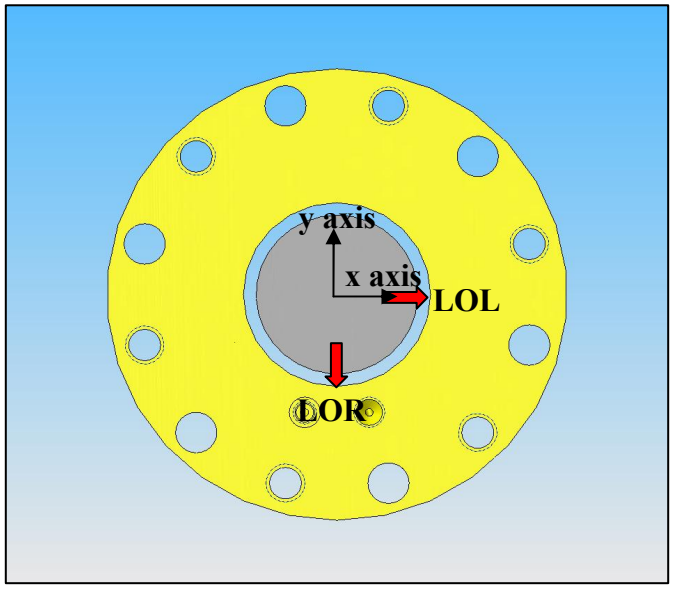

Fig. 10 Direction of load for LOR and LOL configurations

EXPERIMENTAL PROCEDURE

This section details the experimental procedure for the start-transient testing. First, the manual alignment to ensure the measured clearance of the hybrid bearing is outlined. Second, the bump test procedure to record the clearance before and after start-transient testing is detailed. Finally, the procedure for start-transient testing in LabVIEW through custom VI's is given.

Alignment Procedure

The hybrid bearing was designed with a matching taper to that of the test bearing pedestal [6]. However, experience showed that the taper is not correct and can lead to misalignment of the hybrid bearing [5]. To ensure proper alignment, the hybrid bearing is bolted to the test bearing pedestal. The (non-rotating) rotor is displaced around the outside of the bearing by hand while recording the displacement. The data are analyzed, and if the clearance in any direction from the center is less than 0.0127 *mm* (0.5 *mils*) of the measured clearance, the bearing is adjusted. This method allows for almost instant feedback and for iterative changes in alignment until the desired clearance is achieved. The properly aligned bearing is then secured to the test bearing pedestal for start-transient testing.

Bump Test Procedure

A bump test is preformed to establish the bearing clearance for start-transient testing. Load is applied through the magnetic bearing in eight directions forcing the rotor to the side of the bearing while proximity probes record the displacement. Figure 11 displays the orientation of applied load during a bump test.

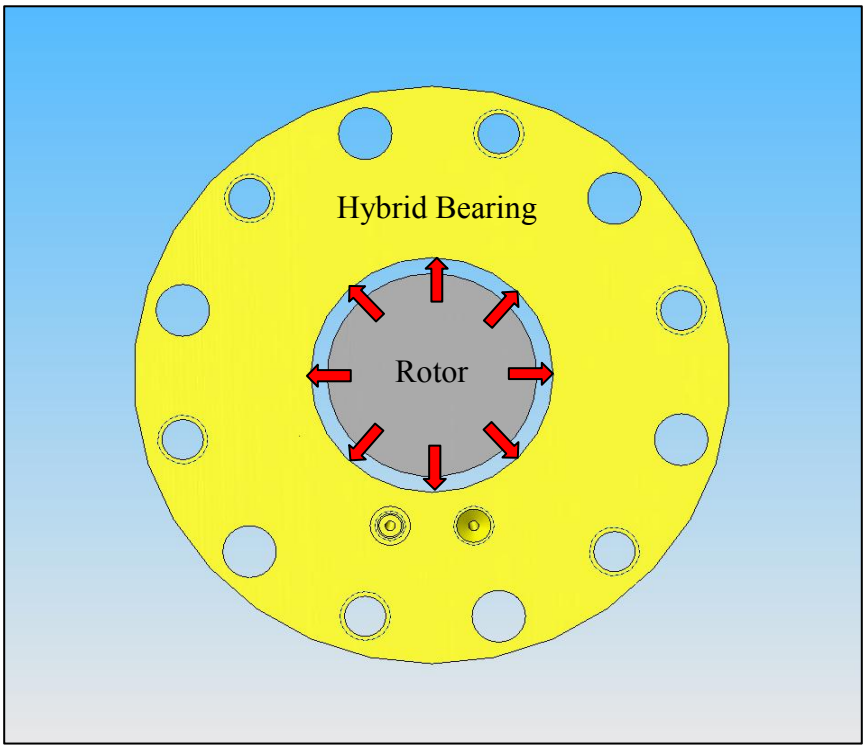

Fig. 11 Direction of applied load during bump test

The difference between the rotor's displacement in one direction and 180 degrees from that direction gives a diametral clearance. The average diametral clearance establishes the bearing clearance for start-transient testing. This is a final check to verify the average diametral clearance is within 0.0127 *mm* (0.5 *mils*), or nearly 80%, of the measured clearance and that the bearing is secure in the test bearing pedestal. Also, the center of the bearing relative to the proximity probe positions is established; therefore, the data taken during the start-transients can be adjusted so the center of the bearing is at (0, 0).

Start-Transient Procedure

For each start-transient test case, a custom virtual VI was created in LabVIEW. Besides recording the instrumentation data as listed in Table 5 at 5000 *Hz*, the custom VI coordinates the start and acceleration rate of the motor, timing for the opening of the valve, and application of the direction and magnitude of the load. The timing and application of the motor, valve, and load for each case were determined through extensive experiments prior to the start-transient testing.

TEST RESULTS

Many start-transients were performed, each varying different parameters including ramp rate (drive torque), supply pressure, applied unit load, and load orientation. Table catalogs each start-transient test that was completed. The following sections detail the results including: (1) steady-state predictions of the start-transient test cases including passing through a critical speed with a comparison to test results, (2) hydrostatic lift-off defined by rotor centerline plots and waterfall plots, (3) an evaluation of torque, (4) a comparison to the results from Borchard [5] using water, and (5) a look at the bearing before and after start-transient testing.

Start-Transient Predictions

The model for small motion about an equilibrium position for a hybrid bearing is shown in Eq. (5), [12].

$$\begin{Bmatrix} f_{bx} \\ f_{by} \end{Bmatrix} = -\begin{bmatrix} K_{xx} & K_{xy} \\ K_{yx} & K_{yy} \end{bmatrix} \begin{Bmatrix} \Delta x \\ \Delta y \end{Bmatrix} - \begin{bmatrix} C_{xx} & C_{xy} \\ C_{yx} & C_{yy} \end{bmatrix} \begin{Bmatrix} \Delta \dot{x} \\ \Delta \dot{y} \end{Bmatrix} - \begin{bmatrix} M_{xx} & M_{xy} \\ M_{yx} & M_{yy} \end{bmatrix} \begin{Bmatrix} \Delta \ddot{x} \\ \Delta \ddot{y} \end{Bmatrix} \tag{5}$$

XLHydroJet® calculates the stiffness, damping, and added mass coefficients of the hybrid bearing for a given supply and exhaust pressure, load, and speed. The bearing coefficients are used in XLTRC^{TM} Rotordynamics Suite (XLTRC^2) [13] to perform a rotordynamic analysis. The original analysis performed by Pavelek [6] is modified to include the updated bearing coefficients. For each of the five start-transient test cases due to the varying ramp rate and supply pressure, a steady-state rotordynamic analysis using XLTRC^2 is performed. The steady-state rotordynamic analysis produces the damped natural frequency map showing predicted critical speeds in some cases, damped eigenvalue mode shapes, and steady-state rotordynamic response plot.

The rotordynamic damped natural frequency map plots the first, second, third, and higher natural frequencies of the rotor versus rotor speed. The synchronous line represents the running speed, and the coincidence of the shaft's natural frequency and the synchronous line is a critical speed (CS). A forward CS refers to the whirling motion of

the rotor in the direction of rotation and can be excited by many factors including imbalance. A CS with a whirling motion in the direction opposite of rotation is a backward CS. Unless significant bearing orthotropy is present, backward CSs are not excited by imbalance.

The 100% torque-100% pressure and 50% torque-100% pressure cases predict no CSs below 15,000 *rpm*. The maximum amplitude in the 100% torque-100% pressure case is 0.017 *mm* (0.67 *mils*) while in the 50% torque-100% pressure case it is 0.022 *mm* (0.87 *mils*).

Figure 12 displays the rotordynamic damped natural frequency map for the 50% torque-50% pressure case. The 25% torque-50% pressure case is very similar and shown in the appendix. The similarity is expected because the bearing coefficients and rotor natural frequencies are calculated independent of the ramp rate, the major difference between the two cases.

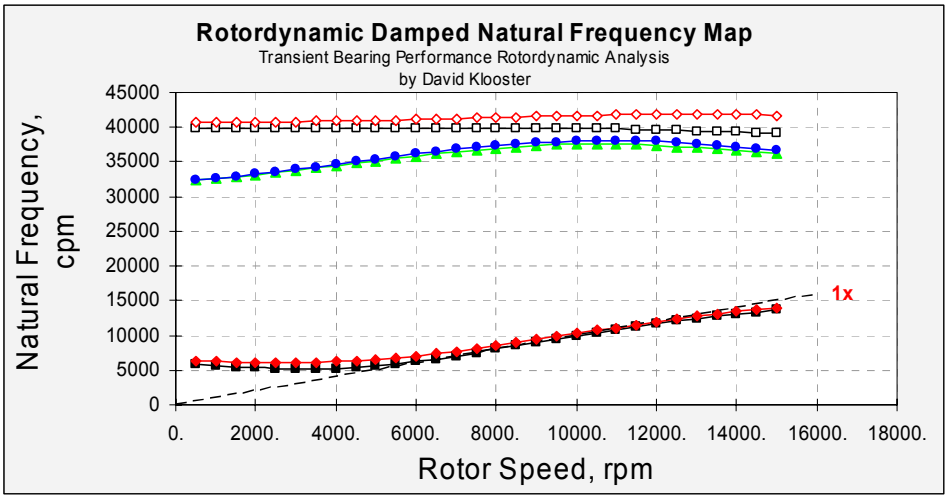

Fig. 12 Rotordynamic damped natural frequency map 50% torque-50% pressure

Note the first forward and first backward natural frequencies increase along the synchronous line. This is a potentially disastrous problem as running near a CS for an extended period of time can lead to a large amplitude response especially with little to no damping. Figure 13 shows that the first backward CS is near 8,000 *rpm* while the first forward CS is near 12,000 *rpm*.

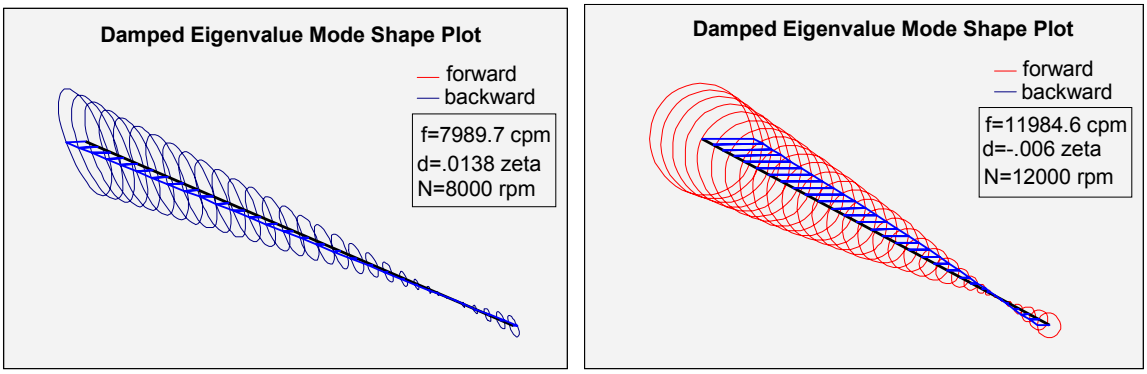

Fig. 13 Damped eigenvalue mode shape for first two modes 50% torque-50% pressure

The rotordynamic response plot shown in Figure 14 predicts large amplitude response of 0.34 *mm* (13 *mils*) at the backward CS near 8,000 *rpm* and 0.78 *mm* (31 *mils*) at the forward CS near 12,000 *rpm*. This predicted response would create a significant rub as the response is expected to exceed the bearing diametral clearance of 0.12 *mm* (4.8 *mils*) as shown in Figure 14. Similarly, the 25% torque-50% pressure case predicts a backward CS near 7,000 *rpm* with an amplitude of 0.28 *mm* (11 *mils*) and a second backward CS near 11,500 *rpm* with a response of 0.51 *mm* (20 *mils*).

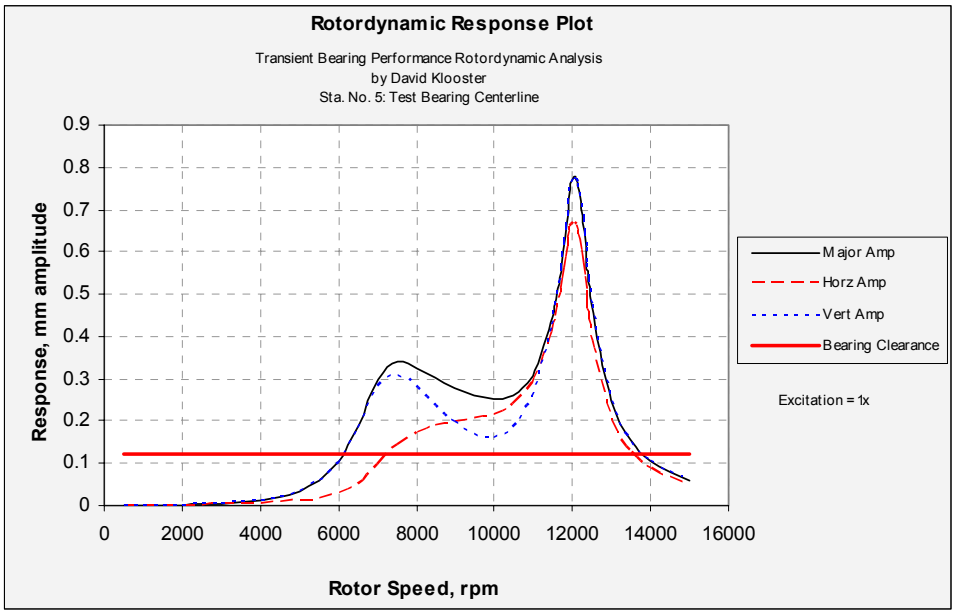

Fig. 14 Steady state rotordynamic response plot at test bearing 50% torque-50% pressure

The 25% torque-25% pressure case predicts a backward CS near 5,000 *rpm* and a forward CS near 6,000 *rpm* as shown in Figure 15. Figure 16 shows the rotordynamic

response plot with amplitudes exceeding the bearing diametral clearance of 0.38 *mm* (15 *mils*) between the running-speed range $5{,}700 \leq \omega \leq 6{,}400$.

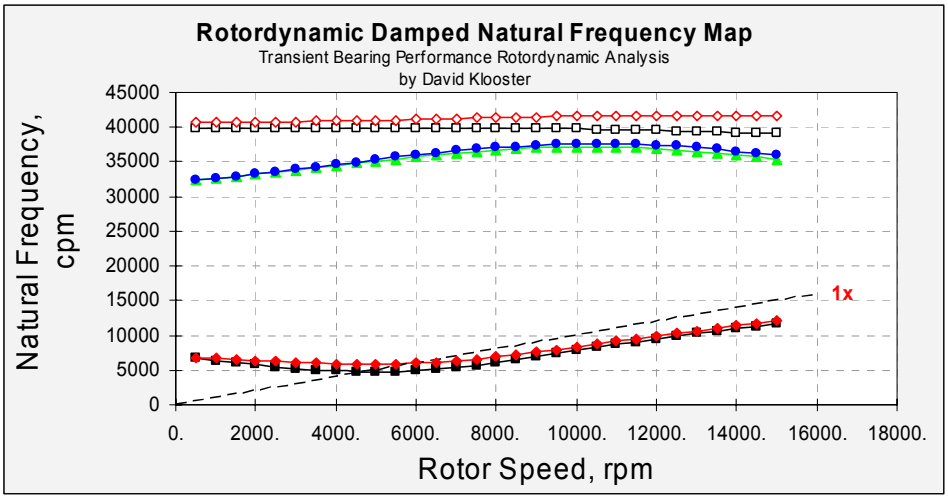

Fig. 15 Rotordynamic damped natural frequency map 25% torque-25% pressure

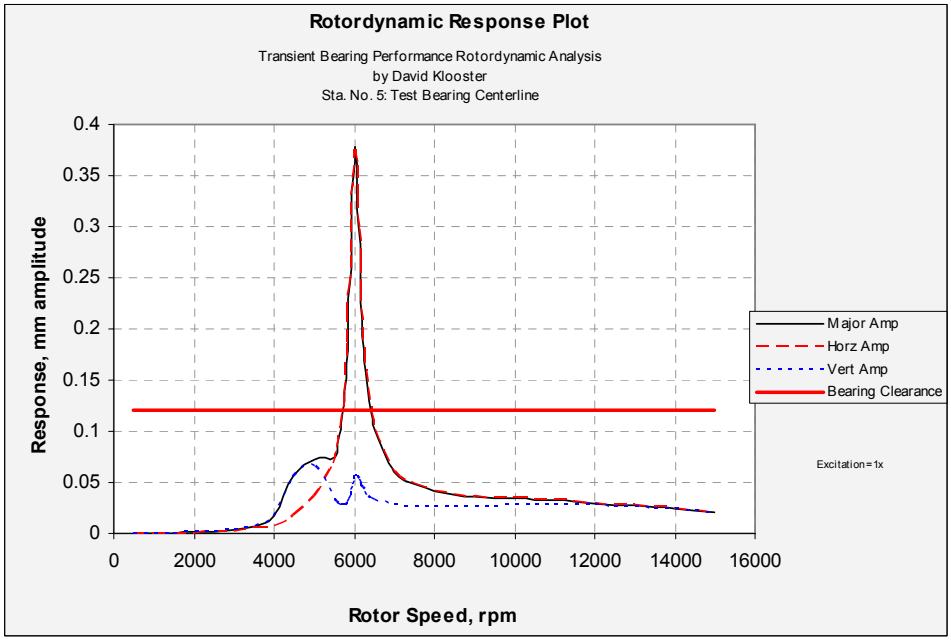

Fig. 16 Steady state rotordynamic response plot at test bearing 25% torque-25% pressure

For three of the five cases the steady state rotor response is predicted to exceed the bearing radial clearance and cause rubbing. The critical speed and amplitude response are summarized in Table 10.

Table 10 Predicted critical speeds for start-transient 1X static unit load cases

	Order	Direction	Critical Speed [rpm]	Amplitude [mm (mils)]
50% Torque 50% Pressure	1st	Backward	8,000	0.34 (13)
	2nd	Forward	12,000	0.78 (31)
25% Torque 50% Pressure	1st	Backward	7,000	0.28 (11)
	2nd	Backward	11,500	0.51 (20)
25% Torque 25% Pressure	1st	Backward	5,000	0.07 (2.9)
	2nd	Forward	6,000	0.38 (15)

There are two reasons the proposed test cases in Table 9 will be followed despite the prediction to rub while passing through a critical speed. The predictions in XLHydroJet® and XLTRC^2 are steady state not transient. A fast acceleration to 15,000 *rpm* may reduce the predicted response. The author found this to be true. While maintaining a supply pressure of 8.55 *bar* (124 *psia*) the motor was accelerated to 15,000 *rpm* while the ramp rate was varied between 8824 *rpm/s*, 4412 *rpm/s*, and 2206 *rpm/s*. Figure 17 shows that with a quick acceleration of 8842 *rpm/s* and 4412 *rpm/s* the amplitude response was much lower than an acceleration of 2206 *rpm/s*.

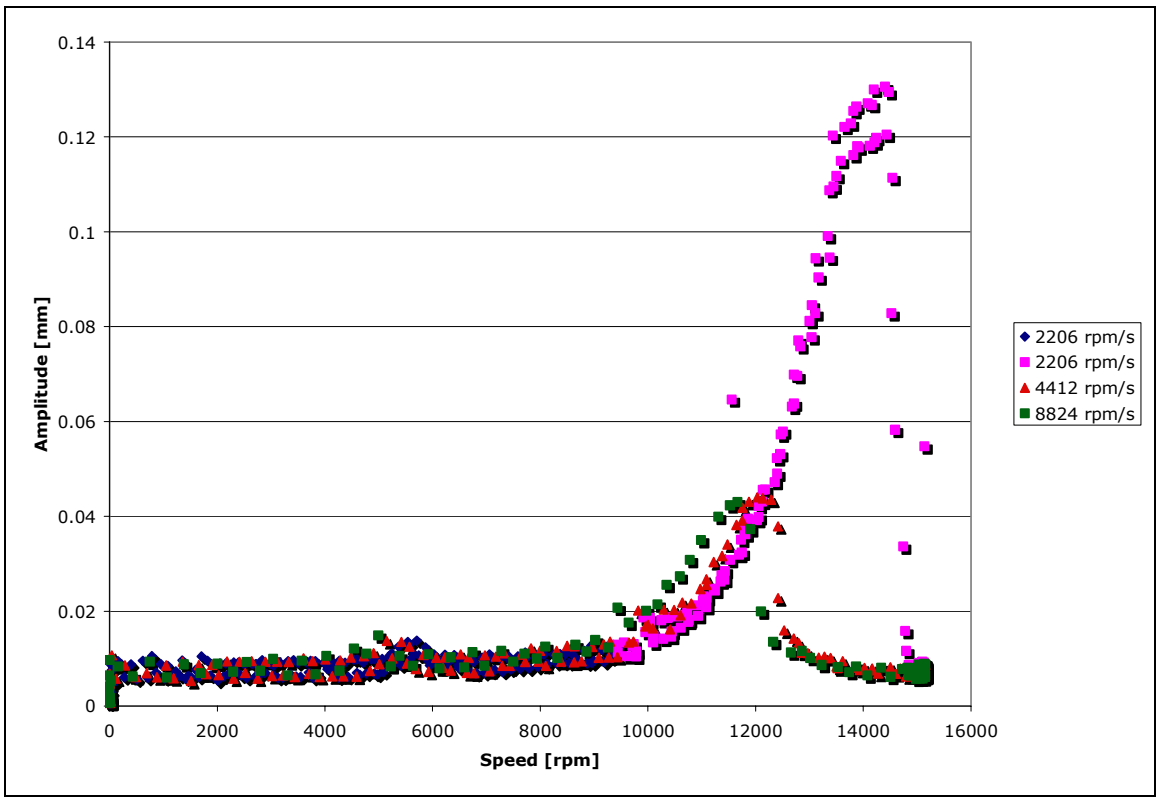

Fig. 17 Amplitude response for varying ramp rate with a constant supply pressure of 8.55 bar

The second reason the proposed test cases in Table 9 will be followed is that with increased unit load the speed at which lift-off occurs is predicted to increase. At very high unit loads, lift-off is predicted at speeds higher than the critical speeds. Therefore, since the start-transient testing has a fast acceleration to 15,000 *rpm*, and at higher unit loads the lift-off speed is predicted to be higher than the critical speed, the proposed start-transient test cases in Table 9 were followed.

In each of the 1X and 2X static unit load, for the 50% torque-50% pressure, 25% torque-50% pressure, and 25% torque-25% pressure start-transient cases, the rotor hydrostatically lifted-off at the beginning of the start-transient because the initial supply pressure was greater the applied load. As the speed approached a CS, the rotor's amplitude increased, and contact with the bearing occurred causing rubbing. With a static unit load of 3X or higher, hydrostatic lift-off occurred near or after the predicted CS, and there was no observation of rub. The data at which the start-transient test began to rub is shown in Table 11.

Table 11 Observed initial running speed for rub near predicted critical speed

	Ramp Rate [rpm/s]	Supply Pressure at 15,000 rpm [bar (psia)]	Unit Load [bar (psi)]	Load Direction	Speed [rpm]	Predict Critical Speed [rpm]	Supply Pressure [bar (psia)]	Recess Pressure [bar (psia)]	Pressure Ratio
Case 3	4412	9.63 bar (139.7 psia)	0.263 (3.81)	LOR	8916	8000	2.87 (41.6)	1.79 (26.0)	0.62
Case 3	4412	9.63 bar (139.7 psia)	0.311 (4.51)	LOR	2059	8000	1.98 (28.7)	2.14 (31.0)	1.08
Case 4	2206	9.63 bar (139.7 psia)	0.263 (3.81)	LOR	5454	7000	1.77 (25.7)	1.90 (27.5)	1.07
Case 4	2206	9.63 bar (139.7 psia)	0.311 (4.51)	LOR	4557	7000	2.05 (29.8)	2.12 (30.7)	1.03
Case 5	2206	5.32 bar (77.2 psia)	0.263 (3.81)	LOR	7023	5000	2.11 (30.7)	2.03 (29.4)	0.96
Case 5	2206	5.32 bar (77.2 psia)	0.311 (4.51)	LOR	5897	5000	2.11 (30.6)	2.19 (31.8)	1.04
Case 8	4412	9.63 bar (139.7 psia)	0.282 (4.09)	LOL	7555	8000	2.27 (32.9)	1.99 (28.9)	0.88
Case 8	4412	9.63 bar (139.7 psia)	0.443 (6.42)	LOL	26	8000	2.10 (30.5)	1.91 (27.6)	0.91
Case 9	2206	9.63 bar (139.7 psia)	0.282 (4.09)	LOL	1172	7000	1.54 (22.3)	1.63 (23.6)	1.06
Case 9	2206	9.63 bar (139.7 psia)	0.443 (6.42)	LOL	3079	7000	2.06 (29.8)	1.97 (28.6)	0.96
Case 10	2206	5.32 bar (77.2 psia)	0.282 (4.09)	LOL	6491	5000	1.91 (27.7)	1.98 (28.7)	1.04
Case 10	2206	5.32 bar (77.2 psia)	0.443 (6.42)	LOL	1699	5000	2.11 (30.6)	2.12 (30.8)	1.00

For each of the 1X cases the speed at which rub occurs is near the predicted critical speed. With the exception of one condition the 2X cases begins to rub at a lower speed than the similar 1X case. This is expected, because at a higher load, the eccentricity is higher. Therefore, the amplitude response required to cause rub is less because it is closer to the side of the bearing. The predicted critical speeds are for the 1X rotor cases and do not match as well. Regardless, even though the start of rubbing is close to the predicted critical speed it may not matter. The prediction of a critical speed assumes small motion about an equilibrium point. The predicted amplitudes in Table 10 are large, and that assumption appears to be violated.

The condition that the rotor starts and stops rubbing with the bearing for each test case is presented in the appendix. Childs [14] discusses the rotor-housing response across an annular clearance. Two models are given for continuous contact between the rotor and bearing. The first is a synchronous forwardly preccessing motion and the second is "dry-friction" whip or whirl. The synchronous response model applies here. In this model the response while the rotor is in contact with the bearing depends on the interaction between the rotor and stator, and comparison to the predicted speed range the rotor exceeds the bearing clearance may not be applicable. Nonetheless, the speed and supply pressure that the rotor starts and stops rubbing is presented in the appendix.

Rub occurring in the present start-transient testing is similar to the first model discussed by Childs [14], which is a synchronous forwardly preccessing motion. Wilkes et al. [15] however produced dry-friction whip and whirl on the test rig used here using impulse excitation. The absence of dry-friction whip and whirl in the present test program suggests that an external impulse is needed for initiation of this potentially destructive type of motion.

Hydrostatic Lift-off

Scharrer et al [3,4] and Borchard [5] defined hydrostatic lift-off in terms of the rotor centerline plot, as the point of departure towards the center of the bearing. Similarly, hydrostatic lift-off is defined as the point the eccentricity remains 0.00254 *mm* (0.1 *mils*) less than the C_r established by the bump test; this is represented by Eq. (6). The 0.00254 *mm* (0.1 *mils*) distance was selected as it is greater than the assumed surface roughness of 0.002 *mm* (0.079 *mils*). Equation (7) defines the eccentricity while Eq. (8) defines the eccentricity ratio.

$$e \le C_r - 0.00254mm(0.1[mils]) \tag{6}$$

$$e = \sqrt{e_x^2 + e_y^2} \tag{7}$$

$$\varepsilon_0 = \frac{e}{C_r} \tag{8}$$

Figure 18 displays the definition of hydrostatic lift-off. The eccentricity must be less than the bearing clearance minus 0.00254 *mm* (0.1 *mils*). If the eccentricity is less than the difference between the C_r and 0.00254 *mm* (0.1 *mils*) but increases to a value greater than this difference, then hydrostatic lift-off has not yet occurred. This circumstance may happen near the point of hydrostatic lift-off when the supply pressure is in balance with the applied unit load and the rotor may depart towards the center of the bearing and then return to the side. Also, a distinction is made between a rub due to excessive synchronous response and hydrostatic lift-off. If the rotor is hydrostatically lifted-off and in passing through a critical speed creates a rub with an eccentricity equal to C_r, this does not negate the prior event of hydrostatic lift-off.

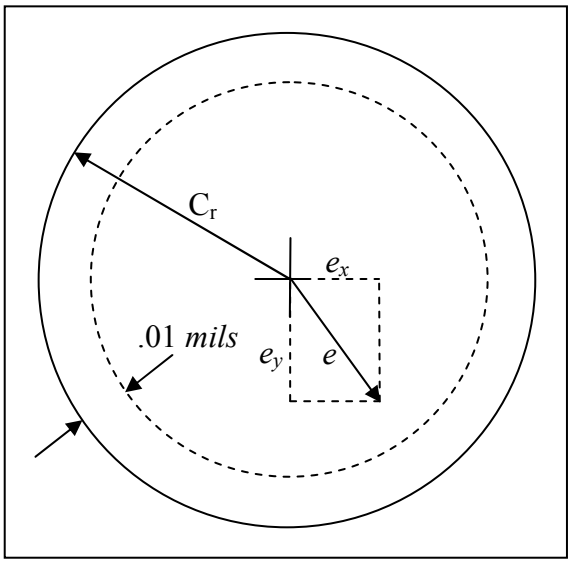

Fig. 18 Definition of hydrostatic lift-off

Hydrostatic lift-off is shown graphically in Figure 19 for the 100% torque-100% pressure, 6X static unit load, LOR start-transient. The rotor rotates along the bottom of the bearing until the point of hydrostatic lift-off, denoted by the red circle. The rotor remains above the difference between the C_r and 0.00254 *mm* (0.1 *mils*) for the remainder of the start-transient as shown in Figure 20. For all rotor centerline plots, the bearing center is located at point (0, 0).

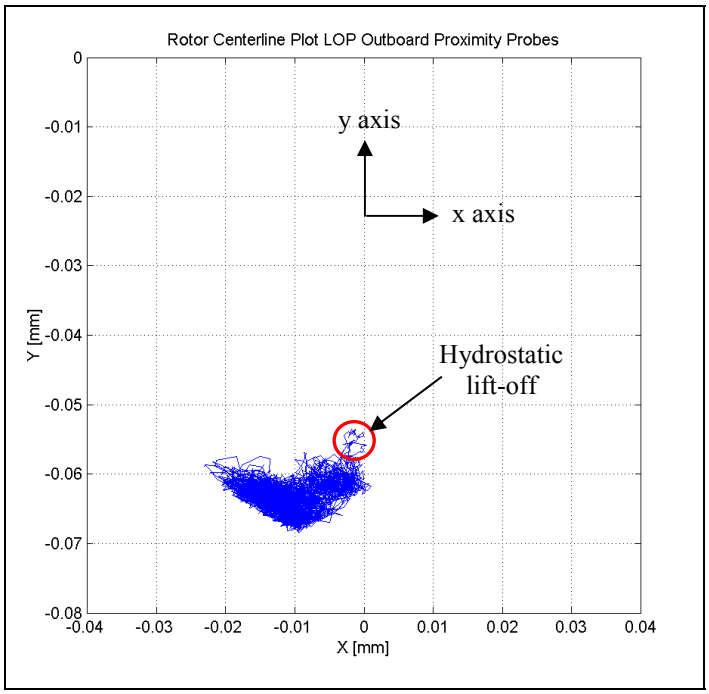

Fig. 19 Rotor centerline plot for 100% torque-100% pressure, 6X static unit load, LOR just after the point of hydrostatic lift-off

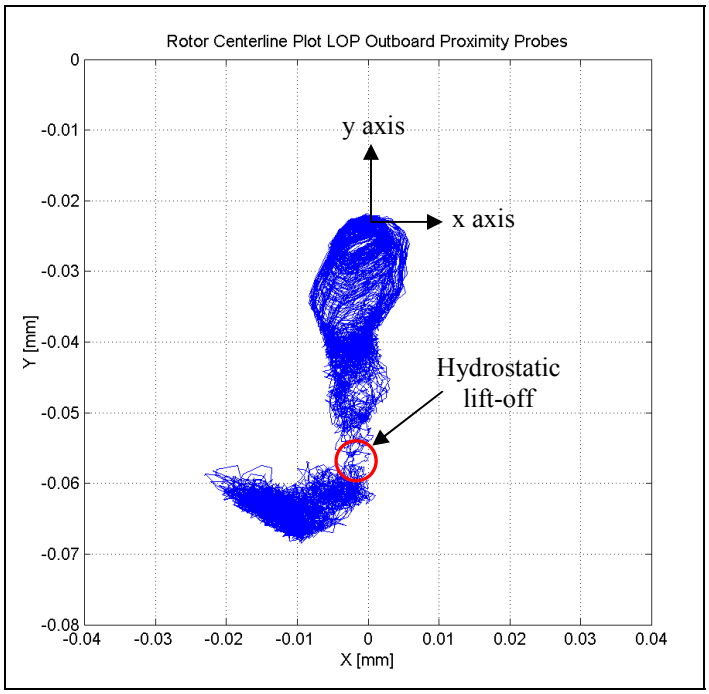

Fig. 20 Rotor centerline plot for 100% torque-100% pressure, 6X static unit load, LOR

For the LOL start-transient test cases, the load from the magnetic bearing is applied in the horizontal direction (*x* axis) on the land of the bearing. However, the applied unit load is defined as the vector summation of the load from the magnetic

bearing and gravity. For LOR cases, gravity and the load from the magnetic bearing are both along the negative *y* axis. In the LOL cases, gravity is in the - *y* direction while the load from the magnetic bearing is in the + *x* direction. Thus, the applied unit load is given in magnitude and direction relative to the - *y* axis. Figure 21 displays the applied unit load and the point of hydrostatic lift-off for the 100% torque-100% pressure, 6X static unit load, LOL start-transient.

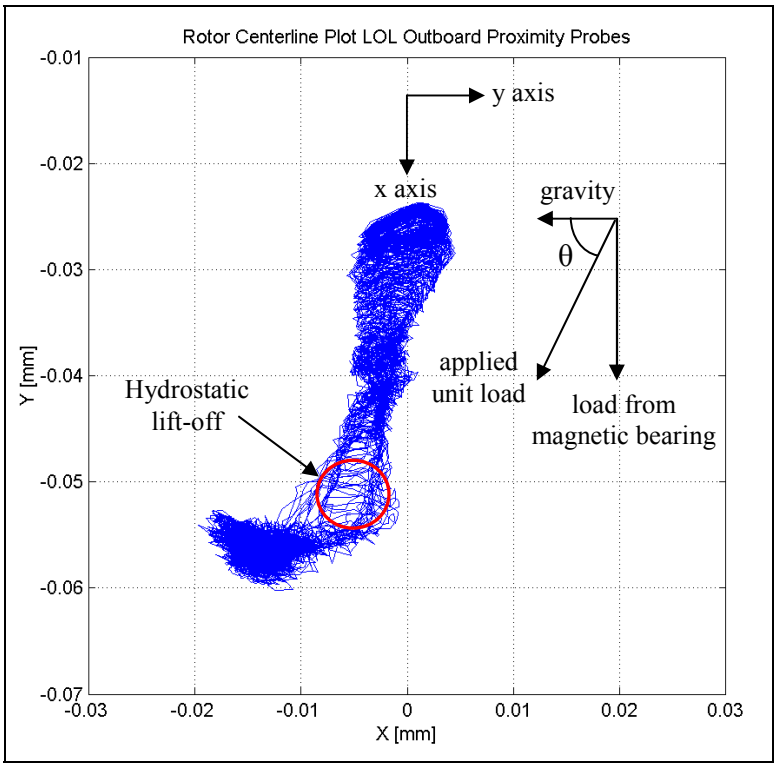

Fig. 21 Rotor centerline plot for 100% torque-100% pressure, 6X static unit load, LOL

XLHydroJet® was used to predict the speed and supply pressure for hydrostatic lift-off. In each case, the given speed, load and supply pressure were known. For the given inputs, the lowest speed and pressure that provided an eccentricity plus surface roughness less than an eccentricity ratio of one is defined as hydrostatic lift-off. Table 12 provides the predicted speed and supply pressure for hydrostatic lift-off for the LOR cases, while Table 13 provides the predicted hydrostatic lift-off for the LOL cases.

Table 12 Predicted speed and supply pressure for hydrostatic lift-off, LOR

	Ramp Rate [rpm/s]	Supply Pressure at 15,000 rpm [bar (psia)]	Load [*N* (*lbf*)]	Lift-off speed [rpm]	Lift-off supply pressure [bar (psia)]
Case 1	8824	18.25 bar (264.7 psia)	31.1 (7)	0	1.98 (28.7)
Case 1	8824	18.25 bar (264.7 psia)	62.3 (14)	4500	2.19 (31.8)
Case 1	8824	18.25 bar (264.7 psia)	93.4 (21)	5500	2.81 (40.8)
Case 1	8824	18.25 bar (264.7 psia)	125 (28)	6500	3.70 (53.7)
Case 1	8824	18.25 bar (264.7 psia)	156 (35)	7000	4.12 (59.8)
Case 1	8824	18.25 bar (264.7 psia)	187 (42)	8000	5.22 (75.7)
Case 1	8824	18.25 bar (264.7 psia)	218 (49)	8500	5.84 (84.7)
Case 1	8824	18.25 bar (264.7 psia)	249 (56)	9000	6.46 (93.7)
Case 2	4412	18.25 bar (264.7 psia)	31.1 (7)	0	1.98 (28.7)
Case 2	4412	18.25 bar (264.7 psia)	62.3 (14)	500	2.25 (32.6)
Case 2	4412	18.25 bar (264.7 psia)	93.4 (21)	3500	2.74 (39.7)
Case 2	4412	18.25 bar (264.7 psia)	125 (28)	6500	3.22 (46.7)
Case 2	4412	18.25 bar (264.7 psia)	156 (35)	9000	4.12 (59.8)
Case 2	4412	18.25 bar (264.7 psia)	187 (42)	10500	5.36 (77.7)
Case 2	4412	18.25 bar (264.7 psia)	218 (49)	11000	6.05 (87.7)
Case 3	4412	9.63 bar (139.7 psia)	31.1 (7)	0	1.98 (28.7)
Case 3	4412	9.63 bar (139.7 psia)	62.3 (14)	8500	2.25 (32.6)
Case 3	4412	9.63 bar (139.7 psia)	93.4 (21)	9500	2.60 (37.7)
Case 3	4412	9.63 bar (139.7 psia)	125 (28)	11500	3.43 (49.7)
Case 3	4412	9.63 bar (139.7 psia)	156 (35)	12500	4.19 (60.8)
Case 4	2206	9.63 bar (139.7 psia)	31.1 (7)	0	1.98 (28.7)
Case 4	2206	9.63 bar (139.7 psia)	62.3 (14)	8500	2.25 (32.6)
Case 4	2206	9.63 bar (139.7 psia)	93.4 (21)	10000	2.81 (40.8)
Case 4	2206	9.63 bar (139.7 psia)	125 (28)	11500	3.56 (51.6)
Case 5	2206	5.32 bar (77.2 psia)	31.1 (7)	0	1.98 (28.7)
Case 5	2206	5.32 bar (77.2 psia)	62.3 (14)	12000	2.32 (33.6)
Case 5	2206	5.32 bar (77.2 psia)	93.4 (21)	13000	2.88 (41.8)

Table 13 Predicted speed and supply pressure for hydrostatic lift-off, LOL

	Ramp Rate [rpm/s]	Supply Pressure at 15,000 rpm [bar (psia)]	Load [*N* (*lbf*)]	Lift-off speed [rpm]	Lift-off supply pressure [bar (psia)]
Case 6	8824	18.25 bar (264.7 psia)	31.1 (7)	0	1.98 (28.7)
Case 6	8824	18.25 bar (264.7 psia)	62.3 (14)	5000	2.46 (35.7)
Case 6	8824	18.25 bar (264.7 psia)	93.4 (21)	5500	2.81 (40.8)
Case 6	8824	18.25 bar (264.7 psia)	125 (28)	6500	3.70 (53.7)
Case 6	8824	18.25 bar (264.7 psia)	156 (35)	7000	4.12 (59.8)
Case 6	8824	18.25 bar (264.7 psia)	187 (42)	8000	5.22 (75.7)
Case 6	8824	18.25 bar (264.7 psia)	218 (49)	8500	5.84 (84.7)
Case 6	8824	18.25 bar (264.7 psia)	249 (56)	9000	6.46 (93.7)
Case 7	4412	18.25 bar (264.7 psia)	31.1 (7)	0	1.98 (28.7)
Case 7	4412	18.25 bar (264.7 psia)	62.3 (14)	500	2.25 (32.6)
Case 7	4412	18.25 bar (264.7 psia)	93.4 (21)	4000	2.81 (40.8)
Case 7	4412	18.25 bar (264.7 psia)	125 (28)	7500	3.43 (49.7)
Case 7	4412	18.25 bar (264.7 psia)	156 (35)	9000	4.12 (59.8)
Case 7	4412	18.25 bar (264.7 psia)	187 (42)	10000	4.67 (67.7)
Case 7	4412	18.25 bar (264.7 psia)	218 (49)	11000	6.05 (87.7)
Case 8	4412	9.63 bar (139.7 psia)	31.1 (7)	0	1.98 (28.7)
Case 8	4412	9.63 bar (139.7 psia)	62.3 (14)	8500	2.25 (32.6)
Case 8	4412	9.63 bar (139.7 psia)	93.4 (21)	9500	2.60 (37.7)
Case 8	4412	9.63 bar (139.7 psia)	125 (28)	11500	3.43 (49.7)
Case 8	4412	9.63 bar (139.7 psia)	156 (35)	12500	4.19 (60.8)
Case 9	2206	9.63 bar (139.7 psia)	31.1 (7)	0	1.98 (28.7)
Case 9	2206	9.63 bar (139.7 psia)	62.3 (14)	9000	2.25 (32.6)
Case 9	2206	9.63 bar (139.7 psia)	93.4 (21)	10000	2.81 (40.8)
Case 9	2206	9.63 bar (139.7 psia)	125 (28)	11500	3.56 (51.6)
Case 10	2206	5.32 bar (77.2 psia)	31.1 (7)	0	1.98 (28.7)
Case 10	2206	5.32 bar (77.2 psia)	62.3 (14)	12000	2.32 (33.6)
Case 10	2206	5.32 bar (77.2 psia)	93.4 (21)	13000	2.88 (41.8)

By the current definition of hydrostatic lift-off, Table 14 provides the observed speed, supply and recess pressure, pressure ratio, supply temperature, and flow rate at the point of hydrostatic lift-off for the LOR start-transient cases, which correspond to cases

1-5 in Table 9. The data for the LOL start-transient cases are in Table 15, which correspond to cases 6-10 in Table 9. Hydrodynamic lift-off occurs when the rotation of the rotor relative to the static bearing surface drags fluid into the film creating a wedge effect generating hydrodynamic pressures that overcome the forces acting on the rotor [16]. As with Borchard [5], no clear indication of hydrodynamic lift-off was observed.

Table 14 Hydrostatic lift-off data for start-transient testing with air, LOR

Ramp Rate [rpm/s]	Supply Pressure at 15,000 rpm [bar (psia)]	Unit Load [bar (psi)]	Direction of load [rad (deg)]	Speed [rpm]	Supply Pressure [bar (psia)]	Recess Pressure [bar (psia)]	Pressure Ratio	Supply Temperature [°C (°F)]	Flow Rate [kg/s]
8824	18.25 bar (264.7 psia)	0.263 (3.81)	0 (0)	0	2.08 (30.2)	1.98 (28.7)	0.95	19.8 (67.7)	0.0022
8824	18.25 bar (264.7 psia)	0.311 (4.51)	0 (0)	0	2.30 (33.4)	2.33 (33.8)	1.01	20.8 (69.4)	0.0025
8824	18.25 bar (264.7 psia)	0.433 (6.27)	0 (0)	5159	2.71 (39.3)	2.74 (39.8)	1.01	20.4 (68.7)	0.0050
8824	18.25 bar (264.7 psia)	0.614 (8.91)	0 (0)	5587	3.09 (44.8)	3.02 (43.9)	0.98	21.3 (70.3)	0.0065
8824	18.25 bar (264.7 psia)	0.823 (11.9)	0 (0)	7803	5.42 (78.6)	5.47 (79.3)	1.01	19.6 (67.2)	0.0125
8824	18.25 bar (264.7 psia)	1.05 (15.2)	0 (0)	8798	6.41 (92.9)	6.35 (92.1)	0.99	19.5 (67.0)	0.0142
8824	18.25 bar (264.7 psia)	1.28 (18.5)	0 (0)	10387	9.08 (132)	9.05 (131)	1.00	19.4 (67.0)	0.0183
8824	18.25 bar (264.7 psia)	1.53 (22.2)	0 (0)	12337	10.7 (155)	10.5 (152)	0.98	19.4 (66.9)	0.0205
4412	18.25 bar (264.7 psia)	0.263 (3.81)	0 (0)	0	2.01 (29.2)	1.90 (27.6)	0.95	20.8 (69.4)	0.0021
4412	18.25 bar (264.7 psia)	0.311 (4.51)	0 (0)	0	2.29 (33.3)	2.45 (35.5)	1.07	20.6 (69.1)	0.0023
4412	18.25 bar (264.7 psia)	0.433 (6.27)	0 (0)	2154	2.50 (36.2)	2.64 (38.2)	1.06	19.7 (67.4)	0.0033
4412	18.25 bar (264.7 psia)	0.614 (8.91)	0 (0)	7808	3.76 (54.5)	3.72 (54.0)	0.99	19.5 (67.1)	0.0057
4412	18.25 bar (264.7 psia)	0.823 (11.9)	0 (0)	7907	4.18 (60.7)	4.28 (62.0)	1.02	21.7 (71.7)	0.0062
4412	18.25 bar (264.7 psia)	1.05 (15.2)	0 (0)	11062	6.44 (93.5)	6.38 (92.5)	0.99	20.2 (68.3)	0.0114
4412	18.25 bar (264.7 psia)	1.28 (18.5)	0 (0)	12642	9.52 (138)	9.54 (138)	1.00	20.5 (68.8)	0.0182
4412	9.63 bar (139.7 psia)	0.263 (3.81)	0 (0)	0	1.67 (24.2)	1.77 (25.6)	1.06	20.7 (69.3)	0.0023
4412	9.63 bar (139.7 psia)	0.311 (4.51)	0 (0)	0	2.00 (29.0)	2.08 (30.2)	1.04	20.3 (68.6)	0.0021
4412	9.63 bar (139.7 psia)	0.433 (6.27)	0 (0)	7737	2.51 (36.4)	2.68 (38.9)	1.07	20.6 (69.1)	0.0029
4412	9.63 bar (139.7 psia)	0.614 (8.91)	0 (0)	10842	3.34 (48.5)	3.49 (50.6)	1.04	21.4 (70.6)	0.0047
4412	9.63 bar (139.7 psia)	0.823 (11.9)	0 (0)	11665	3.85 (55.8)	3.92 (56.8)	1.02	21.8 (71.3)	0.0057
2206	9.63 bar (139.7 psia)	0.263 (3.81)	0 (0)	0	1.92 (27.9)	1.89 (27.4)	0.98	18.6 (65.4)	0.0021
2206	9.63 bar (139.7 psia)	0.311 (4.51)	0 (0)	0	2.06 (29.9)	2.16 (31.4)	1.05	20.8 (69.4)	0.0022
2206	9.63 bar (139.7 psia)	0.433 (6.27)	0 (0)	10330	3.33 (48.2)	3.52 (51.0)	1.06	21.2 (70.1)	0.0041
2206	9.63 bar (139.7 psia)	0.614 (8.91)	0 (0)	10845	3.36 (48.7)	3.44 (49.9)	1.02	20.7 (69.3)	0.0044
2206	5.32 bar (77.2 psia)	0.263 (3.81)	0 (0)	0	2.08 (30.1)	2.00 (29.0)	0.96	20.9 (69.6)	0.0023
2206	5.32 bar (77.2 psia)	0.311 (4.51)	0 (0)	0	2.11 (30.6)	2.12 (30.7)	1.00	19.7 (67.5)	0.0024
2206	5.32 bar (77.2 psia)	0.433 (6.27)	0 (0)	9043	2.44 (35.4)	2.50 (36.2)	1.02	19.8 (67.7)	0.0026

Table 15 Hydrostatic lift-off data for start-transient testing with air, LOL

Ramp Rate [rpm/s]	Supply Pressure at 15,000 rpm [bar (psia)]	Unit Load [bar (psi)]	Direction of load [rad (deg)]	Speed [rpm]	Supply Pressure [bar (psia)]	Recess Pressure [bar (psia)]	Pressure Ratio	Supply Temperature [°C (°F)]	Flow Rate [kg/s]
8824	18.25 bar (264.7 psia)	0.282 (4.09)	0.705 (40.4)	0	1.70 (24.7)	1.78 (25.8)	1.05	20.6 (69.0)	0.0017
8824	18.25 bar (264.7 psia)	0.443 (6.42)	1.07 (61.0)	0	2.38 (34.6)	2.26 (32.7)	0.95	20.8 (69.4)	0.0033
8824	18.25 bar (264.7 psia)	0.659 (9.56)	1.24 (71.0)	4910	2.97 (43.1)	2.30 (33.4)	0.77	20.4 (68.7)	0.0068
8824	18.25 bar (264.7 psia)	0.898 (13.0)	1.33 (76.2)	6450	4.62 (67.0)	3.40 (49.2)	0.74	21.3 (70.4)	0.0106
8824	18.25 bar (264.7 psia)	1.15 (16.6)	1.38 (79.2)	8061	6.10 (88.5)	4.14 (60.1)	0.68	21.7 (71.0)	0.0139
8824	18.25 bar (264.7 psia)	1.41 (20.4)	1.42 (81.2)	8939	7.49 (109)	4.90 (71.1)	0.65	19.9 (67.8)	0.0164
8824	18.25 bar (264.7 psia)	1.68 (24.3)	1.44 (82.7)	9232	7.55 (110)	4.80 (69.6)	0.64	19.4 (67.0)	0.0157
8824	18.25 bar (264.7 psia)	1.97 (28.6)	1.46 (83.7)	10614	9.18 (133)	5.62 (81.5)	0.61	19.4 (67.0)	0.0182
4412	18.25 bar (264.7 psia)	0.282 (4.09)	0.705 (40.4)	0	2.26 (32.8)	2.12 (30.8)	0.94	20.8 (69.4)	0.0026
4412	18.25 bar (264.7 psia)	0.443 (6.42)	1.07 (61.0)	3236	2.45 (35.5)	2.12 (30.8)	0.87	20.5 (68.9)	0.0035
4412	18.25 bar (264.7 psia)	0.659 (9.56)	1.24 (71.0)	6747	3.52 (51.0)	2.71 (39.4)	0.77	20.3 (68.6)	0.0047
4412	18.25 bar (264.7 psia)	0.898 (13.0)	1.33 (76.2)	10263	5.13 (74.5)	3.58 (51.9)	0.70	21.5 (70.7)	0.0075
4412	18.25 bar (264.7 psia)	1.15 (16.6)	1.38 (79.2)	10835	5.81 (84.2)	3.95 (57.3)	0.68	19.8 (67.6)	0.0102
4412	18.25 bar (264.7 psia)	1.41 (20.4)	1.42 (81.2)	11282	6.89 (99.9)	4.36 (63.2)	0.63	19.7 (67.5)	0.0125
4412	18.25 bar (264.7 psia)	1.68 (24.3)	1.44 (82.7)	12920	9.64 (140)	6.36 (92.2)	0.66	19.7 (67.5)	0.0176
4412	9.63 bar (139.7 psia)	0.282 (4.09)	0.705 (40.4)	0	2.22 (32.1)	2.11 (30.6)	0.95	20.7 (69.3)	0.0025
4412	9.63 bar (139.7 psia)	0.443 (6.42)	1.07 (61.0)	0	2.05 (29.8)	1.83 (26.6)	0.89	18.2 (61.0)	0.0021
4412	9.63 bar (139.7 psia)	0.659 (9.56)	1.24 (71.0)	9885	2.89 (42.0)	2.20 (31.9)	0.76	20.8 (69.5)	0.0035
4412	9.63 bar (139.7 psia)	0.898 (13.0)	1.33 (76.2)	11989	4.12 (59.8)	3.03 (44.0)	0.74	21.5 (70.7)	0.0067
4412	9.63 bar (139.7 psia)	1.15 (16.6)	1.38 (79.2)	12980	5.00 (72.5)	3.25 (47.1)	0.65	17.9 (64.3)	0.0092
2206	9.63 bar (139.7 psia)	0.282 (4.09)	0.705 (40.4)	0	1.53 (22.1)	1.57(22.8)	1.03	19.2 (66.5)	0.0012
2206	9.63 bar (139.7 psia)	0.443 (6.42)	1.07 (61.0)	0	2.22 (32.2)	2.00 (29.0)	0.90	19.6 (67.2)	0.0028
2206	9.63 bar (139.7 psia)	0.659 (9.56)	1.24 (71.0)	10151	3.30 (47.9)	3.04 (44.1)	0.92	19.9 (67.9)	0.0040
2206	9.63 bar (139.7 psia)	0.898 (13.0)	1.33 (76.2)	11376	3.69 (53.5)	2.57 (37.2)	0.70	19.9 (67.9)	0.0045
2206	5.32 bar (77.2 psia)	0.282 (4.09)	0.705 (40.4)	0	2.49 (36.1)	2.22 (32.1)	0.89	19.5(67.2)	0.0031
2206	5.32 bar (77.2 psia)	0.443 (6.42)	1.07 (61.0)	0	2.25 (32.7)	2.12 (30.8)	0.94	21.0 (69.8)	0.0025
2206	5.32 bar (77.2 psia)	0.659 (9.56)	1.24 (71.0)	12688	2.84 (41.2)	2.41 (35.0)	0.85	21.2 (70.1)	0.0037

The pressure ratio for the LOR cases in Table 14 are nearly one; this is because the rotor is covering the recess where the recess pressure measurement is being taken. Since there is very little flow while the rotor is covering the recess, the recess pressure should equal the supply pressure. In the LOL case the rotor is forced to the side of the bearing on the land allowing for flow out of the bottom recess while the rotor is still in contact with the bearing and a pressure ratio less than one at hydrostatic lift-off. Also, as the applied unit load increases the pressure ratio at hydrostatic lift-off decreases. Even though the applied unit load is towards the side, gravity is forcing the rotor towards the bottom recess where the recess pressure measurement is being taken. Thus, a lower applied unit load results in a lower attitude angle, which may restrict flow out of the bottom recess and account for the higher pressure ratio in the LOL start-transient cases.

The start transient cases were conducted to see how hydrostatic lift-off (the speed and supply pressure that occur at hydrostatic lift-off) depends on the applied unit load, the final supply pressure at 15,000 *rpm*, and the ramp rate. Figure 22 shows the supply pressure at hydrostatic lift-off versus the applied unit load for the LOR start-transient test cases. The increasing applied unit load in Figure 22 for case 1 correspond to the proposed 1X - 8X applied unit loads in Table 9, while the applied unit loads for case 2 correspond to the 1X - 7X cases. Cases 1 and 2 have the same supply pressure of 18.25 *bar* (264.7 *psia*) at 15,000 *rpm* but differ in that the ramp rate in case 2 is half of case 1 at 4412 *rpm/s*.

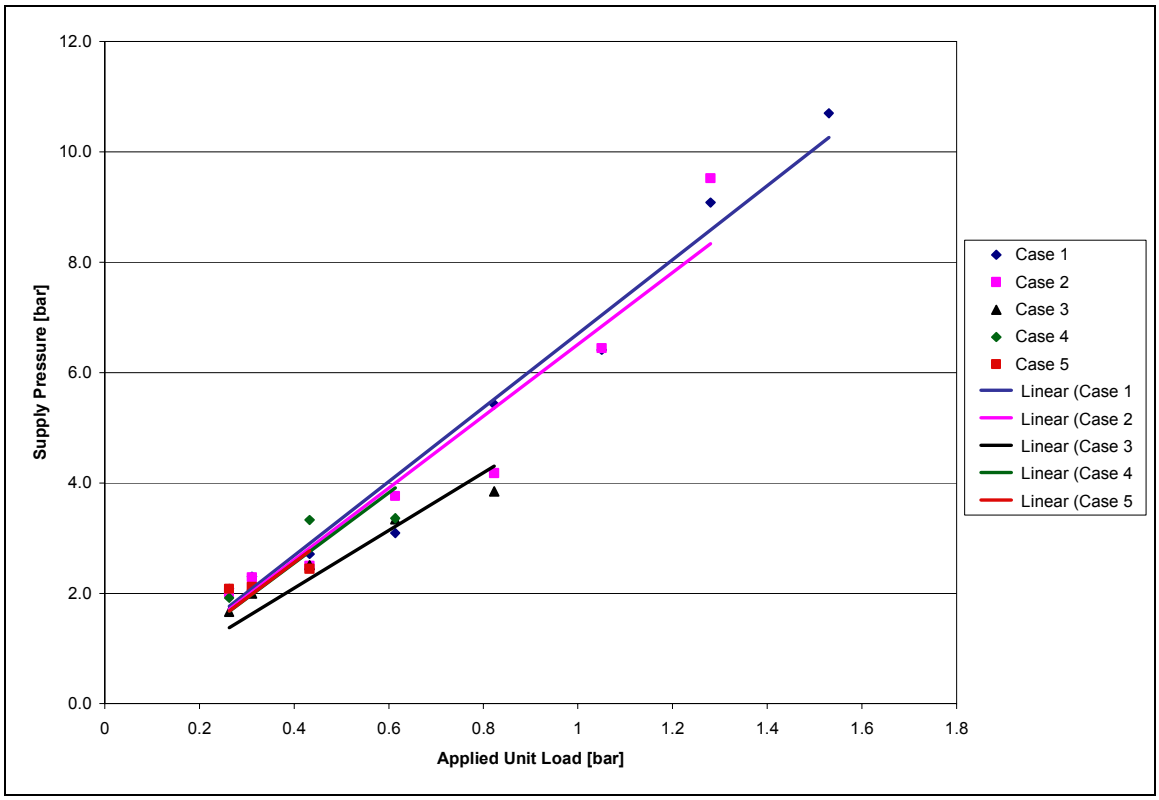

Fig. 22 Hydrostatic lift-off supply pressure versus applied unit load for the LOR cases

The increasing applied unit load for cases 3, 4, and 5 in Figure 22 correspond to the 1X – 5X, 1X – 4X, and 1X – 3X applied unit loads in Table 9, respectively. The ramp rate in case 3 is the same as case 2 but the supply pressure at 15,000 *rpm* is 9.63 *bar* (139.7 *psia*). The supply pressure in case 4 is the same as case 3 but the ramp rate is 2206 *rpm/s*. Case 4 and 5 have the same ramp rate but the supply pressure in case 5 is 5.32 *bar* (77.2 *psia*).

Figure 23 shows the supply pressure at hydrostatic lift-off versus the applied unit load for the LOL start-transient test cases. Similar to Figure 22, the increasing applied unit load in Figure 23 correspond to the increasing applied unit loads for cases 6-10 in Table 9. Also, the previously described similarities and differences between cases 1-5 are the same as cases 6-10, respectively. Note that the 1X cases in Figure 23 have a higher hydrostatic lift-off supply pressure than the trend lines. This is because hydrostatic lift-off occurred before the start of the start transient test, and the lowest recorded supply pressure is the hydrostatic lift-off supply pressure. Figure 22 and Figure

23 both support the following conclusion; the required supply pressure for hydrostatic lift-off is approximately a linear function of the applied unit load.

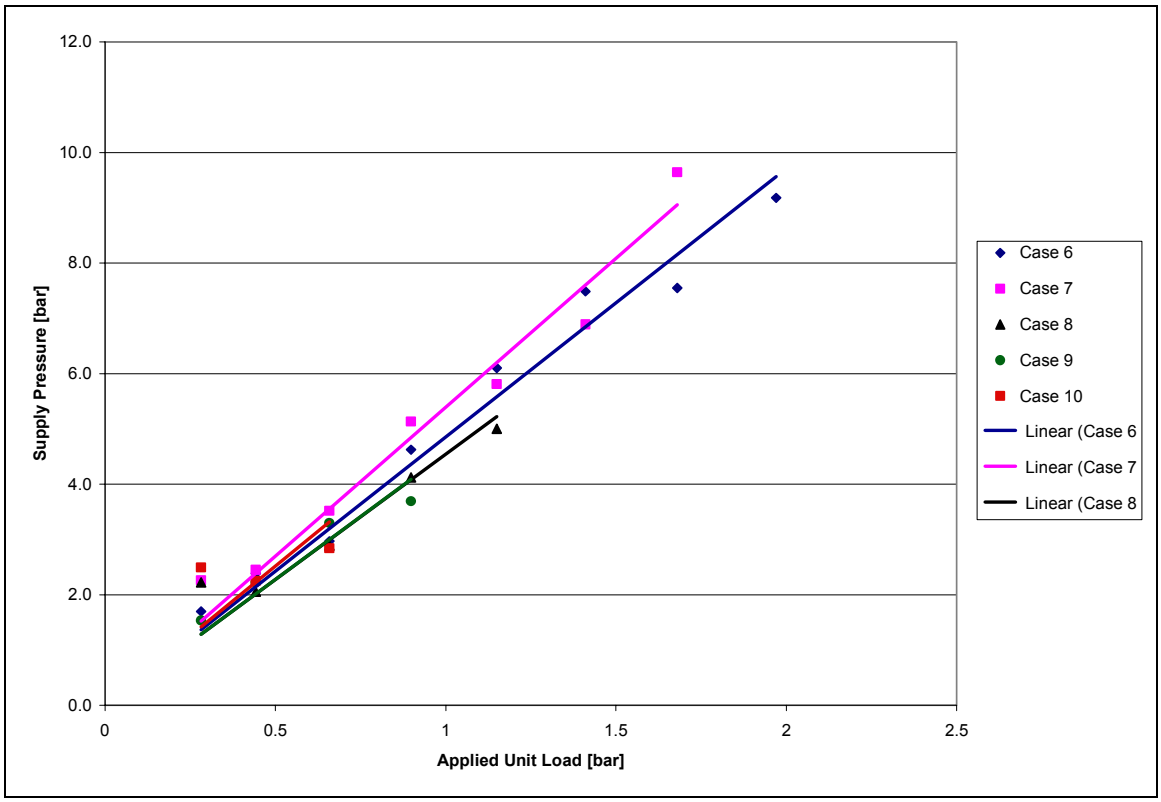

Fig. 23 Hydrostatic lift-off supply pressure versus applied unit load for the LOL cases

To understand how the supply pressure at 15,000 *rpm* affects hydrostatic lift-off, cases with similar ramp rates and direction of the applied unit load but different supply pressures at 15,000 *rpm* are compared. Case 2 and case 3 are both LOR start-transient cases and have the same ramp rate of 4412 *rpm/s*. However, the supply pressure at 15,000 *rpm* in case 2 is 18.25 *bar* (264.7 *psia*) and 9.63 *bar* (139.7 *psia*) in case 3. As the supply pressure drops from case 2 to case 3, the required supply pressure for hydrostatic lift-off in Figure 22 appears to decreases. This conclusion is supported by comparing cases 7 to 8 in Figure 23, which are both LOL start-transient cases. Both have the same ramp rate but, as with cases 2 and 3, differ in supply pressure at 15,000 *rpm*. Comparing cases 4 to 5, or cases 9 to 10 does not support this conclusion, the change in supply pressure at 15,000 *rpm* shows no change in hydrostatic lift-off supply pressure. However, this may be due to the small sample size due to the limit in applied unit load.

Lowering the supply pressure at 15,000 *rpm* may reduce the required supply pressure for hydrostatic lift-off but this may be ambiguous as cases 3-5 and cases 8-10 pass through a critical speed.

Figure 24 displays the reason that dropping the supply pressure at 15,000 *rpm* may lower the required supply pressure for hydrostatic lift-off. While the required supply pressure for hydrostatic lift-off in case 3 is less than case 2, the speed at which lift-off occurs in case 3 is much higher than in case 2. The supply pressure at hydrostatic lift-off may be reduced with a lower supply pressure at 15,000 *rpm* due to an increased hydrodynamic effect at high speeds.

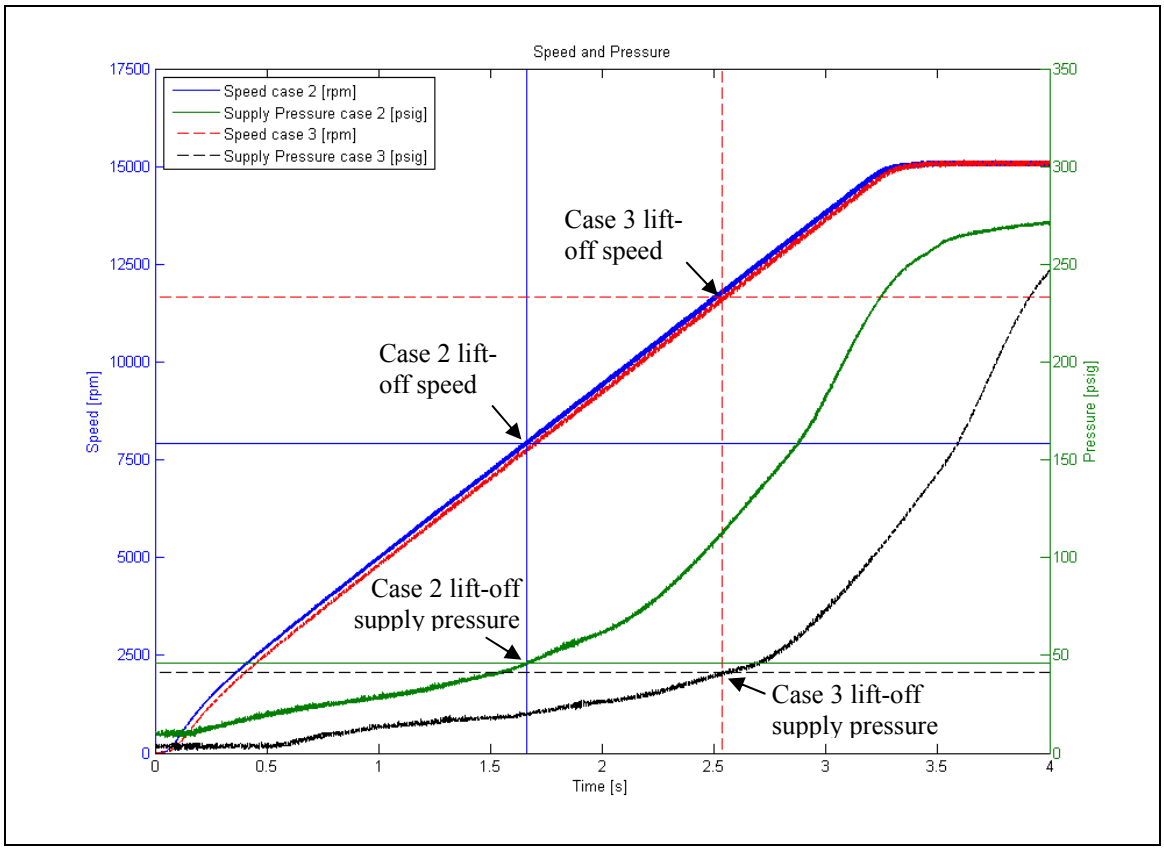

Fig. 24 Case 2_5X vs. Case 3_5X hydrostatic lift-off speed and pressure

Cases 1 and 2 in Figure 22 support the following conclusion: changing the ramp rate while keeping the supply pressure at 15,000 *rpm* constant has no significant impact. The impact of the ramp rate can also be investigated by comparing case 3 to case 4. Cases 3 and 4 have the same supply pressure at 15,000 *rpm* but the ramp rate in case 4 is

half that of case 3 at 2206 *rpm/s*. Here it appears that decreasing the ramp rate from 4412 *rpm/s* to 2206 *rpm/s* increases the required supply pressure for hydrostatic lift-off. Similar to the comparison of case 1 and 2, case 6 has the same supply pressure at 15,000 *rpm* as case 7 but the ramp rate for case 7 is half that of case 6 at 4412 *rpm/s*. This comparison supports the same conclusion as case 1 and 2. The comparison of case 8 to case 9 also supports this conclusion. The similarities of supply pressure at 15,000 *rpm* and the difference in ramp rate between cases 8 and 9 are the same as cases 3 and 4. It appears that the ramp rate while keeping the supply pressure constant has no significant impact.

As described previously, the supply pressure depends on the speed squared. Figure 25 displays the hydrostatic lift-off speed versus the applied unit load for the LOR start-transient test cases. The increasing applied unit loads correspond to the increasing unit loads in Table 9. In the 1X and 2X cases in Figure 25, the event of hydrostatic lift-off occurs before the motor starts at 0 *rpm*. Hydrostatic lift-off speed in Figure 25 increases from case 1 to 2, case 2 to 3, 3 to 4, but decreases from case 4 to 5. Making any clear conclusions from the hydrostatic lift-off speed is futile. Since hydrostatic lift-off occurs in the 1X and 2X applied unit load cases at 0 rpm and the hydrostatic lift-off supply pressure does not appear to have any significant change due to the change in supply pressure at 15,000 *rpm* or ramp rate, the event of hydrostatic lift-off does not depend on speed. Any appearance of a trend is due to the dependence of speed on the supply pressure at lift-off. These conclusions are similar for the LOL start-transient test cases as seen in Figure 26.

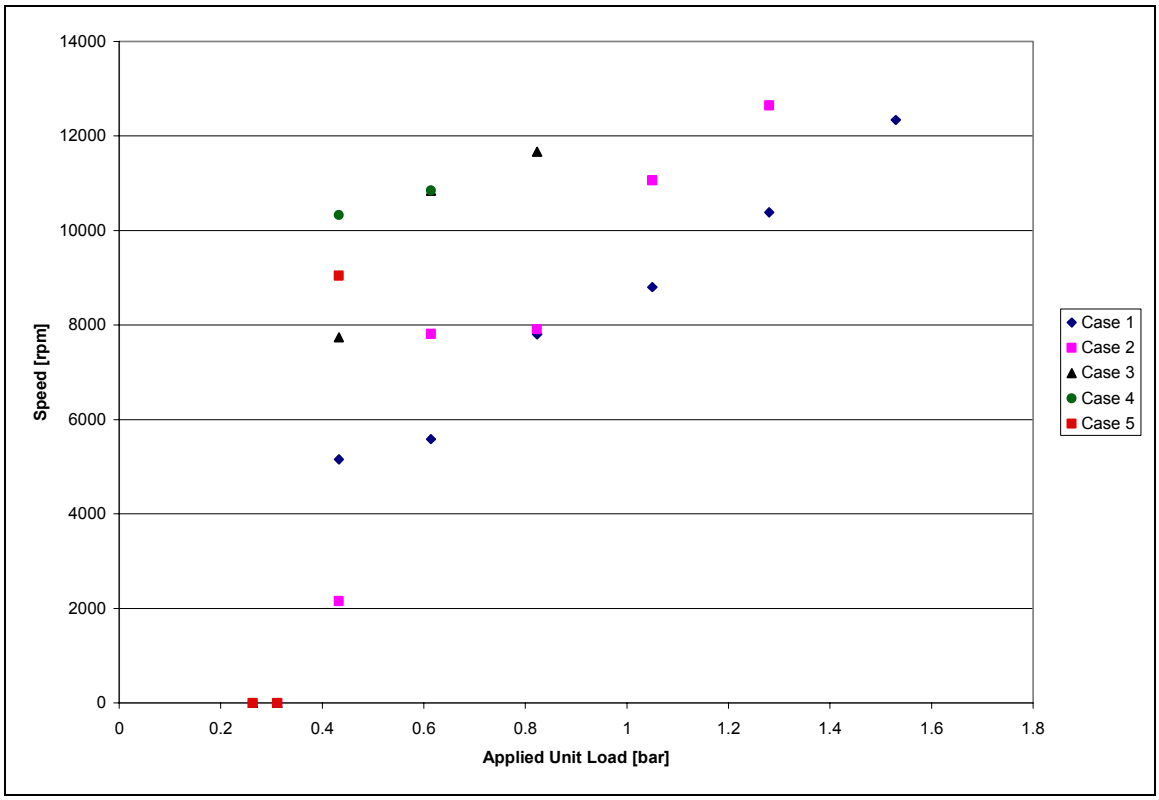

Fig. 25 Hydrostatic lift-off speed versus applied unit load for the LOR cases

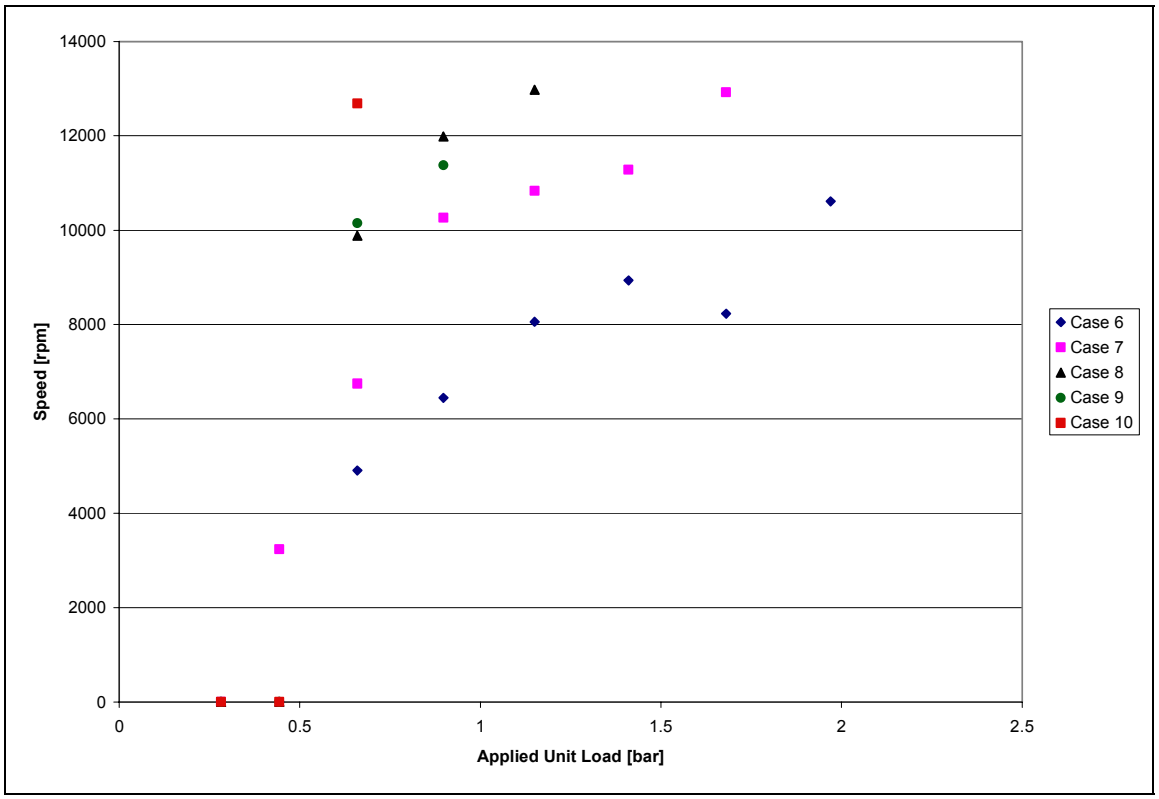

Fig. 26 Hydrostatic lift-off speed versus unit load for the LOL cases

Figure 27 shows the hydrostatic lift-off supply pressure versus the applied unit load for cases 1 and 2 and cases 6 and 7 in Table 9. Cases 1 and 2 are LOR start-transient cases, while cases 6 and 7 are LOL start-transient cases. Figure 27 supports the conclusion that the required supply pressure for hydrostatic lift-off is approximately a linear function of the applied unit load. Figure 27 also supports the following conclusion; the required hydrostatic lift-off supply pressure is less for the LOL start-transient test cases.

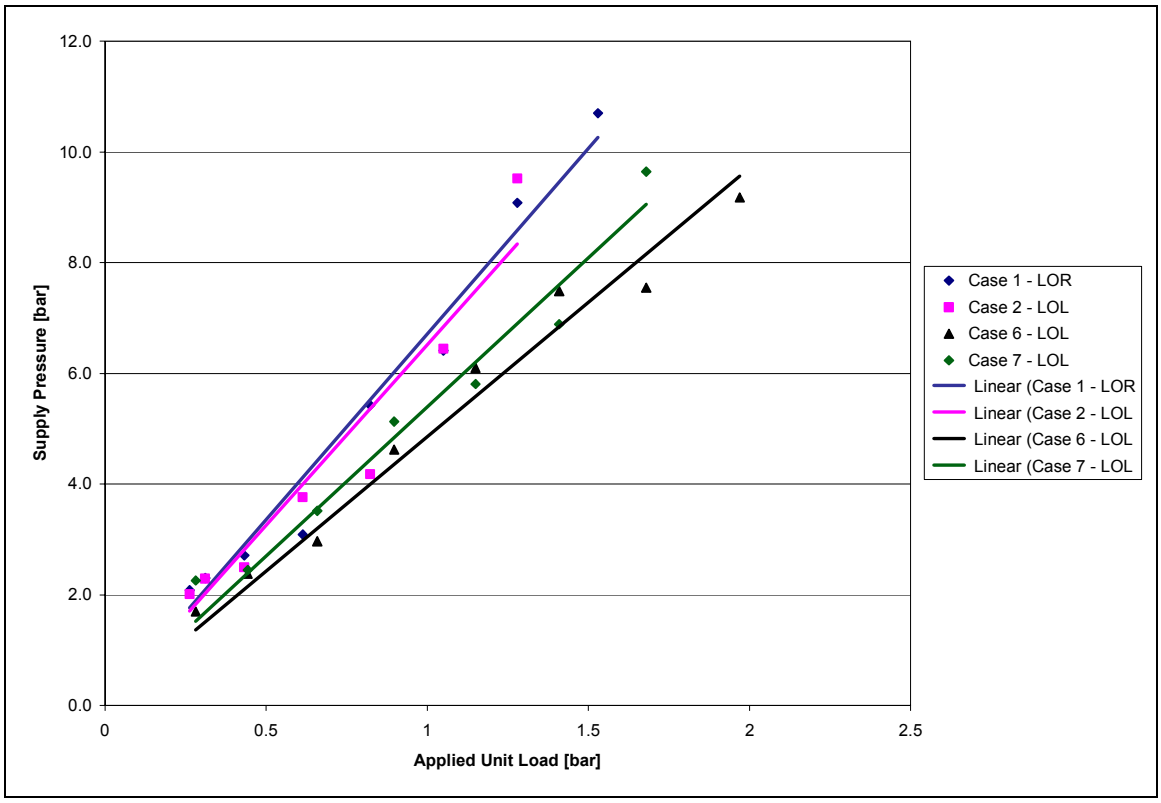

Fig. 27 Supply pressure at lift-off versus unit load for cases 1, 2 (LOR), 6, and 7 (LOL)

Table 12 and Table 13 detailed the predicted speed and supply pressure at hydrostatic lift-off. Contrary to Figure 27, which shows hydrostatic lift-off for the LOL cases occurring at a lower supply pressure for a given applied unit load than the LOR, the predicted results for the LOR and LOL cases do not show a difference between the two in Figure 28. Figure 28 shows the supply pressure at hydrostatic lift-off versus the applied unit load for the predicted and actual results in the 100% torque-100% pressure 1X LOR

and LOL cases. The supply pressure required for hydrostatic lift-off is predicted to increase with increasing applied unit load, but the LOR test cases show a higher supply pressure required for hydrostatic lift-off. The predicted supply pressure for hydrostatic lift-off in the LOL cases follows the test results rather closely. XLHydroJet® predicts each input as a steady state; therefore the ramp rate is not taken into account.

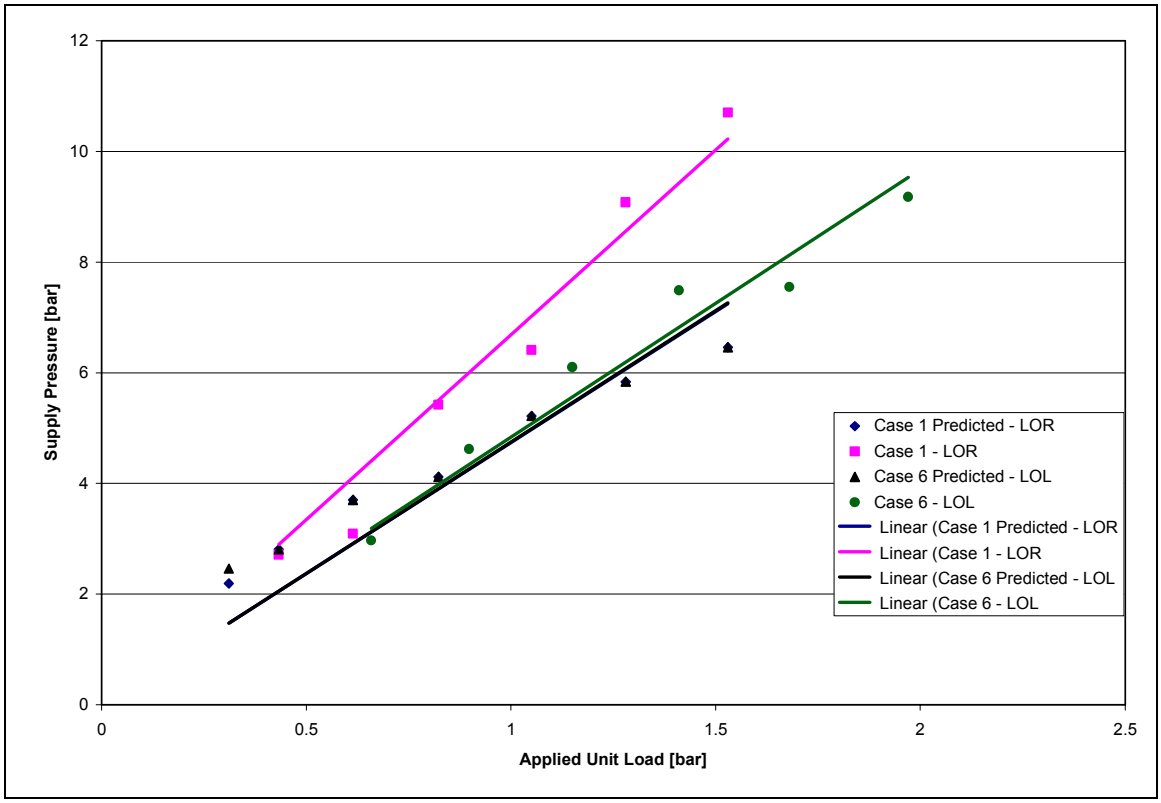

Fig. 28 Predicted and actual hydrostatic lift-off supply pressure versus applied unit load for cases 1 (LOR) and 6 (LOL)

Comparing Forward and Backward 1X Synchronous Amplitudes

A second approach to determine hydrostatic lift-off is to compare the amplitude of the backward 1X synchronous line to the trend of the forward 1X synchronous line. If the rotor is forced to the side of the bearing and constrained to move back and forth along the outside of the bearing, similar to Figure 19, the forward and backward whirl should be similar. Figure 29 displays the amplitudes of the forward and backward 1X synchronous lines in the 100% torque-100% pressure, 6X static unit load, LOR case. Near 9,204 *rpm* the amplitude of the backward whirl decreases while the amplitude of the forward whirl increases, indicating hydrostatic lift-off. This compares to the value in

Table 14 of 8,798 *rpm* for the graphical method. Table 16 details the speed of hydrostatic lift-off using this alternate procedure.

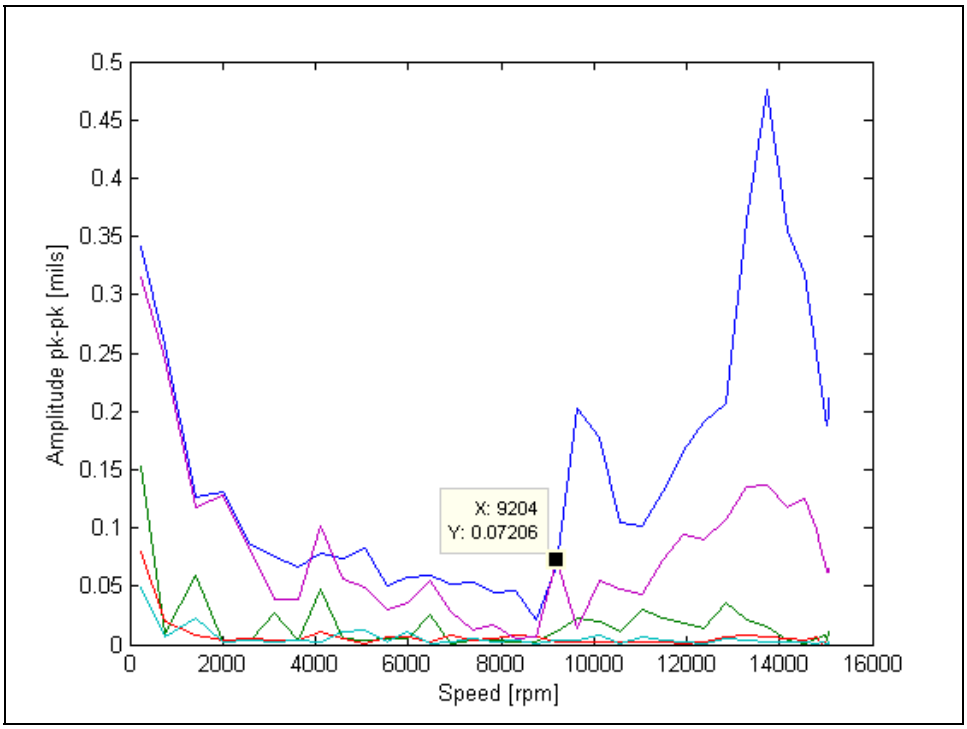

Fig. 29 Forward and backward amplitude for the 100% torque-100% pressure, 6X static unit load, LOR

Table 16 Hydrostatic lift-off as defined by comparison of the amplitude for the synchronous forward and backward whirl

	Ramp Rate [rpm/s]	Supply Pressure at 15,000 rpm [bar (psia)]	Unit Load [bar (psi)]	Lift-off forward vs. backward [rpm]		Ramp Rate [rpm/s]	Supply Pressure at 15,000 rpm [bar (psia)]	Unit Load [bar (psi)]	Lift-off forward vs. backward [rpm]
Case 1	8824	18.25 bar (264.7 psia)	0.263 (3.81)	0	Case 6	8824	18.25 bar (264.7 psia)	0.282 (4.09)	0
Case 1	8824	18.25 bar (264.7 psia)	0.311 (4.51)	0	Case 6	8824	18.25 bar (264.7 psia)	0.443 (6.42)	0
Case 1	8824	18.25 bar (264.7 psia)	0.433 (6.27)	4338	Case 6	8824	18.25 bar (264.7 psia)	0.659 (9.56)	5023
Case 1	8824	18.25 bar (264.7 psia)	0.614 (8.91)	5912	Case 6	8824	18.25 bar (264.7 psia)	0.898 (13.0)	6462
Case 1	8824	18.25 bar (264.7 psia)	0.823 (11.9)	9116	Case 6	8824	18.25 bar (264.7 psia)	1.15 (16.6)	6455
Case 1	8824	18.25 bar (264.7 psia)	1.05 (15.2)	9204	Case 6	8824	18.25 bar (264.7 psia)	1.41 (20.4)	8302
Case 1	8824	18.25 bar (264.7 psia)	1.28 (18.5)	9665	Case 6	8824	18.25 bar (264.7 psia)	1.68 (24.3)	8014
Case 1	8824	18.25 bar (264.7 psia)	1.53 (22.2)	11020	Case 6	8824	18.25 bar (264.7 psia)	1.97 (28.6)	8827
Case 2	4412	18.25 bar (264.7 psia)	0.263 (3.81)	0	Case 7	4412	18.25 bar (264.7 psia)	0.282 (4.09)	0
Case 2	4412	18.25 bar (264.7 psia)	0.311 (4.51)	0	Case 7	4412	18.25 bar (264.7 psia)	0.443 (6.42)	0
Case 2	4412	18.25 bar (264.7 psia)	0.433 (6.27)	4422	Case 7	4412	18.25 bar (264.7 psia)	0.659 (9.56)	4868
Case 2	4412	18.25 bar (264.7 psia)	0.614 (8.91)	5605	Case 7	4412	18.25 bar (264.7 psia)	0.898 (13.0)	7583
Case 2	4412	18.25 bar (264.7 psia)	0.823 (11.9)	8514	Case 7	4412	18.25 bar (264.7 psia)	1.15 (16.6)	8081
Case 2	4412	18.25 bar (264.7 psia)	1.05 (15.2)	10590	Case 7	4412	18.25 bar (264.7 psia)	1.41 (20.4)	8645
Case 2	4412	18.25 bar (264.7 psia)	1.28 (18.5)	11850	Case 7	4412	18.25 bar (264.7 psia)	1.68 (24.3)	12620
Case 3	4412	9.63 bar (139.7 psia)	0.263 (3.81)	0	Case 8	4412	9.63 bar (139.7 psia)	0.282 (4.09)	0
Case 3	4412	9.63 bar (139.7 psia)	0.311 (4.51)	0	Case 8	4412	9.63 bar (139.7 psia)	0.443 (6.42)	0
Case 3	4412	9.63 bar (139.7 psia)	0.433 (6.27)	5575	Case 8	4412	9.63 bar (139.7 psia)	0.659 (9.56)	7636
Case 3	4412	9.63 bar (139.7 psia)	0.614 (8.91)	9637	Case 8	4412	9.63 bar (139.7 psia)	0.898 (13.0)	10670
Case 3	4412	9.63 bar (139.7 psia)	0.823 (11.9)	12620	Case 8	4412	9.63 bar (139.7 psia)	1.15 (16.6)	11570
Case 4	2206	9.63 bar (139.7 psia)	0.263 (3.81)	0	Case 9	2206	9.63 bar (139.7 psia)	0.282 (4.09)	0
Case 4	2206	9.63 bar (139.7 psia)	0.311 (4.51)	0	Case 9	2206	9.63 bar (139.7 psia)	0.443 (6.42)	0
Case 4	2206	9.63 bar (139.7 psia)	0.433 (6.27)	7400	Case 9	2206	9.63 bar (139.7 psia)	0.659 (9.56)	7910
Case 4	2206	9.63 bar (139.7 psia)	0.614 (8.91)	10080	Case 9	2206	9.63 bar (139.7 psia)	0.898 (13.0)	10410
Case 5	2206	5.32 bar (77.2 psia)	0.263 (3.81)	0	Case 10	2206	5.32 bar (77.2 psia)	0.282 (4.09)	0
Case 5	2206	5.32 bar (77.2 psia)	0.311 (4.51)	0	Case 10	2206	5.32 bar (77.2 psia)	0.443 (6.42)	0
Case 5	2206	5.32 bar (77.2 psia)	0.433 (6.27)	10050	Case 10	2206	5.32 bar (77.2 psia)	0.659 (9.56)	11830

Both methods for determining hydrostatic lift-off reveal similar trends. However, a comparison of the amplitude for the forward and backward whirl is limited by the steps between each point, and there is not always a clear distinction when the forward and backward whirl deviate.

Ramp Rate

The ramp rate (drive torque) parameter is varied for different start-transient test cases. The ROCETS predictions accelerated from zero to 15,000 *rpm* over 1.7 *seconds*, which is referred to as 100% torque. If the acceleration to 15,000 *rpm* takes 3.4 *seconds* or 6.8 *seconds*, it is referred to as 50% torque or 25% torque, respectively. Figure 30 confirms that the acceleration to 15,000 *rpm* takes twice or four times as long, but also that there is a reduction in torque of 50 and 25%. The percent difference between the maximum drive torque for the 100% torque and 50% torque or 25% torque cases is not 50 and 25 percent, because the maximum drive torque for the 100% torque case is limited by the motor at 11 *N-m* (8.1 *ft-lbs*). However, a comparison of the drive torque before the drop to 0.30 *N-m* (0.22 *ft-lbs*) at a steady 15,000 *rpm* does confirm the reduction in drive torque of 50 and 25 percent, respectively.

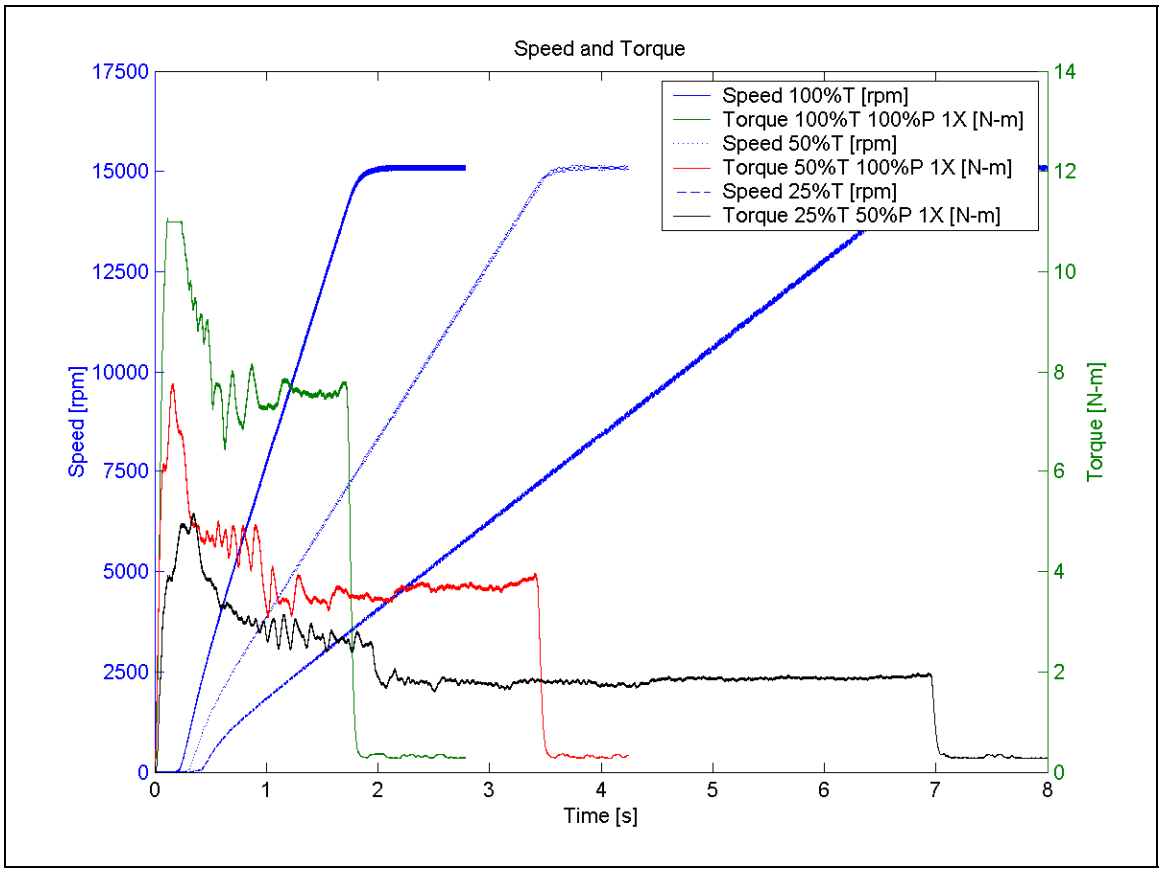

Fig. 30 Drive torque for varying ramp rates

Hydrostatic lift-off may also be estimated by a comparison in drive torque for a 1X case to a higher load case. Figure 31 shows the 100% torque-100% pressure, 1X static weight case compared to the similar 8X case. Hydrostatic lift-off was determined graphically by the rotor centerline plot at the point the eccentricity remained 0.00254 *mm* (0.1 *mils*) above C_r. The point of hydrostatic lift-off for the 8X case is shown in Figure 31.

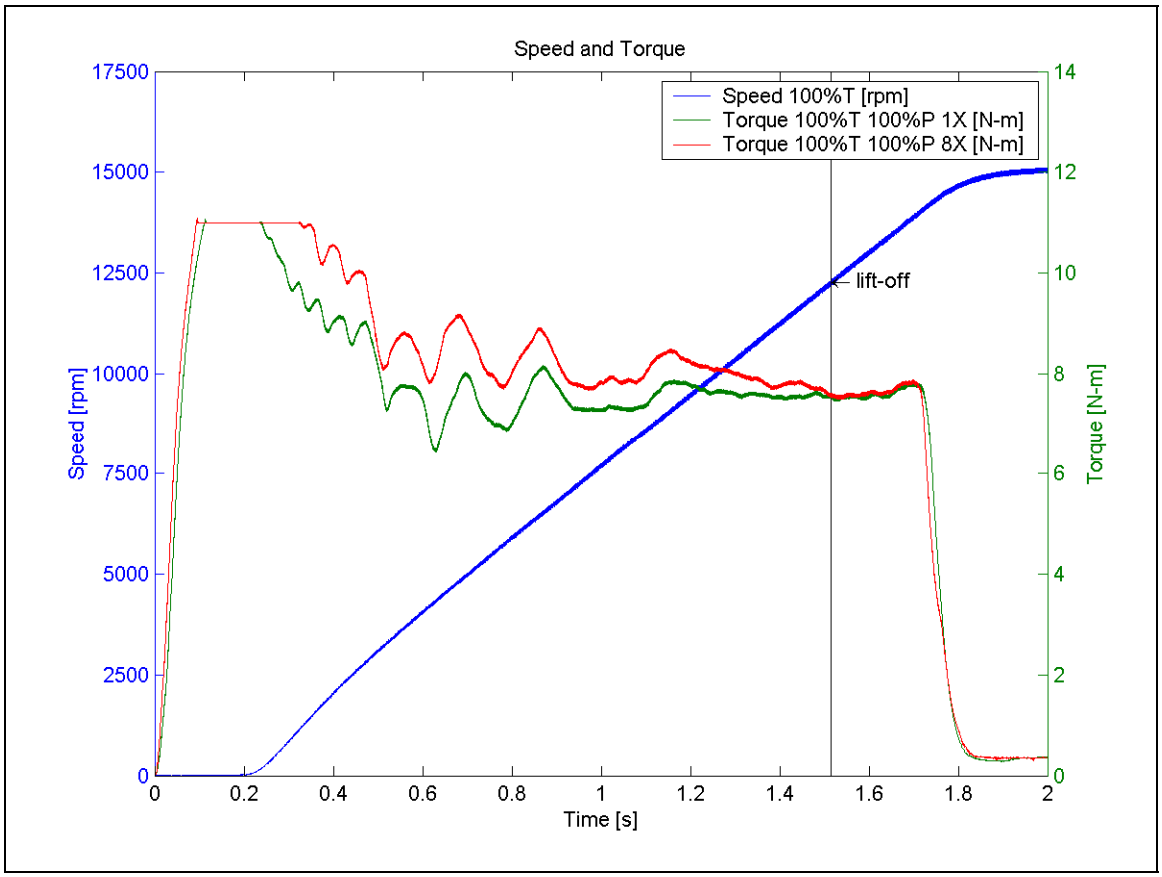

Fig. 31 Torque and speed versus time for 100% torque-100% pressure 1X and 8X static unit load, LOR

Note how the torque for the 8X case follows the 1X case after the point of hydrostatic lift-off, yet before requires more drive torque to maintain the same speed. The similarity in drive torque after the point of hydrostatic lift-off is due to the absence of metal-to-metal contact in both cases, an indication that both have hydrostatically lifted-off.

This method may only be used in comparing similar cases; for instance, cases with the same ramp rate and supply pressures at 15,000 *rpm*. Also, careful attention must be made that the rotor in the baseline (1X case) is not in contact with the bearing throughout the start-transient. Metal-to-metal contact due to rubbing before hydrostatic lift-off or a rub while passing through a critical speed will result in a higher torque. Also, comparing cases with a similar applied unit load, such as a 1X and 4X cases, makes the determination of hydrostatic lift-off difficult as the drive torque in each case is similar. Therefore, comparison of the drive torque only confirms the method for determining

hydrostatic lift-off by the rotor centerline plot but does not itself provide a new method. No observation of hydrodynamic lift-off would be obtained by the drive torque data.

Water Versus Air

Borchard [5] completed many start-transients of a hybrid bearing in water. He also defined hydrostatic lift-off as the point of departure towards the center of the bearing. Figure 32 shows the orbit plot from the start-transient case 1 with a 1X rotor weight static load in the vertical direction. Five different points were defined for the start-transient with point 2 as the inception of hydrostatic lift-off at 4,275 *rpm*.

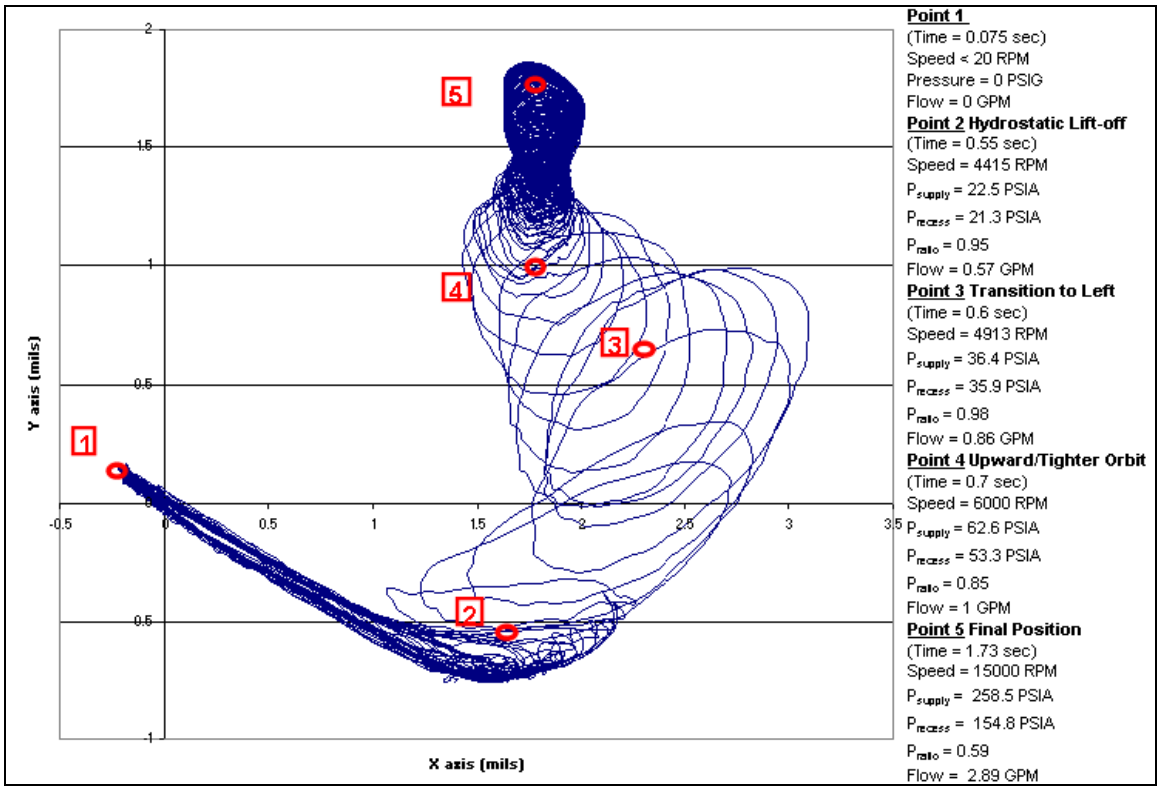

Fig. 32 Case 1 test result with 1X rotor weight static load from Borchard [5]

Continuing with case 1, Borchard [5] increased the load from 1X rotor weight static load to 8X rotor weight static load. With an 8X rotor weight, static load hydrostatic lift-off occurred at 7,900 *rpm*, meaning that the rotor was in contact with the bearing longer with increased load.

In cases 6-10, the static load was applied in the horizontal direction (side) between two pockets (on land). Figure 33 shows the orbit plot from the start-transient case 6 with a 1X rotor weight static side load. Hydrostatic lift-off occurred at 8,700 *rpm* for the 1X rotor weight static side load, and at 12,640 *rpm* for the 8X rotor weight static side load. Again, more load applied to the rotor results in a greater lift-off speed.

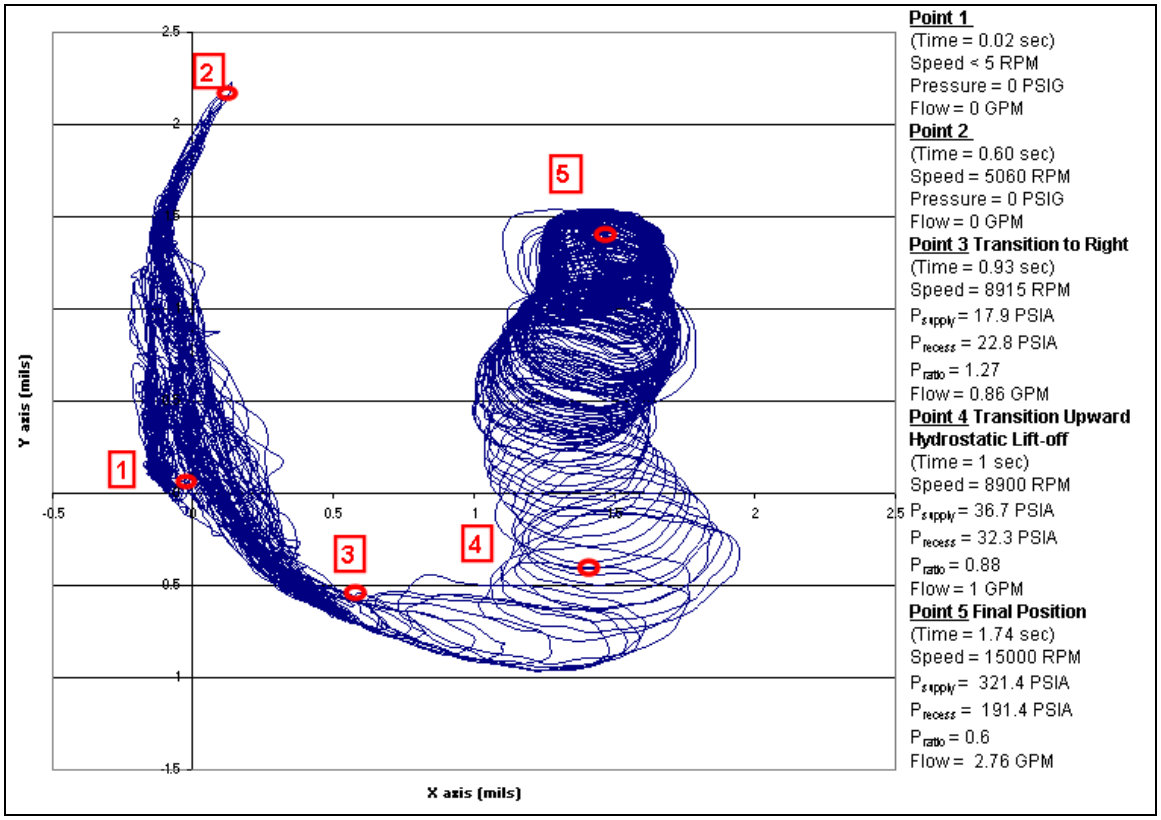

Fig. 33 Case 6 test result with 1X rotor weight static side load from Borchard [5]

Table 17 shows the speed at which hydrostatic lift-off occurred for each start-transient. A more compelling comparison would be to include the supply and recess pressure as hydrostatic lift-off is highly pressure dependent.

Table 17 Hydrostatic lift-off speeds for hybrid bearing in water

	Ramp Rate [rpm/s]	Pressure @ 15,000 [rpm]	Load Orientation	Multiples of Rotor Weight Test Results (Hydrostatic Lift-off Speed [rpm])							
				1X	2X	3X	4X	5X	6X	7X	8X
Case 1	8824	18.3 [bar] (264.7 [psia])	Load on Pad (Vertical)	4,275	5,950	6,000	6,400	6,750	6,300	7,300	7,900
Case 2	4412	18.3 [bar] (264.7 [psia])	Load on Pad (Vertical)	3,025	4,525	3,785	5,410	4,320	4,650	6,030	6,880
Case 3	4412	9.63 [bar] (139.7 [psia])	Load on Pad (Vertical)	2,915	8,750	9,240	7,830	8,815	9,250	11,030	11,760
Case 4	2206	9.63 [bar] (139.7 [psia])	Load on Pad (Vertical)	3,265	2,735	4,460	4,995	8,120	8,915	10,510	11,290
Case 5	2206	5.32 [bar] (77.2 [psia])	Load on Pad (Vertical)	2,080	4,280	6,795	8,800	9,365	10,600	13,285	14,315
Case 6	8824	18.3 [bar] (264.7 [psia])	Load on Land (Horizontal)	N/A	8,700	11,155	10,375	12,420	11,280	11,425	12,640
Case 7	4412	18.3 [bar] (264.7 [psia])	Load on Land (Horizontal)	N/A	7,140	8,015	8,540	9,125	10,250	11,100	11,620
Case 8	4412	9.63 [bar] (139.7 [psia])	Load on Land (Horizontal)	N/A	7,415	8,060	9,000	9,000	9,680	11,600	12,040
Case 9	2206	9.63 [bar] (139.7 [psia])	Load on Land (Horizontal)	N/A	4,195	4,810	5,635	7,840	8,335	10,570	11,515
Case 10	2206	5.32 [bar] (77.2 [psia])	Load on Land (Horizontal)	N/A	4,575	7,355	8,295	9,105	11,950	14,355	14,945

Besides comparing the orbit plots from one start-transient to another, Borchard [5] also made comparisons using the drive torque data from the motor. Borchard [5] described the possible inception of hydrodynamic lift-off as a decrease in drive torque indicating earlier lift-off. However, this is a qualitative observation as no speed for hydrodynamic lift-off is given. Also, the reduction in torque for the 8X case occurred after the 1X case confirming that lift-off occurs at a higher speed with increased load. Borchard [5] also noted by observing torque data from other cases that reducing the ramp rate did in fact decrease the starting torque.

Each start-transient rubbed before the inception of hydrostatic lift-off. After more than 100 start-transient tests, the rotor surface did reveal burnishing while burnishing and pitting were observed on the hybrid bearing surface as displayed in Figure 34 and Figure 35.

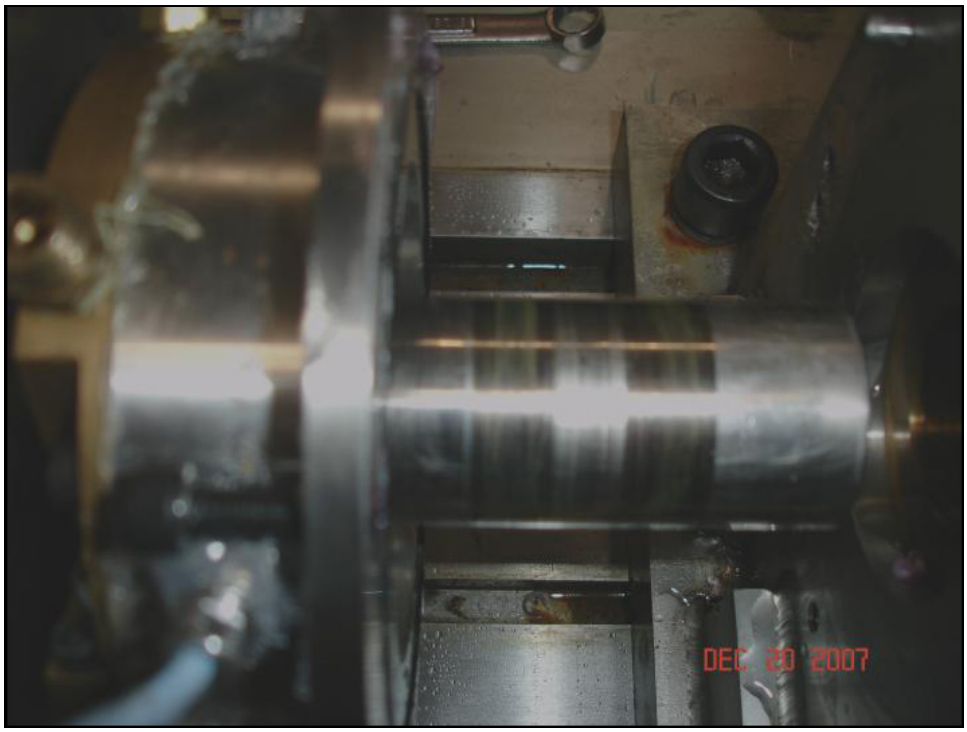

Fig. 34 Burnishing of the rotor observed after testing by Borchard [5]

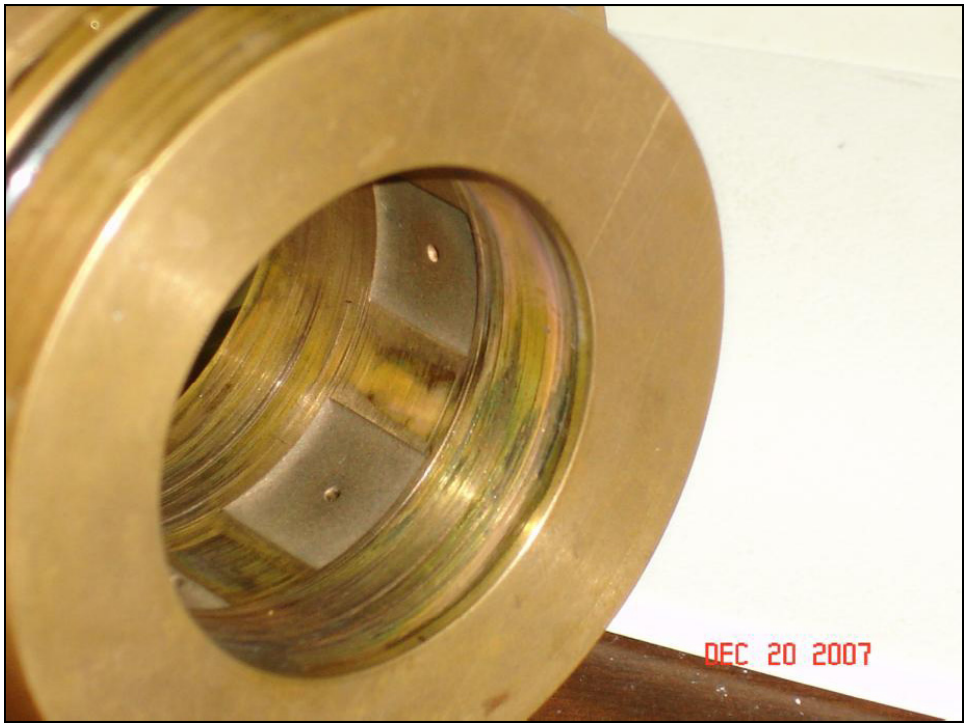

Fig. 35 Burnishing and pitting of the hybrid bearing observed after testing by Borchard [5]

Similar trends between the start-transient testing with water and air exist. Hydrostatic lift-off was determined using a graphical method and is highly pressure dependent, hydrostatic lift-off speed (thus pressure required for hydrostatic lift-off) increased with increasing load, and damage to the rotor and bearing surface incurred due to rubbing. Because hydrostatic lift-off is highly pressure dependent, and the pressure to speed squared is not in the same proportion between each test, no further comparisons are made.

Differences in the start-transient testing with water and air are that pneumatic hammer instability was observed with air and must be predicted and avoided during testing. Very little damping is present with air, and there is a significant drop in the first and second natural frequencies. Therefore, passing through a critical speed was completed successfully but not without rubbing.

Bearing Before and After

During start-transient testing of a hybrid bearing with air, wear occurs due to metal-to-metal contact before hydrostatic lift-off or rubbing while passing through a critical speed. This section briefly compares the rotor and bearing surfaces before and after excess of 100 start-transient tests. Figures 36 and 37 show the rotor before start-transient testing and burnishing of the rotor following testing.

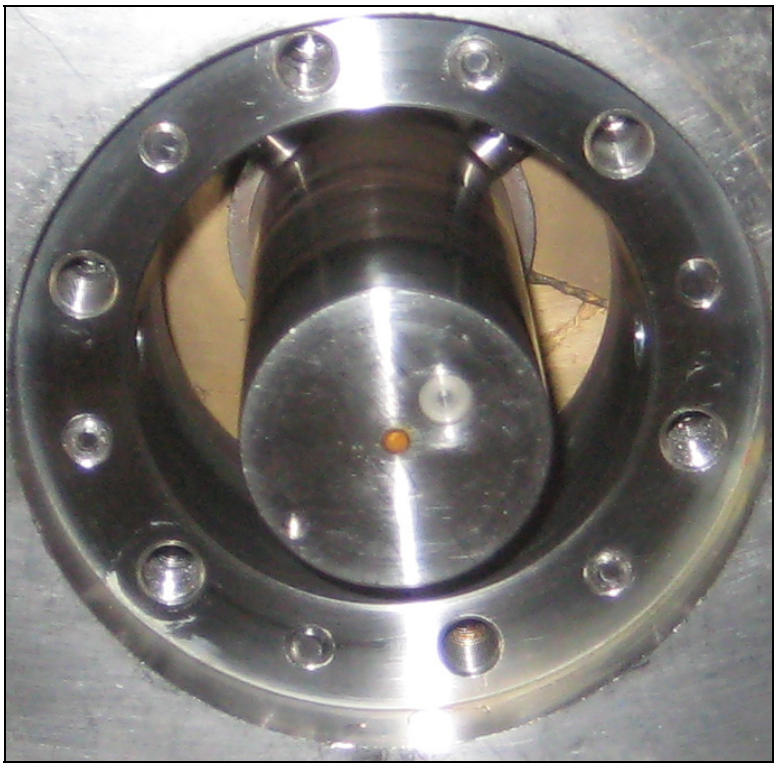

Fig. 36 Rotor before start-transient testing

Fig. 37 Burnishing of the rotor after start-transient testing

Figures 38 and 39 show the bearing surface in the direction of the LOR applied unit load before and after start-transient testing. While Figures 40 and 41 show a similar comparison in the direction of the LOL applied unit load. Figure 42 displays the burnishing of the bearing surface in both direction of applied unit load.

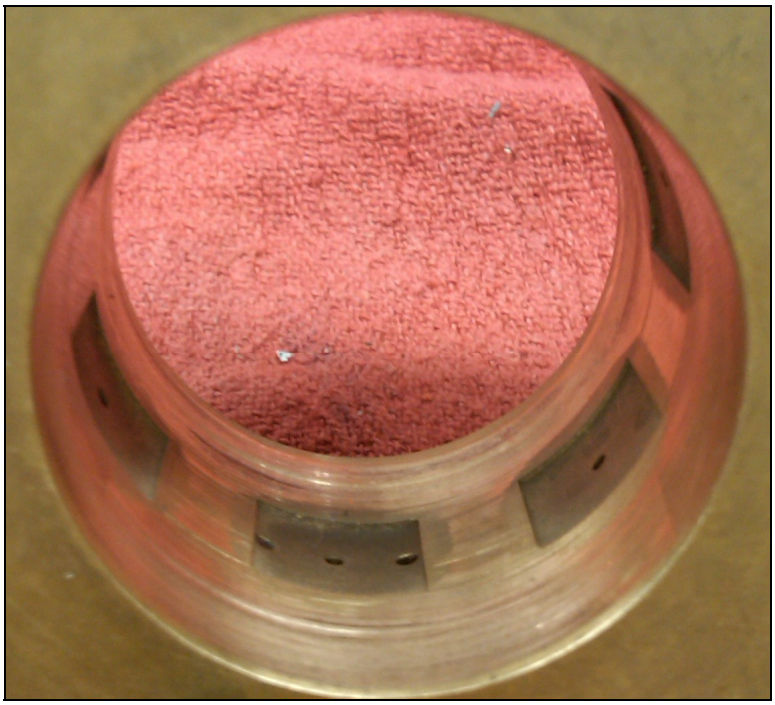

Fig. 38 Bearing before start-transient testing with applied unit LOR direction

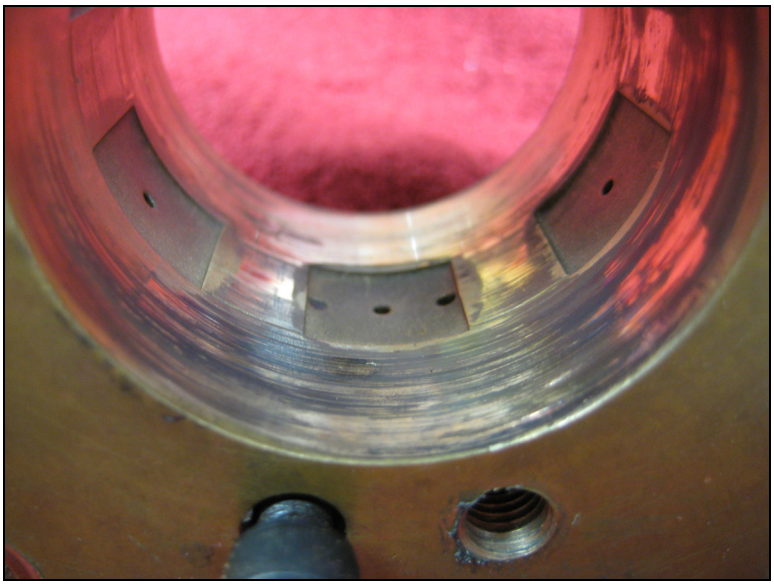

Fig. 39 Burnishing of the bearing with applied unit load LOR direction

Fig. 40 Bearing before start-transient testing with applied unit LOL direction

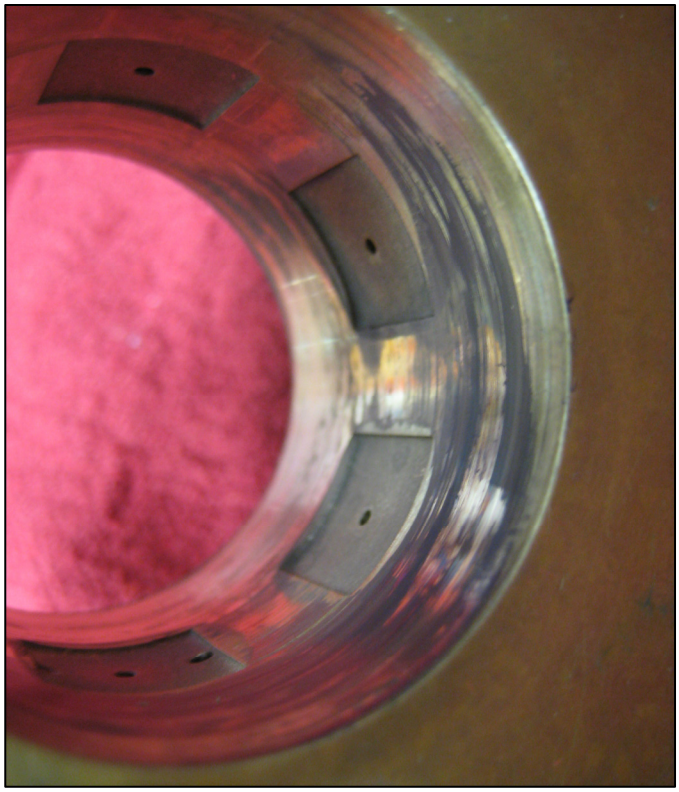

Fig. 41 Burnishing of the bearing with applied unit load LOL direction

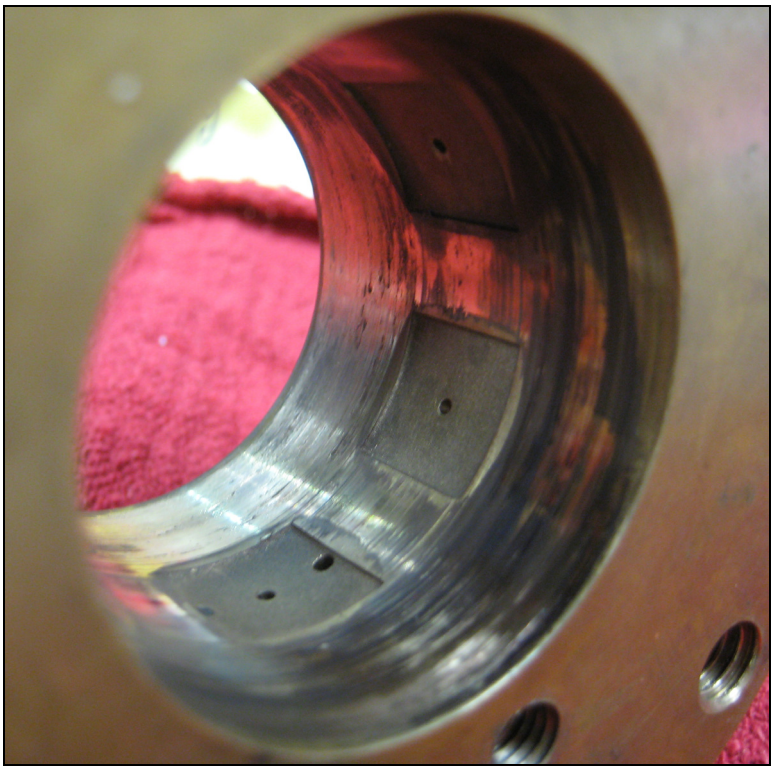

Fig. 42 Burnishing of the bearing in the direction of applied unit load after start-transient testing

CONCLUSIONS

Start-transient testing of a hybrid bearing with air was successfully completed, providing an indication of the performance of a hybrid bearing operating in a compressible fluid medium. Several parameters including the ramp rate, supply pressure at 15,000 *rpm*, magnitude of the load, and load orientation were varied. Data are stored in a .dat file for access by various computer programs for future evaluation of transient predictions. The current analysis investigates several topics including hydrodynamic and hydrostatic lift-off with comparisons to steady state predictions and previously acquired data from start-transient testing with water, rub due to passing through a lightly damped critical speed, and pneumatic hammer instability.

Hydrodynamic lift-off occurs due to the relative motion of the rotor to bearing surface in a wedge shape creating a hydrodynamic pressure effect. Hydrodynamic lift-off could not be confirmed from any of the three methods used to determine hydrostatic lift-off.

Hydrostatic lift-off occurs due to the increase in external supply pressure (speed dependent) and defined as the point of departure towards the center of the bearing while remaining 0.00254 *mm* (0.1 *mils*) above the bearing clearance as determined from the rotor centerline plots. Similar values of hydrostatic lift-off were also determined when differences in the amplitude of the 1X synchronous forward and backward whirl were observed as well as variations in the motor torque. Analysis of the rotor centerline plots are the most reliable way to determine hydrostatic lift-off. Even so, this method is limited by the inability to accurately measure an established bearing clearance. Hydrodynamic and hydrostatic lift-off are important quantities to reduce the damage caused by metal to metal contact between the rotor and bearing surface.

Evaluation of the hydrostatic lift-off supply pressure versus applied unit load support the following conclusions: (1) the required supply pressure for hydrostatic lift-off is approximately a linear function of the applied unit load (2) changing the ramp rate while keeping the supply pressure at 15,000 *rpm* constant has no significant impact (3) lowering the supply pressure at 15,000 *rpm* may reduce the required supply pressure for hydrostatic lift-off and (4) the LOR start-transient cases required a higher hydrostatic lift-

off speed and supply pressure than the corresponding LOL start-transient cases. The dependence of speed on hydrostatic lift-off is only because the supply pressure is proportional to the speed squared.

In cases 3-5 and cases 8-10 in Table 9, the start-transient test case passed through a critical speed, in some cases causing a rub in the start-transient tests that hydrostatically lifted-off before passing through the critical speed. Yu et al. [17] generated dry-friction whip caused by rubbing contact while transitioning through a critical speed. Wilkes et al. [15] produced dry-friction whip and whirl on the same test rig used in the start-transient testing by impulse excitation. However, during start-transient tests rubbing while accelerating the rotor through a critical speed produced a synchronous forwardly preccessing motion.

Steady state predictions for hydrostatic lift-off using XLHydroJet® did well for the LOL cases but was low for the LOR cases. The ramp rate can not be taken into account in a steady state prediction. Given these facts and a poor relationship between the start of rubbing and the critical speed prediction, transient predictions for a hybrid bearing in air should be completed.

Pneumatic-hammer instability is observed in the hybrid bearing with air as the fluid medium, and careful attention is required in adaptation to cryogenic applications such as liquid hydrogen due to it being highly compressible.

REFERENCES

[1] Childs, D., and Hale, K., 1994, "A Test Apparatus and Facility to Identify the Rotordynamic Coefficients of High-Speed Hydrostatic Bearings," ASME Journal of Tribology, **116**(2), pp. 337-344.

[2] Scharrer, J.K., Tellier, J. and Hibbs, R., 1991, "A Study of the Transient Performance of Hydrostatic Journal Bearings: Part I-Test Apparatus and Facility," STLE Paper 91-TC-3B-1.

[3] Scharrer, J.K., Tellier, J. and Hibbs, R., 1991, "A Study of the Transient Performance of Hydrostatic Journal Bearings: Part II-Experimental Results," STLE Paper 91-TC-3B-2.

[4] Sharrer, J., Tellier, J. and Hibbs, R., 1992, "Start Transient Testing of an Annular Hydrostatic Bearing in Liquid Oxygen," AIAA Paper 92-3404.

[5] Borchard, R.H., 2008, "Transient Testing Results for an Experimental Hybrid Bearing," Texas A&M University Master's Project Report, Department of Mechanical Engineering

[6] Pavelek, D., 2006, "Development of a Test Apparatus for Validating Predictions of (i) Dry-Friction Whirl/Whip and (ii) Transient Hybrid Bearing Performance," Texas A&M University Master's Project Report, Department of Mechanical Engineering.

[7] "XLHYDROJET: Computational Analyses of Hydrostatic/Hydrodynamic Bearings," Texas A&M University. http://phn.tamu.edu/TRIBGroup/Soft_hydrojet_1.htm. Access date: May 2009.

[8] Dyck, B.J., 2007, "Experimental Study of Dry-Friction Whirl and Whip for a Rotor Supported by an Aannular Rub Surface." Texas A&M University Master's Project Report, Department of Mechanical Engineering.

[9] Mosher, P., and Childs, D., 1998, "Theory Versus Experiment for the Effects of Pressure Ratio on the Performance of an Orifice-Compensated Hybrid Bearing," ASME Journal of Vibration and Acoustics, **120**(4), pp. 930-936.

[10] San Andrés, L., 1991, "Fluid Compressibility Effects on the Dynamic Response of Hydrostatic Journal Bearings," WEAR, **146**, pp.269-283.

[11] Borchard, H., 2007, "Draft: A Report on Pneumatic Hammer Tests," Texas A&M University Master's Project Report, Department of Mechanical Engineering.

[12] Childs, D., 2001 "Stability Insights from Hybrid-Bearing Research at the Texas A&M University Turbomachinery Laboratory." Proc. ISCORMA–1, August 22, Lake Tahoe, CA.

[13] "XLTRC^2: Rotordynamics Software Suite," The Turbomachinery Laboratory, Texas A&M University. http://turbolab.tamu.edu/research/trc/XLTRC%202002.pdf. Access date: May 2009.

[14] Childs, D., 1993, *Turbomachinery Rotordynamics: Phenomena, Modeling, and Analysis*, John Wiley and Sons, New York.

[15] Wilkes, J., Dyck, B.J., Childs, D., and Phillips, S., 2009, "Measurements Versus Predictions For Multi-Mode Dry-Friction Whip and Whirl," Proceedings of IGTI Turbo Expo, Paper # GT2009-59459, Orlando, FL June.

[16] San Andrés, L., 2008, MEEN 626 Course Notes: Introduction to Hydrodynamic Lubrication, http://phn.tamu.edu/me626/Notes_pdf/Introduction.pdf. Access date: May, 2009.

[17] Yu, J. J., Goldman, P., and Bently, D., 2000, "Rotor/Seal Experimental and Analytical Study of Full Annular Rub," Proc. of ASME IGTI Turboexpo 2000, ASME, New York, Vol. 2000-GT-389, pp. 1–9.

APPENDIX

Magnetic Bearing

SKF manufactures the magnetic bearing exciter that applies the static and dynamic load to the rotor through a laminated sleeve. To prevent damage to the magnetic bearing during a power loss, catcher bearings are installed. A controller converts a zero to five voltage signal to a current which is sent to two axis channels, V24 (horizontal plane) and W24 (vertical plane). The axes have two degrees of freedom 180 degrees apart (referred to as I_{top} and I_{bottom}). Eq. (9) is used to calculate the force that is applied by the magnetic bearing.

$$F = C\left[\left(\frac{I_{top}}{2(g-x)}\right)^2 - \left(\frac{I_{bottom}}{2(g-x)}\right)^2\right] - F_o \tag{9}$$

The calibrated magnetic bearing has a calibration factor and effective gap that are constant for both axes (C = 11.341 and g = 535.01). The rotor is centered during calibration so the offset (x) is assumed to be zero. The calibrated tare is F_o = 0.184 for the vertical axis while the tare is F_o = -0.06 for the horizontal axis.

Borchard [5] calculated the force required from the magnetic bearing to provide the correct unit load for each start-transient. Using Eq. (9) Borchard [5] calculated the correct amp required by the magnetic bearing to apply the correct force to the rotor. The same method is used for this testing including control of the magnetic bearing in LabVIEW.

The desired load was to increase by multiples of the rotor weight, 0.263 *bar* (3.81 *psi*). However, a reevaluation of the applied load through custom VIs in LabVIEW revealed an incorrect calculation of load supported by the bearing. The recalculated unit load is presented in Table 14, Table 15 and Table 19, although not exactly multiples of the rotor weight.

Start-Transient Test Cases

Figure 9 displays the speed, supply and recess pressures for the 50% torque-50% pressure case against the ROCETS data. The 100% torque-100% pressure, 50% torque-100% pressure, 25% torque-50% pressure, and 25% torque-25% pressure cases are compared to the equivalent ROCETS data in Figures 43-46, respectively.

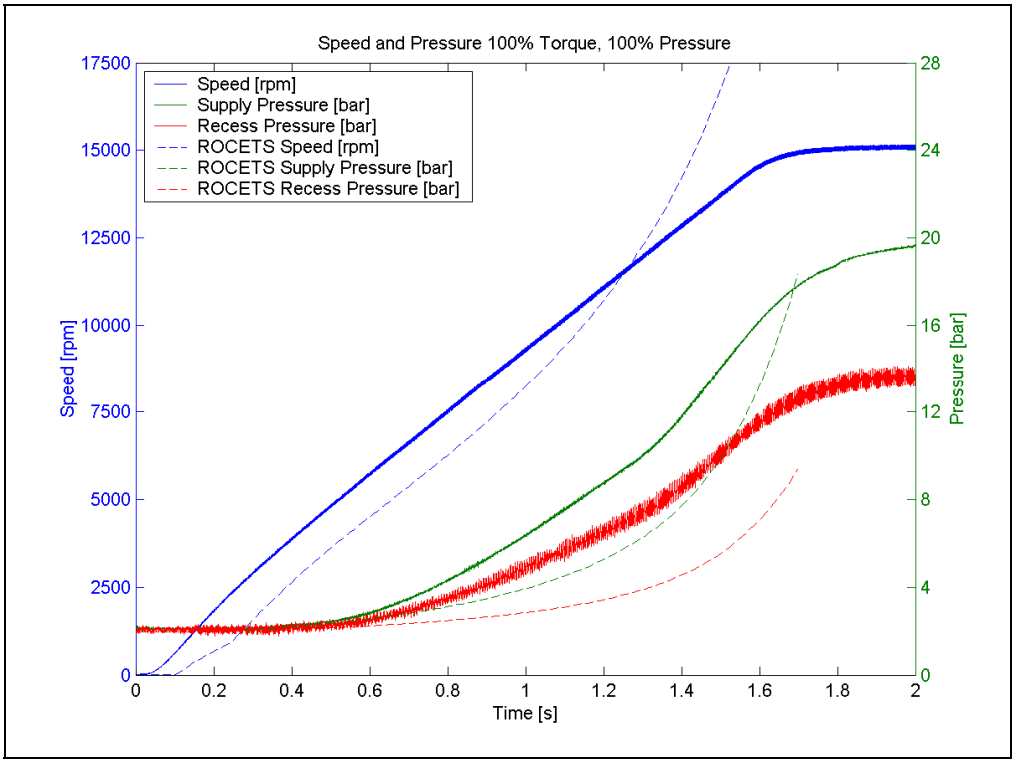

Fig. 43 Comparison between ROCETS data and start-transient test 100% torque-100% pressure

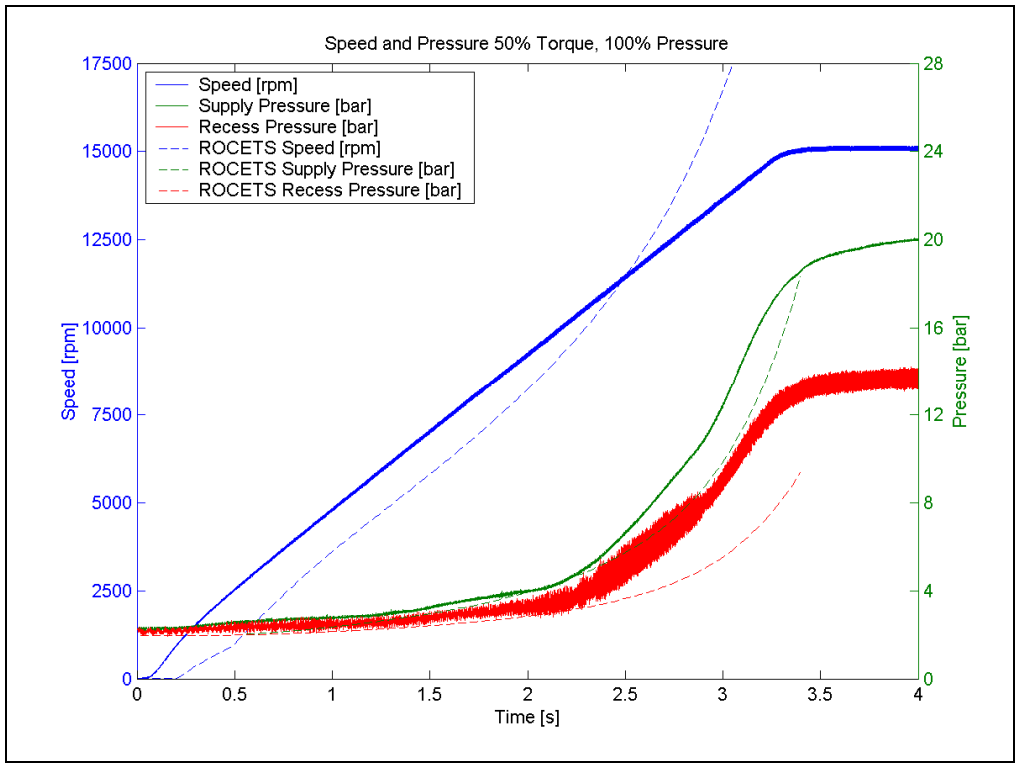

Fig. 44 Comparison between ROCETS data and start-transient test 50% torque-100% pressure

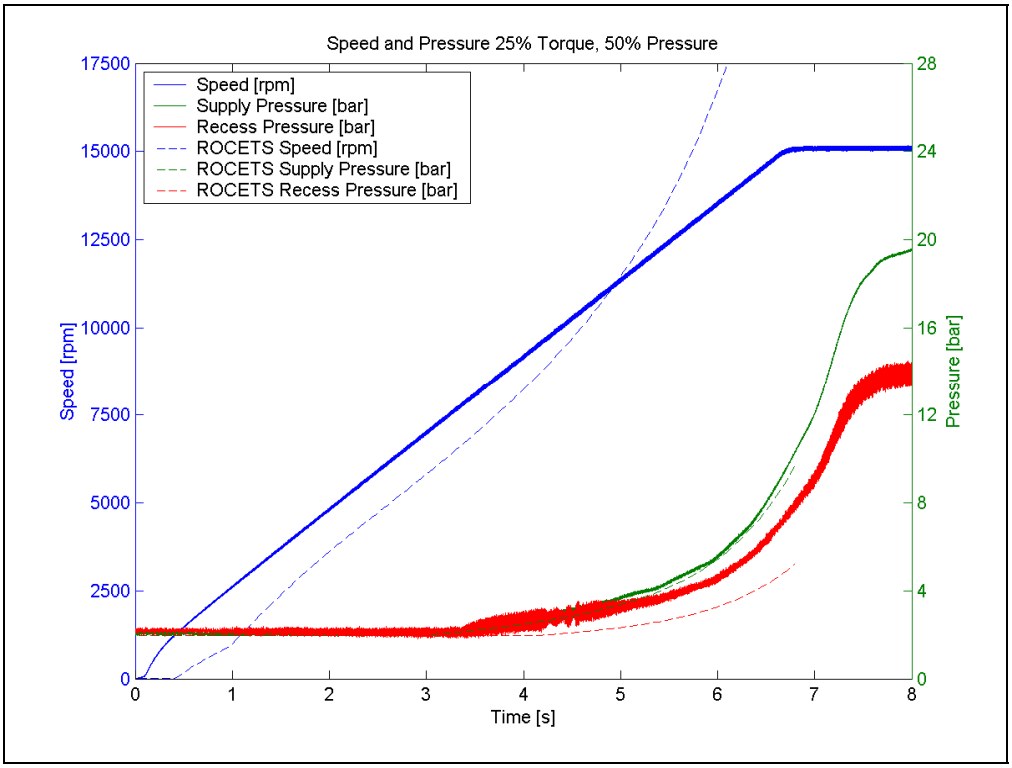

Fig. 45 Comparison between ROCETS data and start-transient test 25% torque-50% pressure

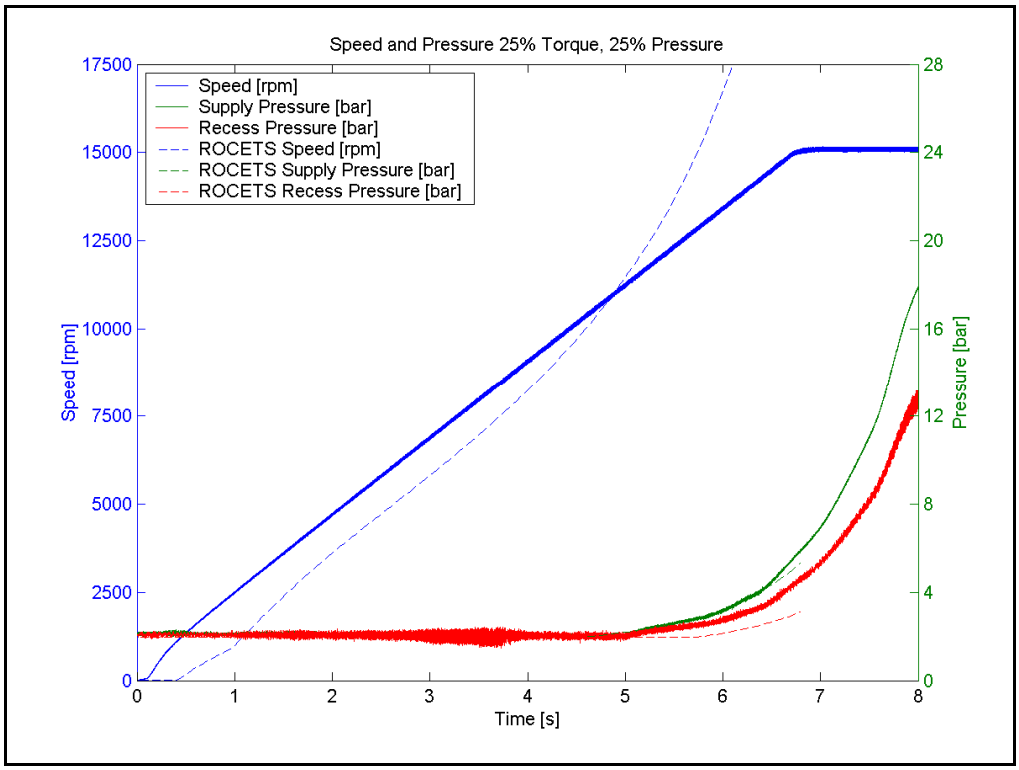

Fig. 46 Comparison between ROCETS data and start-transient test 25% torque-25% pressure

Instrumentation Specification

For start-transient testing of the hybrid bearing with air the data are recorded in a .dat file for later use. Table 18 details the instrumentation specifications for each sensor. For start-transient testing with air, some channels recorded in the .dat file are not utilized. The lift-off voltage recorded in channel seven is not used while channel eight is left blank. A new flow meter was installed in the modified fluid supply loop; therefore, the flow meter for water in channel fourteen is not needed. To limit the recess volume added to the bottom pocket due to the recess pressure-measurement ports, the dynamic pressure transducer in channel nineteen is removed and filled with wax. The exhaust air exits the bearing to the room; therefore the exhaust pressure and temperature in channels sixteen and twenty-one are measuring room temperature and pressure and not needed.

Table 18 Instrumentation specification for all sensors in .dat file

.dat file	Location	Manufacturer	Model	Sensitivity	Measurement Range	Fequency Range
	Speed					
1	Mounted Tachometer	NIDEC-SHIMPO	MCS-655	Once per Rev Pulse (Black/White)	N/A	N/A
	Proximity Probes					
2-3	Test Bearing Housing (Outboard)	Bently Nevada	3300 REBAM®	78.7 mV/mm (200 mV/mil)	0-0.2 mm (0-8 mil) (±6.4µm, ±0.25mil)	0-10,000 Hz +5%, -10%
	(2 probes mounted at 90 degrees)					
3-4	Test Bearing Housing (Inboard)	Bently Nevada	3300 REBAM®	78.7 mV/mm (200 mV/mil)	0-0.2 mm (0-8 mil) (±6.4µm, ±0.25mil)	0-10,000 Hz +5%, -10%
	(2 probes mounted at 90 degrees)					
5-6	Support Bearing Housing	Bently Nevada	3300 REBAM®	78.7 mV/mm (200 mV/mil)	0-0.2 mm (0-8 mil) (±6.4µm, ±0.25mil)	0-10,000 Hz +5%, -10%
	(2 probes mounted at 90 degrees)					
7	Lift-off Voltage	N/A	N/A	N/A	N/A	N/A
8	Blank2	N/A	N/A	N/A	N/A	N/A
	Accelerometers					
9-10	Support Bearing Housing	PCB Piezotronics	352C34	10 mV/g (±10%)	±50 g pk	0.5-10,000 Hz (±5%)
	(2 probes mounted at 90 degrees)					0.3-15,000 Hz (±10%)
11-12	Test Bearing Housing	PCB Piezotronics	352C34	10 mV/g (±10%)	±50 g pk	0.5-10,000 Hz (±5%)
	(2 probes mounted at 90 degrees)					0.3-15,000 Hz (±10%)
13	Drive Motor Casing	PCB Piezotronics	393A03	1000 mV/g (±5%)	±5 g pk	0.5-2,000 Hz (±5%)
	(1 probe mounted by support bearing)					0.3-4,000 Hz (±10%)
	Flow Meter (Water)					
14	Flow Meter	Flow Technology	FT-08AEXW-LEG-5	N/A	0.066-2.64 Liters/min (0.25-10 gpm)	N/A
	(Mounted before test bearing)					
	Speed					
15	Encoder Speed	N/A	N/A	N/A	N/A	N/A
	(Via motor controller software)					
	Pressure Transducers					
16	Exhaust Pressure	PCB Piezotronics	1501B01FB - 1000 psig/20	72.5 mV/bar (5 mV/psi) (± 2%)	0-68.9 bar (0-1000 psig) (±0.25%)	5-2,000 Hz
	(Mounted after test bearing)					
17	Supply Pressure	PCB Piezotronics	1501B01FB - 1000 psig/20	72.5 mV/bar (5 mV/psi) (± 2%)	0-68.9 bar (0-1000 psig) (±0.25%)	5-2,000 Hz
	(Mounted before test bearing)					
18	Recess Pressure	Kulite Semiconductor	XCQ-093-250A	0.406 mV/psia	0-17.2 bar (0-250 psia) (±5%)	N/A
	(Mounted in recess of test bearing)					
19	Dynamic Pressure	PCB Piezotronics	105C12	72.5 mV/bar (5 mV/psi) (±15%)	0-68.9 bar (0-1000 psig)	0.5-250,000 Hz
	(Mounted in recess of test bearing)					

Table 18. Continued

.dat file	Location	Manufacturer	Model	Sensitivity	Measurement Range	Fequency Range
	Temperature Sensors					
20	Supply Temperature	Omega	RTD-NPT-360-E	0.00385 Ω/Ω/°C	(0-230°C) 0-450°F	N/A
	(Mounted before test bearing)					
21	Exhaust Temperature	Omega	RTD-NPT-360-E	0.00385 Ω/Ω/°C	(0-230°C) 0-450°F	N/A
	(Mounted after test bearing)					
	Speed					
22	Scaled Tachometer	N/A	N/A	N/A	N/A	N/A
	(Via motor controller software)					
	Torque					
23	Load	N/A	N/A	N/A	N/A	N/A
	(Via motor controller software)					
24	Force Voltage	N/A	N/A	N/A	N/A	N/A
	(W 24 vertical displacement)					
	Temperature Sensors					
25	Flow Meter Temperature (Inlet)	Omega	RTD-NPT-72-E-DUAL-1/4-MPT	0.00385 Ω/Ω/°C	(0-230°C) 0-450°F	N/A
	(Mounted before flow meter)					
26	Flow Meter Temperature (Outlet)	Omega	RTD-NPT-72-E-DUAL-1/4-MPT	0.00385 Ω/Ω/°C	(0-230°C) 0-450°F	N/A
	(Mounted after flow meter)					
	Pressure Transducers					
27	Flow Meter Pressure (Inlet)	Omega	PX209-300G10V	483.6 mV/bar (33.3 mV/psig) (1.5%)	0-10.7 bar (0-300 psig) (0.25%)	N/A
	(Mounted before flow meter)					
28	Flow Meter Pressure (Outlet)	Omega	PX209-300G10V	483.6 mV/bar (33.3 mV/psig) (1.5%)	0-10.7 bar (0-300 psig) (0.25%)	N/A
	(Mounted after flow meter)					
29	Force Voltage	N/A	N/A	N/A	N/A	N/A
	(V 24 horizontal displacement)					
	Flow Meter (Air)					
30	Flow Meter	Flow Technology	FT8-8NEE1-GEAH4	N/A	0.40 - 8.0 ACFM	N/A
	(Mounted before test bearing)					
31	Valve Voltage	N/A	N/A	N/A	N/A	N/A

Start-Transient Predictions

A linear, steady-state rotordynamic analysis was completed by Pavelek [6] for the rotor bearing system, including added inertia from the tapered sleeve/laminate material and coupling, in XLTRC^2. Figure 47 shows the same rotordynamic model used by Pavelek [6] but for this analysis the linear stiffness, damping, and mass coefficients for the hybrid bearing with air are updated.

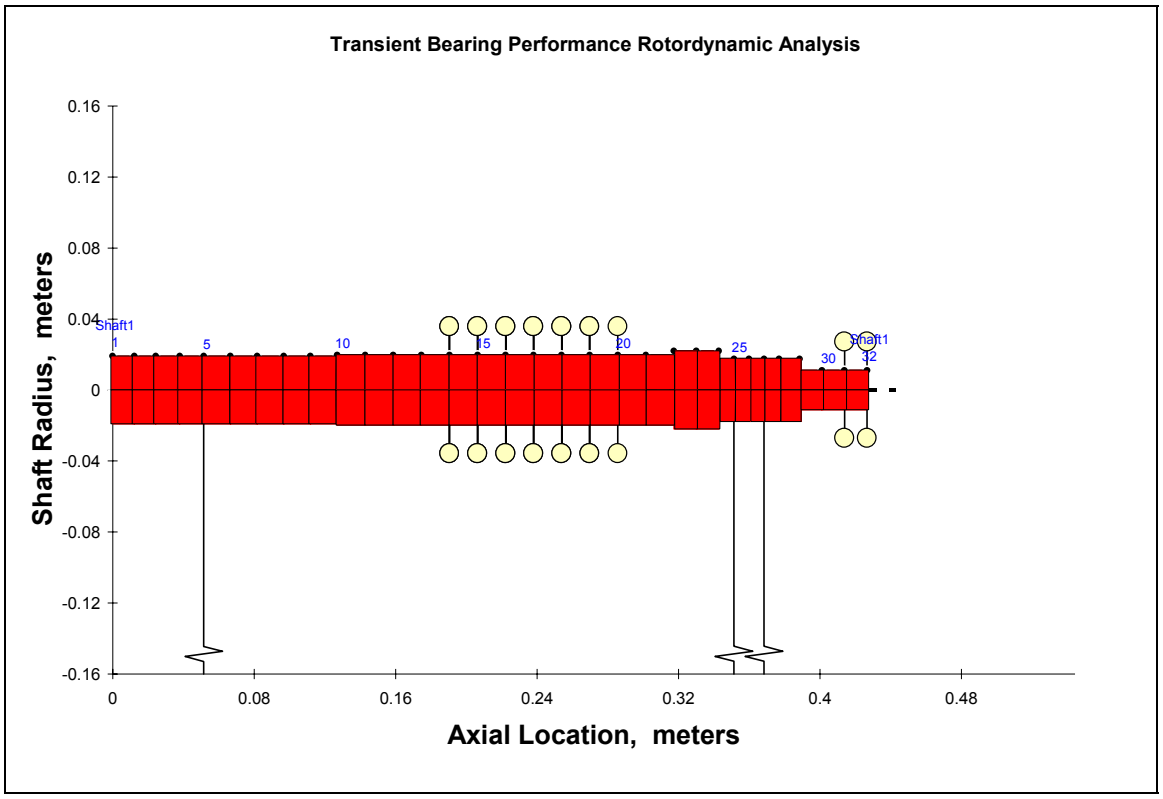

Fig. 47 Plot of model used in rotordynamic analysis

For each of the five start-transient test cases, a steady-state rotordynamic analysis using XLTRC^2 is performed. The following is the steady-state rotordynamic analysis results were not included in the report for brevity.

Figure 48 shows the rotordynamic damped natural frequency map for the 100% torque-100% pressure case. The first and second natural frequencies remain above the synchronous line, therefore, in the range below 15,000 *rpm* there is no predicted critical

speed. Figure 49 shows the mode shape for the first two natural frequencies at 15,000 *rpm* while Figure 50 shows the response at the hybrid bearing.

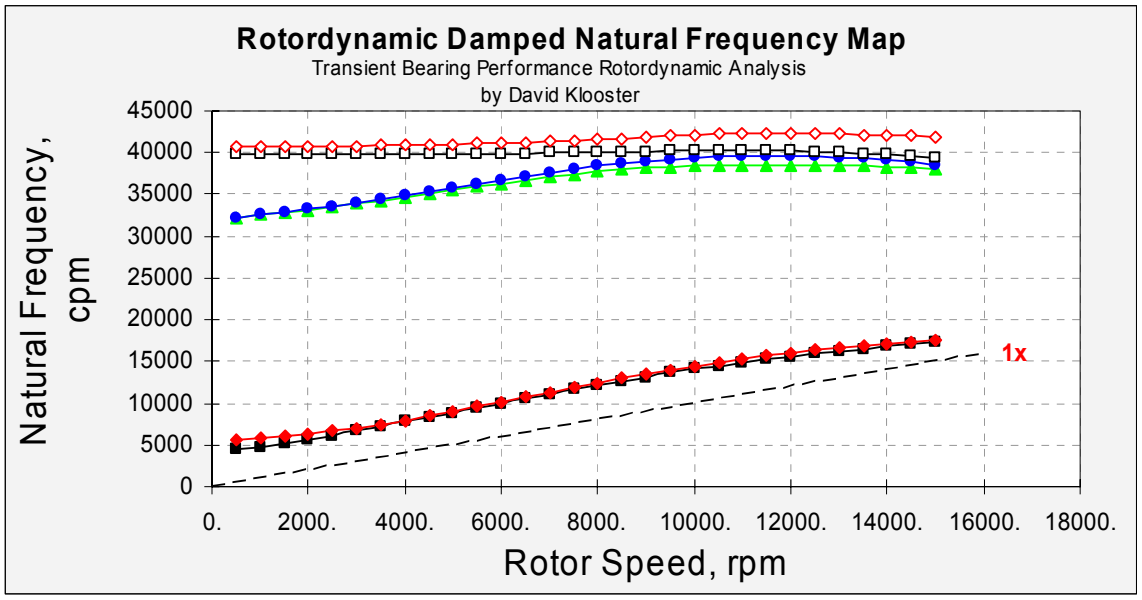

Fig. 48 Rotordynamic damped natural frequency map 100% torque-100% pressure

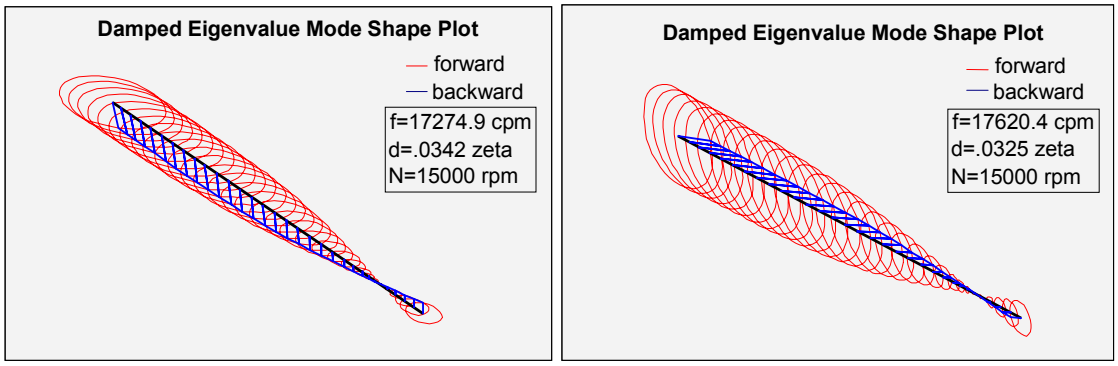

Fig. 49 Damped eigenvalue mode shape for first two modes 100% torque-100% pressure

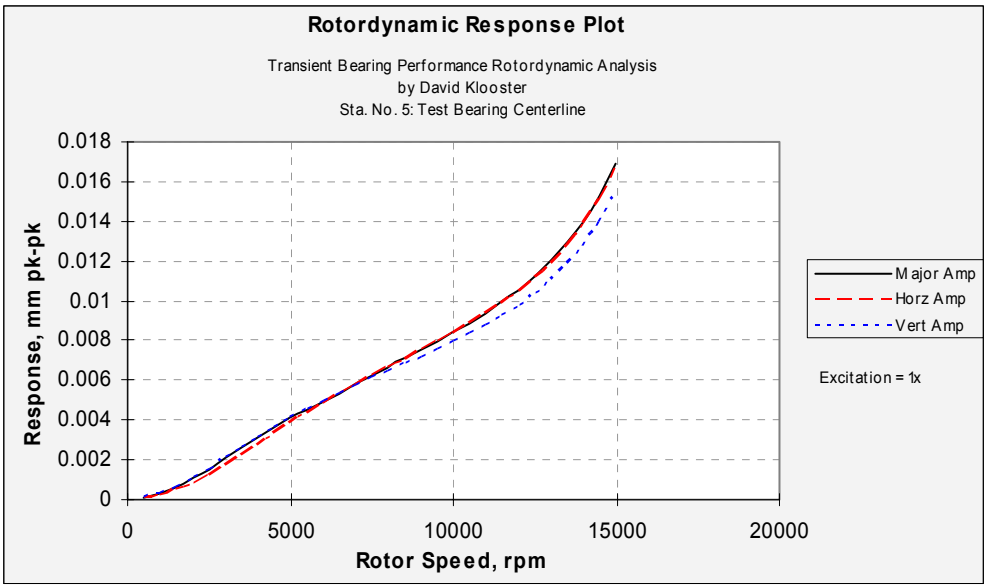

Fig. 50 Steady state rotordynamic response plot at test bearing 100% torque-100% pressure

Similar to the 100% torque-100% pressure case the 50% torque-100% pressure rotordynamic analysis is presented in Figures 51-53.

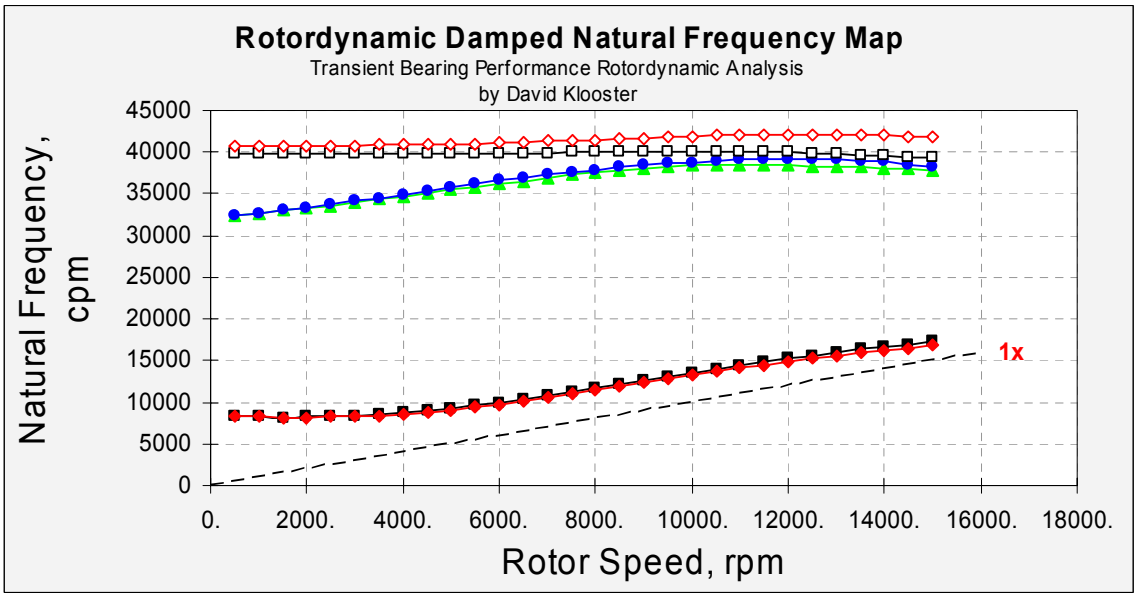

Fig. 51 Rotordynamic damped natural frequency map 50% torque-100% pressure

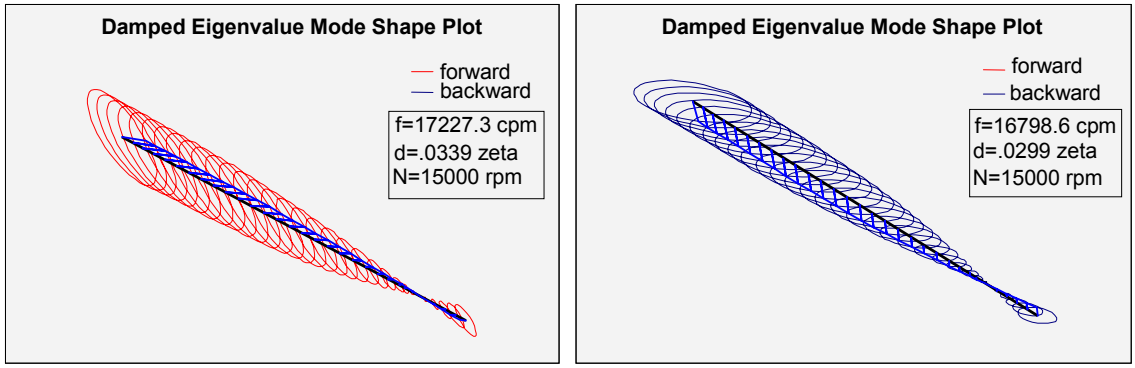

Fig. 52 Damped eigenvalue mode shape for first two modes 50% torque-100% pressure

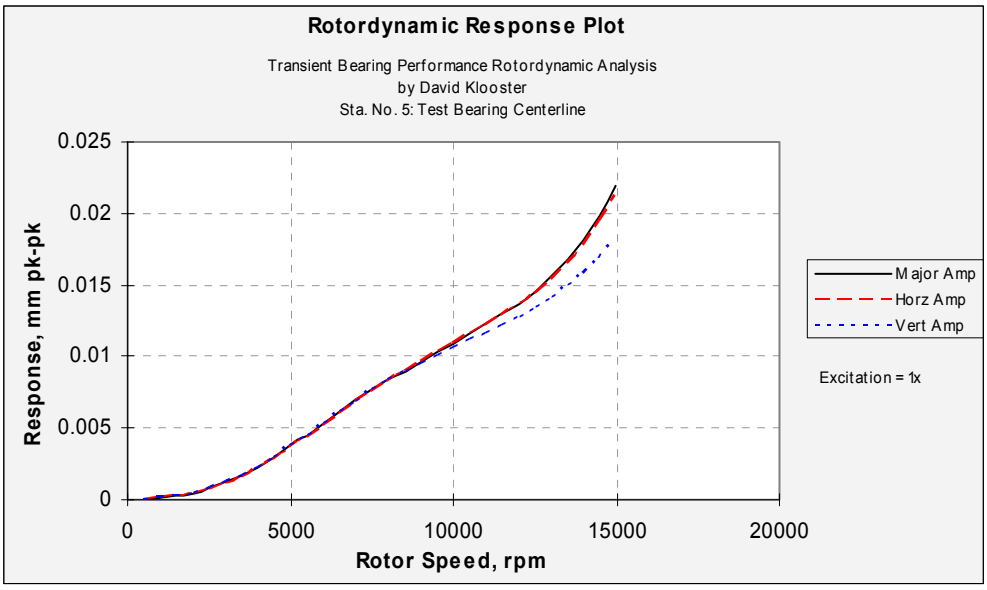

Fig. 53 Steady state rotordynamic response plot at test bearing 50% torque-100% pressure

The 50% torque-50% pressure case was detailed in the report, while the 25% torque-50% pressure case is detailed in Figures 54-56. Figure 57 shows the mode shapes for the two critical speeds in the 25% torque-25% pressure case that are detailed in the report.

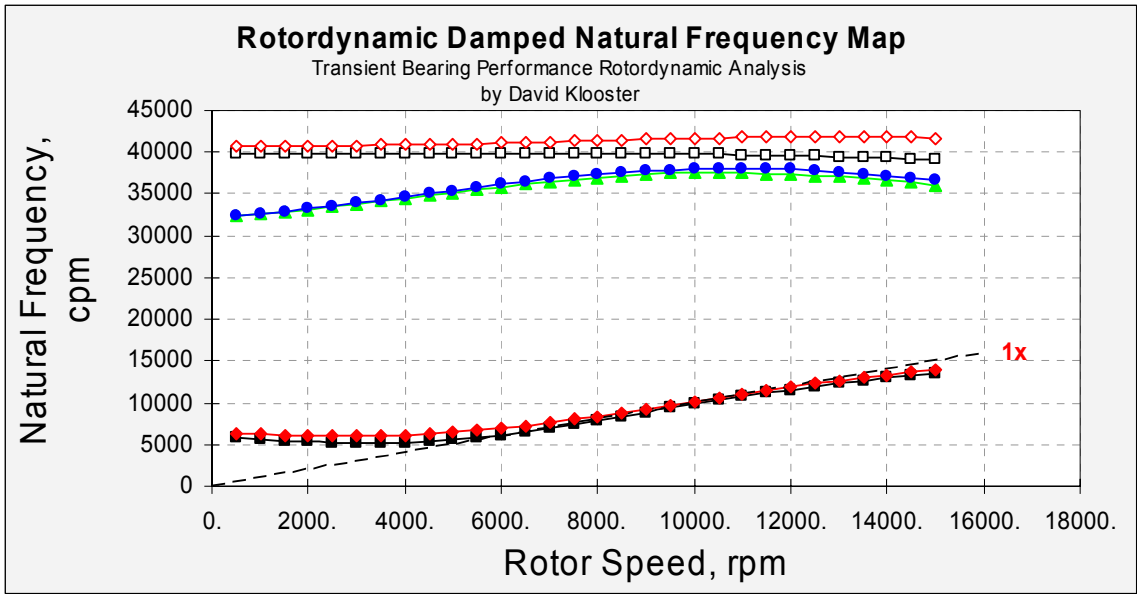

Fig. 54 Rotordynamic damped natural frequency map 25% torque-50% pressure

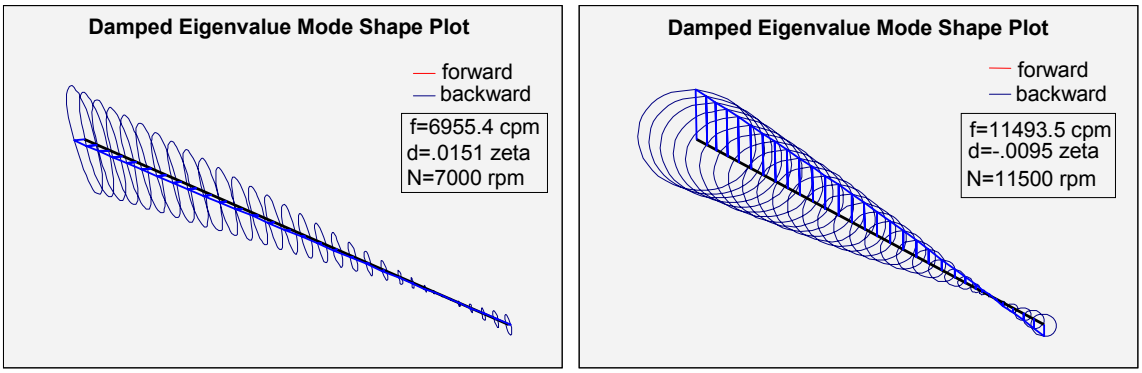

Fig. 55 Damped eigenvalue mode shape for first two modes 25% torque-50% pressure

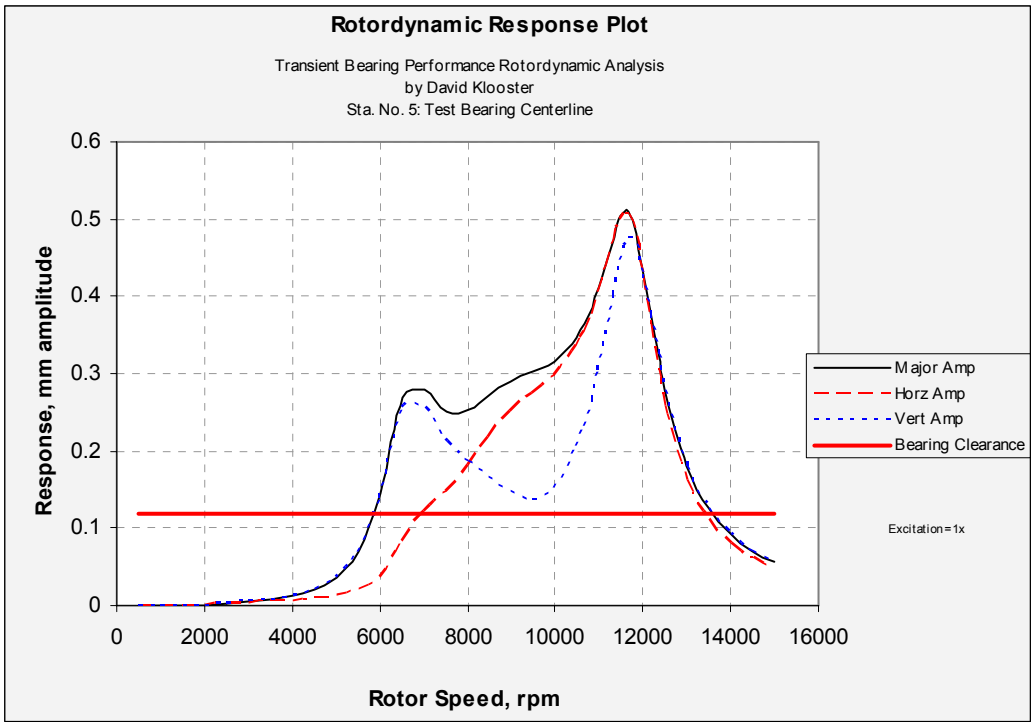

Fig. 56 Steady state rotordynamic response plot at test bearing 25% torque-50% pressure

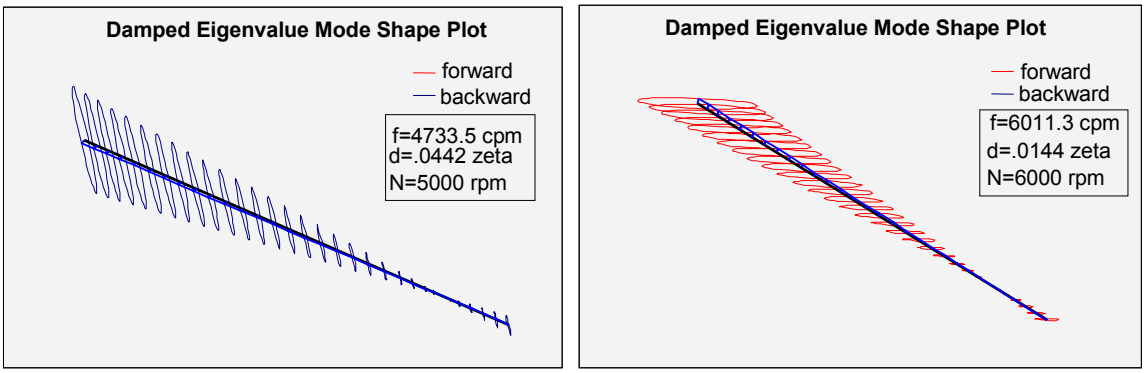

Fig. 57 Damped eigenvalue mode shape for first two modes 25% torque-25% pressure

Rub

Rub was determined from the rotor centerline plots when the rotor equaled or exceeded the established bearing clearance. Table 19 presents the start and stopping point of rub for each start-transient in which a rubbing occurred.

Table 19 Start and stop points for rub

Ramp Rate [rpm/s]	Supply Pressure at 15,000 rpm [bar (psia)]	Start/Stop of intermittent rub	Speed [rpm]	Supply Pressure [bar (psia)]	Recess Pressure [bar (psia)]	Pressure Ratio	Temperature [°C (°F)]	Rate [kg/s]	Unit Load [bar (psi)]	load [rad (deg)]
4412	9.63 bar (139.7 psia)	Start	8916	2.87 (41.6)	1.79 (26.0)	0.62	20.8 (69.4)	0.0037	0.263 (3.81)	0 (0)
4412	9.63 bar (139.7 psia)	Stop	10358	3.11 (45.1)	2.40 (34.8)	0.77	20.7 (69.3)	0.0039	0.263 (3.81)	0 (0)
4412	9.63 bar (139.7 psia)	Start	2059	1.98 (28.7)	2.14 (31.0)	1.08	20.3 (68.6)	0.0018	0.311 (4.51)	0 (0)
4412	9.63 bar (139.7 psia)	Stop	8937	2.54 (36.8)	2.74 (39.7)	1.08	20.3 (68.6)	0.0033	0.311 (4.51)	0 (0)
2206	9.63 bar (139.7 psia)	Start	5454	1.77 (25.7)	1.90 (27.5)	1.07	18.6 (65.4)	0.0018	0.263 (3.81)	0 (0)
2206	9.63 bar (139.7 psia)	Stop	10591	3.46 (50.2)	3.02 (43.8)	0.87	18.6 (65.4)	0.0044	0.263 (3.81)	0 (0)
2206	9.63 bar (139.7 psia)	Start	4557	2.05 (29.8)	2.12 (30.7)	1.03	20.8 (69.4)	0.0021	0.311 (4.51)	0 (0)
2206	9.63 bar (139.7 psia)	Stop	10446	3.20 (46.4)	3.37 (48.8)	1.05	20.8 (69.4)	0.0042	0.311 (4.51)	0 (0)
2206	5.32 bar (77.2 psia)	Start	7023	2.11 (30.7)	2.03 (29.4)	0.96	20.9 (69.7)	0.0023	0.263 (3.81)	0 (0)
2206	5.32 bar (77.2 psia)	Stop	8508	2.10 (30.5)	2.25 (32.7)	1.07	20.9 (69.6)	0.0021	0.263 (3.81)	0 (0)
2206	5.32 bar (77.2 psia)	Start	5897	2.11 (30.6)	2.19 (31.8)	1.04	19.7 (67.5)	0.0023	0.311 (4.51)	0 (0)
2206	5.32 bar (77.2 psia)	Stop	8414	1.96 (28.5)	2.12 (30.7)	1.08	19.7 (67.5)	0.0020	0.311 (4.51)	0 (0)
4412	9.63 bar (139.7 psia)	Start	7555	2.27 (32.9)	1.99 (28.9)	0.88	20.7 (69.3	0.0026	0.282 (4.09)	0.705 (40.4)
4412	9.63 bar (139.7 psia)	Stop	9294	2.73 (39.6)	2.83 (41.1)	1.04	20.7 (69.2)	0.0035	0.282 (4.09)	0.705 (40.4)
4412	9.63 bar (139.7 psia)	Start	26	2.10 (30.5)	1.91 (27.6)	0.91	18.2 (64.7)	0.0021	0.443 (6.42)	1.07 (61.0)
4412	9.63 bar (139.7 psia)	Stop	9009	2.73 (39.6)	2.86 (41.5)	1.05	18.2 (64.8)	0.0037	0.443 (6.42)	1.07 (61.0)
2206	9.63 bar (139.7 psia)	Start	1172	1.54 (22.3)	1.63 (23.6)	1.06	19.2 (66.5)	0.0012	0.282 (4.09)	0.705 (40.4)
2206	9.63 bar (139.7 psia)	Stop	9752	3.01 (43.6)	2.84 (41.2)	0.94	19.2 (66.6)	0.0038	0.282 (4.09)	0.705 (40.4)
2206	9.63 bar (139.7 psia)	Start	3079	2.06 (29.8)	1.97 (28.6)	0.96	19.6 (67.2)	0.0024	0.443 (6.42)	1.07 (61.0)
2206	9.63 bar (139.7 psia)	Stop	9729	3.13 (45.4)	3.13 (45.5)	1.00	19.6 (67.2)	0.0040	0.443 (6.42)	1.07 (61.0)
2206	5.32 bar (77.2 psia)	Start	6491	1.91 (27.7)	1.98 (28.7)	1.04	19.5 (67.1)	0.0019	0.282 (4.09)	0.705 (40.4)
2206	5.32 bar (77.2 psia)	Stop	8023	1.98 (28.7)	2.09 (30.4)	1.06	19.5 (67.2)	0.0021	0.282 (4.09)	0.705 (40.4)
2206	5.32 bar (77.2 psia)	Start	1699	2.11 (30.6)	2.12 (30.8)	1.00	21.0 (69.8)	0.0024	0.443 (6.42)	1.07 (61.0)
2206	5.32 bar (77.2 psia)	Stop	8659	2.31 (33.5)	1.55 (22.4)	0.67	21.0 (69.8)	0.0029	0.443 (6.42)	1.07 (61.0)

Another method for determining what speeds rubbing occurs is to look for super synchronous vibration in a double sided waterfall plot. A particular area of interest is near 615 *Hz* which is the natural frequency of the test bearing housing in the *x* direction. Figure 58 shows a super synchronous vibration at about 680 *Hz* from 4,212 *rpm* to 10,460 *rpm*. The range using the rotor centerline plot for this case is 5,454 *rpm* to 10,591 *rpm*. Table 20 details the start and stop points of rub from super synchronous vibration observation.

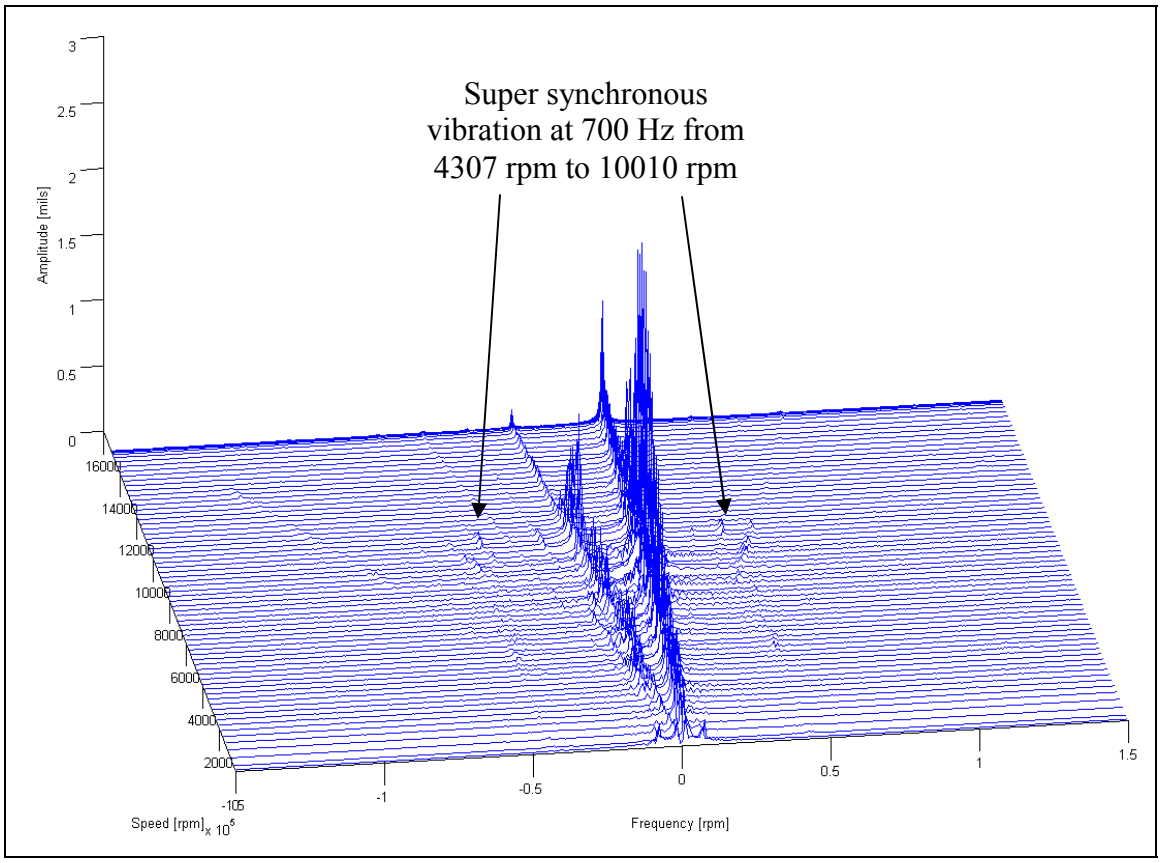

Fig. 58 Double sided waterfall plot for outboard proximity probes for 50% torque-50% pressure 4X applied unit load

Table 20 Start and stop points of rub from super synchronous vibration observation

	Ramp Rate [rpm/s]	Supply Pressure at 15,000 rpm [bar (psia)]	Speed [rpm]	
			Start Rub	Stop Rub
Case 3	4412	9.63 bar (139.7 psia)	7243	9278
Case 3	4412	9.63 bar (139.7 psia)	7802	10510
Case 4	2206	9.63 bar (139.7 psia)	4418	10540
Case 4	2206	9.63 bar (139.7 psia)	4291	10190
Case 5	2206	5.32 bar (77.2 psia)	8400	10070
Case 5	2206	5.32 bar (77.2 psia)	8459	10460
Case 8	4412	9.63 bar (139.7 psia)	6263	10500
Case 8	4412	9.63 bar (139.7 psia)	4698	10280
Case 9	2206	9.63 bar (139.7 psia)	6865	7981
Case 9	2206	9.63 bar (139.7 psia)	7716	8607
Case 10	2206	5.32 bar (77.2 psia)	4562	9027
Case 10	2206	5.32 bar (77.2 psia)	4698	8495

VITA

Name:	David Gregg Klooster
Address:	DRS Technologies 13544 North Central Expressway Dallas, TX 75243
Email Address:	klooster54@hotmail.com
Education:	B.S., Mechanical Engineering, Kettering University, 2007 M.S., Mechanical Engineering, Texas A&M University, 2009